Magnetic-force microscopy and micromagnetic simulations on domains of structured ferromagnets

Dissertation
zur Erlangung des Doktorgrades
des Fachbereichs Physik
der Universität Hamburg

vorgelegt von
Miriam Barthelmeß
geb. Halverscheid
aus Bochum

Hamburg
2003

Gutachter der Dissertation:	Prof. Dr. U. Merkt Prof. Dr. W. Hansen
Gutachter der Disputation:	Prof. Dr. U. Merkt Prof. Dr. D. Heitmann
Datum der Disputation:	13. Mai 2004
Vorsitzender des Prüfungsausschusses:	Dr. S. Kettemann
Vorsitzender des Promotionsausschusses:	Prof. Dr. R. Wiesendanger
Dekan des Fachbereichs Physik :	Prof. Dr. G. Huber

Abstract

In this thesis, the magnetization of microstructured ferromagnets is studied with help of computer simulations in comparison to experiments. As experimental techniques magnetic-force microscopy and Hall μ-magnetometry are used. The latter measures the stray field generated by ferromagnetic elements in external magnetic fields. Comparison to simulated hysteresis curves of the magnetization gives the possibility to analyze the coercive and saturating fields of the particles. However, no statements can be made about the signal strength. For this reason, a computer code has been developed, which uses the output data of the micromagnetic simulations to calculate the stray field in arbitrary distances above the sample. The magnetization data is therefore interpreted as magnetic dipoles in the lattice cells, which have been defined for the simulation. The stray fields of the single dipoles are superimposed and can be visualized pointwise or utilized for further calculations. The measurement signal of Hall μ-magnetometry in the ballistic regime is simulated by averaging across the sensitive area above the Hall cross. The comparison between measurement and simulation yields good agreement.

As a second experimental method, magnetic-force microscopy is used. The resulting domain patterns are at first compared to simulated magnetization configurations. Since the measurement signal consists of contributions of all depths, it is rather complicated to interpret it in terms of magnetization. Again, the calculation of the corresponding signal from magnetization data serves for a direct comparison. The measurement signal corresponds to the second derivative of the stray field in out-of-plane direction, so that it can be calculated in connection to the stray field.

These calculations are performed on permalloy elements of various geometries. For comparison, a permalloy sample with distinct geometries and different film thicknesses in immediate neighborhood is prepared and measured by magnetic-force microscopy in the as-prepared state as well as in external magnetic fields. The investigation of domain walls in the structured material yields a transition between cross-tie and Bloch walls between 70 and 100 nm film thickness.

Inhaltsangabe

In dieser Arbeit werden mikrostrukturierte Ferromagnete mit Hilfe von Simulationsrechnungen untersucht und die Ergebnisse mit Experimenten verglichen. Als experimentelle Methoden werden die Magnetkraftmikroskopie und die Hall μ-Magnetometrie angewendet. Mit letzterer kann das Streufeld von ferromagnetischen Elementen in Abhängigkeit des äußeren Magnetfeldes gemessen werden. Der Vergleich mit simulierten Hysteresekurven der Magnetisierung liefert ausschließlich die Möglichkeit, die Koerzitiv- und Sättigungsfelder zu analysieren, nicht aber, Aussagen über die Signalstärken zu treffen. Aus diesem Grunde wird das Simulationsprogramm durch ein Zusatzprogramm erweitert, das die Berechnung des Streufelds in beliebiger Höhe über dem Objekt ermöglicht. Hierfür wird die Ausgabe des Simulationsprogrammes genutzt. Diese besteht aus einer Anordnung von magnetischen Dipolen im für die Simulation definierten Gitter. Die Summe der Streufelder der einzelnen Dipole wird berechnet und kann anschliessend Punkt für Punkt dargestellt oder für weitere Berechnungen genutzt werden. Für die Simulation des Hall-Signals im ballistischen Bereich müssen die Streufeldwerte beispielsweise über den Bereich des Hall-Kreuzes gemittelt werden. Die Berechnung des Hall-Signals liefert eine gute Übereinstimmung mit dem Experiment.
Als zweite experimentelle Untersuchungsmethode wird das Magnetkraftmikroskop verwendet. Die resultierenden Abbildungen der magnetischen Domänen werden im ersten Schritt mit den Magnetisierungmustern aus der Simulation verglichen. Die Interpretation des Messsignals im Hinblick auf die detaillierte Magnetisierung ist jedoch kompliziert und nicht immer eindeutig, denn das Messsignal besteht aus einer Überlagerung der Signale aller Schichten. Eine direkte Vergleichsmöglichkeit liefert auch hier die Berechnung des Messsignals aus den Simulationsdaten. Das Messsignal ist proportional zur zweiten Ableitung des Streufelds senkrecht zur Probenebene. Diese Berechnungen werden an Permalloy Elementen verschiedener Geometrien ausgeführt. Zum Vergleich wird eine Probe hergestellt, auf der Geometrien verschiedener Dicke direkt nebeneinander liegen und mit dem Magnetkraftmikroskop gleichzeitig gemessen werden können. Die Untersuchung der Domänenwände ergibt einen Übergang zwischen Crosstie- und Bloch-Wänden in Filmdicken zwischen 70 und 100 nm.

Contents

Chapter 1

Introduction

The ferromagnetism of micro- and nanostructures is a very active field of basic research and provides a high potential for technological applications [1, 2]. On the one hand, the magnetization behavior itself is of great interest [3, 4], e.g., there is a present discussion about the internal structure of domain walls in thin films and laterally defined elements [5]. If electron transport comes into play, a detailed knowledge of the underlying magnetic structure is of crucial importance. In the nanometer range, one has to distinguish between the classical anisotropic magnetoresistance and the so called domain wall resistance. Furthermore, ferromagnetic materials build an important feature for the realization of future electronic devices, which also make use of the spin of the current carriers, so called spintronic devices [6, 7, 8]. As sources of spinpolarized electrons, 3d transition metals, Heusler alloys and ferromagnetic semiconductors are considered. For all materials, certain requirements concerning the magnetization of the micro- and nanostructured electrodes have to be fulfilled. For example, a high degree of spin polarization has to be combined with small stray fields, as it can be achieved by a tailored multidomain structure [9].

In this work, domains in ferromagnetic permalloy ($Ni_{80}Fe_{20}$) and iron structures are investigated by comparing simulated magnetization patterns to experimental results from Hall μ-magnetometry and magnetic-force microscopy. For this purpose, simulated signals corresponding to the signals of both experimental methods are computed from calculated magnetization data. Detailed investigations of the magnetization behavior in external magnetic fields and the domain wall structure are performed.

The thesis is organized as follows: In chapter 2, the theoretical background for ferromagnetic systems is introduced. Chapter 3 briefly describes the experimental methods, whereas in chapter 4 the computer code used for the simulation of magnetization patterns as well as calculations of the measured signals are presented. Most results of this thesis have already been published. Accordingly, chapter 5 mainly consists of the reprinted publications [P1], [P2], [P3], and [P4].

[P1] G. Meier, M. Halverscheid, T. Matsuyama, and U. Merkt, *Investigation of ferromagnetic microstructures as electrodes for spin-polarized transport experiments*, J. Appl. Phys. **89**, 7469 (2001).

[P2] G. Meier, R. Eiselt, and M. Halverscheid, *Hall micromagnetometry on iron electrodes suitable for spin-polarized transport*, J. Appl. Phys. **92**, 7296 (2002).

[P3] M. Barthelmess, A. Thieme, R. Eiselt, and G. Meier, *Stray fields of iron electrodes for spin-polarized transport*, J. Appl. Phys. **93**, 8400 (2003).

[P4] M. Barthelmess, C. Pels, A. Thieme, and G. Meier, *Stray fields of domains in permalloy microstructures - measurements and simulations*, J. Appl. Phys. **94**, 5641 (2004).

[P5] C. Pels, M. Barthelmess, A. Thieme, and G. Meier, *Thickness and magnetic-field dependence of domain switching in isolated and interacting permalloy contacts*, submitted to J. Magn. Magn. Mat.

[P6] G. Meier, R. Eiselt, M. Barthelmess, M. Bolte, T. Eimüller, and P. Fischer, *Comparative study of magnetization reversal in isolated and stray-field coupled microcontacts*, Appl. Phys. Lett. **85**, 1193 (2004).

Chapter 2

Theoretical background

2.1 Ferromagnetism

The magnetic moment of free electrons has three principal sources: The spin of the electrons, the orbital angular momentum of the electrons moving around the nucleus, and the change in the orbital momentum induced by an applied magnetic field. The first two sources yield paramagnetic and the third diamagnetic contributions to the magnetization. In principal, these contributions can also be found in the solid state. In an external magnetic field, a magnetic moment opposing the external field is induced in a solid as a result of Lenz' law. This diamagnetic effect is often superimposed by paramagnetism, which results from unfilled electron orbitals. The induced magnetization $\vec{M}$, defined as the dipole moment per unit volume, is proportional to the external magnetic field $\vec{H}$:

$$\vec{M} = \chi \vec{H} \tag{2.1}$$

with χ being the magnetic susceptibility of the material. The relation between the magnetic inductance $\vec{B}$ and the magnetization (in SI units used throughout this thesis) then is:

$$\vec{B} = \mu_0(\vec{H} + \vec{M}) = \mu_0(\vec{H} + \chi\vec{H}) = \mu_0(1+\chi)\vec{H} = \mu_0\mu_r\vec{H}\,. \tag{2.2}$$

Here, μ_0 is the vacuum permeability and $\mu_r = 1 + \chi$ the magnetic permeability, which is a material parameter. Depending on the sign and magnitude of χ, the different types of magnetism are distinguished [10]. In the case of $\chi < 0$ and $|\chi| << 1$, the material is diamagnetic, whereas for $\chi > 0$ and typically $10^{-6} < \chi < 10^{-4}$ we speak of paramagnetism. A third type of magnetism is ferromagnetism with $10^2 < \chi < 10^5$. Ferromagnetic materials have a spontaneous magnetization at zero external magnetic field. In some magnetically ordered materials, the magnetic moments couple in an antiparallel configuration. They are called antiferromagnets and have no net magnetic moment. If a material consists

of two antiferromagnetically coupled sublattices having unequal moments, the net moment is not zero. Those materials are called ferrimagnetic.
In this work, ferromagnetic samples, namely iron and permalloy, are investigated. Like paramagnetism, ferromagnetism depends on temperature. Above the so called Curie temperature the material becomes paramagnetic. In ferromagnets, $\vec{M}$ is not proportional to $\vec{H}$, but depends on the history of the magnetization. The relation between the magnetization along the direction of the external field $\vec{M}_H$ and $\vec{H}$ is hysteretic as shown in Fig. 2.1.

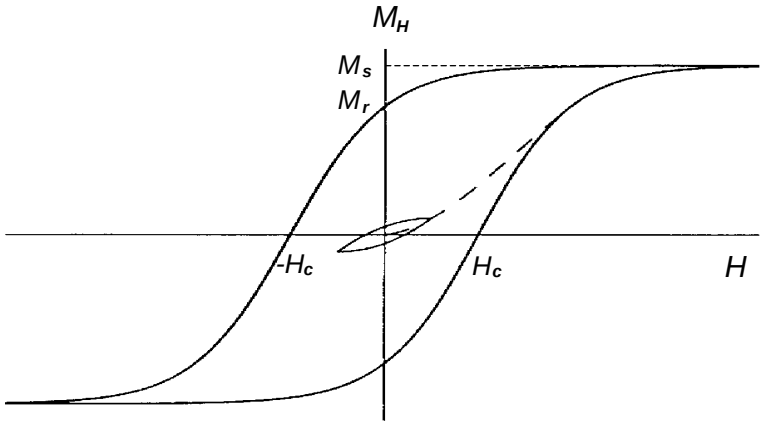

Figure 2.1: Hysteresis curve for ferromagnetic materials, showing the magnetization $\vec{M}$ in the direction of the external field as a function of the external field $\vec{H}$.

Starting with the initial magnetization curve at an unmagnetized state, at a certain external field $\vec{H}$, the ferromagnet is saturated with the saturation magnetization M_s. Now all magnetic moments are oriented in the direction of the external magnetic field, so that the saturation magnetization is the largest magnetization, which can be achieved in the material. If the external field is reduced to zero, a net magnetization will remain in the ferromagnet, called remanence M_r. To decrease the magnetization, a negative external field opposing the orientation of the magnetic moments needs to be applied. The external field, at which the magnetization is reduced to zero, is called coercive field $\vec{H}_c$. Depending on the magnitude of $\vec{H}_c$, hard and soft magnetic materials are distinguished with $H_c \geq 100$ Oe $= 7958$ A/m, respectively $H_c \leq 5$ Oe $= 398$ A/m [11]. For example, iron is a hard magnetic material, whereas permalloy ($Ni_{80}Fe_{20}$) is soft magnetic.
Magnetism is being investigated at diverse scales [12]. On the atomic level (< 1 nm), the origin of magnetic moments, the exchange interaction and crystal anisotropies can be studied, as well as the spin arrangement on the lattice sites. The aim of this work is an analysis of the micromagnetic range, starting with the internal structure of domain walls ($1 - 1000$ nm) and the domain pattern, i.e., the detailed spatial arrangements of domains, in the range of $1 - 1000$ μm.

On larger scales (> 0.1 mm), the texture of magnetic materials is investigated and their phase diagrams are described, ignoring the detailed domain configuration. Finally, the average magnetization behavior of a sample can be studied by measuring the magnetic hysteresis in external magnetic fields, e.g. using SQUID magnetometry.

2.2 Spin polarization

Iron, cobalt and nickel are 3d-transition metals. Their electron system consists of a filled 4s shell and a partly filled 3d shell, with 6 electrons for iron and 8 electrons for nickel. The 3d electrons are localized, whereas the 4s electrons are the conduction electrons [13, 14]. As the latter move through the crystal, they interact with the 3d electrons by s-d-exchange interaction [15] effecting the spin. The densities of states of the localized 3d electrons are shifted due to the exchange energy for spin-up and spin-down, as illustrated in Fig. 2.2(a,b) for iron and nickel. Figure 2.2(c) presents a simplistic view. Since only the electrons in an interval of $\Delta E = \pm k_B T$ around the Fermi energy E_F serve as conducting electrons, the current consists of polarized electrons with the polarization [16]

$$P_N = \frac{N_\downarrow(E_F) - N_\uparrow(E_F)}{N_\downarrow(E_F) + N_\uparrow(E_F)} \,. \tag{2.3}$$

The polarization is equivalent to the difference in density of states between up and down electrons at the Fermi energy.

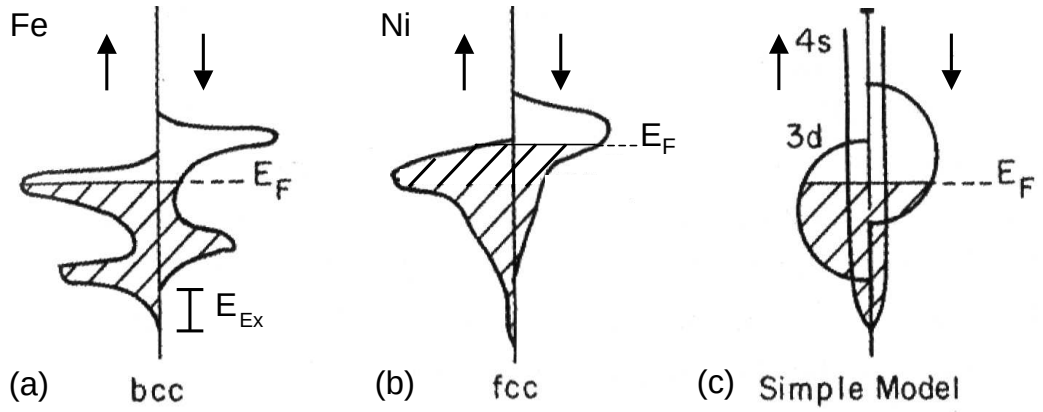

Figure 2.2: Sketch of the density of states for (a) iron, (b) nickel, and (c) a general simple model. The density of states of the localized spin-up and spin-down 3d electrons is shifted due to exchange interaction [17].

2.3 Energy contributions in ferromagnetism

In the calculation of the domain structure of ferromagnetic systems, several energies have to be taken into account [18]: The energy of the magnetization in an external magnetic field is called Zeeman energy and is determined by

$$E_H = -\int_V \vec{M}\vec{H}\, dV \tag{2.4}$$

with V being the volume of the ferromagnetic sample.
In its own stray field $\vec{H}_s$, the magnetization experiences the demagnetization energy. It is also called shape-anisotropy energy, because it depends not only on the volume but also on the form of the ferromagnetic sample. It has its origin in dipole interactions arising from free poles at the surfaces. The demagnetization energy can be written as

$$E_D = -\frac{1}{2}\int_V \vec{M}\vec{H}_s\, dV\,. \tag{2.5}$$

Ferromagnetism is a quantum mechanical effect caused by exchange interaction and accounted by the exchange energy [19, 20]:

$$E_{EX} = -2J\sum_{ij}\vec{S}_i\vec{S}_j\,. \tag{2.6}$$

J is called exchange integral. The exchange coupling is a short range interaction, so that only neighboring spins are effected. In the scalar product of the spin operators $\vec{S}_{i,j}$, the angle between the neighboring spins comes in. For $J > 0$, a parallel arrangement is energetically favored (ferromagnetism), whereas for $J < 0$ it is an antiparallel configuration.
The magneto-crystalline anisotropy energy depends on the crystal structure of the material. It favors the orientation of magnetic moments along certain easy axes. In bcc materials like iron, the easy axes are the $\langle 100\rangle$ directions [21], whereas the $\langle 111\rangle$ directions are hard axes. For fcc nickel, the case is just the opposite, and the fields required for saturation in the hard directions are smaller for Ni than for Fe. Without external fields, the magnetization tends to lie in the direction of the easy axes. In both cases, the anisotropy is called cubic and can be approximated as

$$\begin{aligned} E_K &= K_1\int_V \left(\cos^2\theta_1\cos^2\theta_2 + \cos^2\theta_2\cos^2\theta_3 + \cos^2\theta_3\cos^2\theta_1\right)\, dV \\ &+ K_2\int_V \left(\cos^2\theta_1\cos^2\theta_2\cos^2\theta_3\right)\, dV\,. \end{aligned} \tag{2.7}$$

Terms of higher order can usually be neglected. θ_i are the angles between the magnetization and the crystal axes, and $K_{1,2}$ are the anisotropy constants. Their sign defines the hard and easy axes, whereas their magnitude refers to the difficulty of being magnetized in the hard directions. For the materials used in this work, only the first term of eqn. (2.7) has to be taken into account. For example, the anisotropy constants K_1 for iron and nickel are $48\,000$ J/m^3 and $-5\,700$ J/m^3. Materials organized in a hexagonally close packed lattice have a uniaxial anisotropy. The easy axis is aligned along the c direction of the lattice cell. The uniaxial anisotropy energy can be approximated as

$$E_K = K_{u1} \int_V \sin^2 \phi \, dV + K_{u2} \int_V \sin^4 \phi \, dV \, . \tag{2.8}$$

Again, higher order terms are neglected. ϕ is the angle between the magnetization and the principal axis. K_{ui} are the uniaxial anisotropy constants. For the present materials, only K_{u1} is used. An example for a hexagonal ferromagnet is cobalt. Its anisotropy constant is $520\,000$ J/m^3. This reveals that saturating a cobalt sample in the hard direction of the basal plane of the lattice cell is more than a magnitude harder than saturating iron in the hard $\langle 111 \rangle$ directions.
A special hexagonal ferromagnetic material is permalloy ($\mathrm{Ni_{80}Fe_{20}}$), which is composed in such a way that the anisotropy constant almost vanishes and the material is exceptionally soft magnetic. Experimentally, the anisotropy constant can for example be measured by the magneto-optic Kerr effect (MOKE) [22, 23]. The constant is then deduced from the product of the saturation magnetization and the magnetic inductance needed for saturation in the hard direction ($K = M_s B_A/2$).
Finally, there are other energy contributions like magnetostriction or contributions from lattice defects and impurities, which are neglected in the calculations of this work. The energy of a ferromagnetic system results to be

$$E = E_H + E_D + E_{EX} + E_K \, . \tag{2.9}$$

2.4 Stoner-Wohlfarth model

The magnetization hysteresis can be calculated analytically for a single-domain particle with uniaxial anisotropy, which can result from both, shape or crystalline anisotropy. The particle magnetization is considered spatially uniform throughout the magnetization process. This is often referred to as Stoner-Wohlfarth problem, because they were the first to report a solution in 1948 [24]. In the following, a solution for a spherical particle consisting of a uniaxial material with anisotropy constant K in an external magnetic field B applied parallel to the easy axis, as sketched in Fig. 2.3(a), is described. The particle magnetization

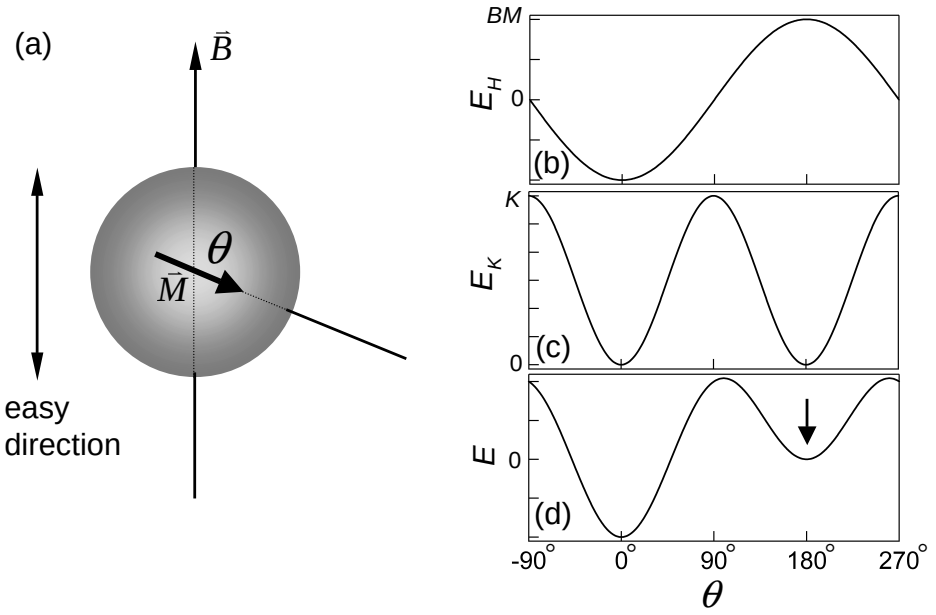

Figure 2.3: Stoner-Wohlfarth model: (a) Single-domain ferromagnetic particle with magnetization $\vec{M}$ lying at an angle θ with respect to the easy axis. Schematic illustration of the energy contributions, (b) Zeeman energy in an external field B and (c) anisotropy energy, and (d) the total energy. K is the anisotropy constant, B the external magnetic field, and $\vec{M}$ the magnetization of the particle.

$\vec{M}$ lies at an angle θ relative to the external field. For this problem, the following components of the total energy mentioned above in (2.9) have to be taken into account: The Zeeman energy $E_H = -BM\cos\theta$ and the anisotropy energy $E_K = K\sin^2\theta$ depend on the angle θ, whereas the demagnetization energy E_D and the exchange energy E_{EX} are constant because of the spherical symmetry and the parallel alignment of the magnetic moments, respectively. Thus, up to an irrelevant constant the total energy is equal to

$$E = K\sin^2\theta - BM\cos\theta\,. \tag{2.10}$$

The shape of the energy in configuration space is sketched in Fig. 2.3(b)-(d), where (b) and (c) illustrate the single contributions and (d) shows the total energy in an arbitrary external field B. At zero external magnetic field, only the anisotropy energy comes in (see Fig. 2.3(c)), and there are two local minima, one for $\theta = 0°$ and one for $\theta = 180°$, which correspond to the direction of the easy axis. We now consider the particle to be in the state indicated by the arrow in Fig. 2.3(d), i.e. $\theta = 180°$, so that the magnetization lies parallel to the easy axis pointing downwards (compare Fig. 2.3(a)). One can now calculate the magnetic field opposing the magnetization, that has to be applied to reverse the

magnetization of the particle, because with increasing external magnetic field, the local minimum at $\theta = 180°$ will disappear and the state of $\theta = 0°$ will be energetically favored. That means looking for the value of $B = B_{\text{switch}}$, at which the energy does not have a local minimum at $\theta = 180°$. An expansion for small angles φ around π with $\theta = \pi + \varphi$ gives

$$\begin{aligned} E(\pi+\varphi) &= K\sin^2(\pi+\varphi) - BM\cos(\pi+\varphi) \\ &\approx K\varphi^2 - \frac{1}{2}B_{\text{switch}}M\varphi^2 + B_{\text{switch}}M\,. \end{aligned} \tag{2.11}$$

With the condition $d^2E/d\varphi^2 < 0$ for a maximum, we find

$$B_{\text{switch}} > \frac{2K}{M}\,. \tag{2.12}$$

For example, permalloy has an anisotropy constant of $K = 100\ \text{J/m}^3$ and a saturation magnetization of $M_s = 860\,000\ \text{A/m}$. It follows that $B_{\text{switch}} = 0.2\,\text{mT}$. For iron with an anisotropy constant of $K = 48\,000\ \text{J/m}^3$ and a saturation magnetization of $M_s = 1\,700\,000\ \text{A/m}$ the switching field in this model is

$$B_{\text{switch}} = \frac{2 \cdot 48\,000\,\text{J/m}^3}{1\,700\,000\,\text{A/m}} = 56.5\,\text{mT}\,.$$

2.5 Domain formation and domain walls

In ferromagnetic particles, the domain configuration at zero magnetic field depends on the interaction of anisotropy energy, exchange energy and demagnetization energy. The anisotropy energy defines the direction of magnetization inside the domains, which will be parallel to the easy axes. The exchange energy causes

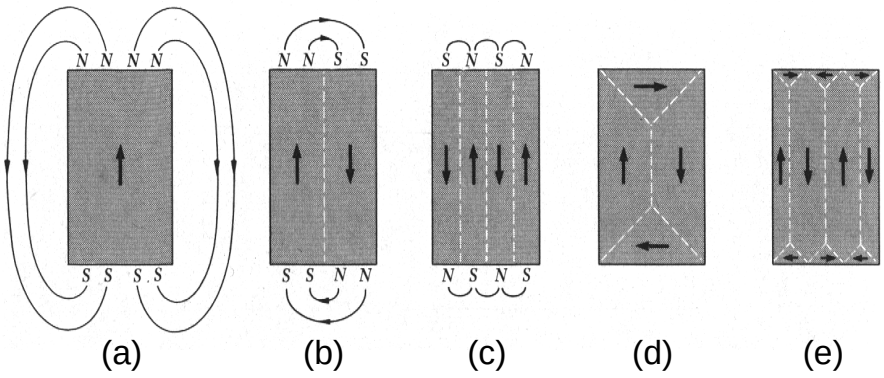

Figure 2.4: Domain patterns in small ferromagnetic particles. From left to right, the demagnetization energy is reduced by the formation of domains, especially by closure domains [12].

neighboring spins to be parallel to each other. Regarding these two energy contributions, a one-domain configuration with the magnetization pointing in the direction of the easy axis seems energetically favored (see Fig. 2.4(a)). However, also the demagnetization energy has to be taken into account. It counteracts a large stray field resulting from the domain configuration of the ferromagnetic particle. As shown in Fig. 2.4(a), the one-domain configuration would result in a large stray field, since the magnetic moments point perpendicular to the boundary of the particle. In the model of magnetic charges, this fact can be easily pictured, since a large number of magnetic charges is present at the boundary. The stray field is lowered by the formation of several antiparallel domains as illustrated in Fig. 2.4(b) and (c). However, the most effective configuration to decrease the stray field is the formation of boundary domains. In this so called flux-closure configuration (Fig. 2.4(d) and (e)), almost no stray field is present outside the particle, since no magnetic charges can be found at the boundaries. This flux-closure configuration is also referred to as "Landau pattern". The number of domains depends on size and shape of the particle. As explained below, the domain walls cause a stray field, which can be measured. To summarize, exchange energy and anisotropy energy are responsible for the formation of large areas with parallel magnetization, whereas the demagnetization energy causes the formation of several domains.

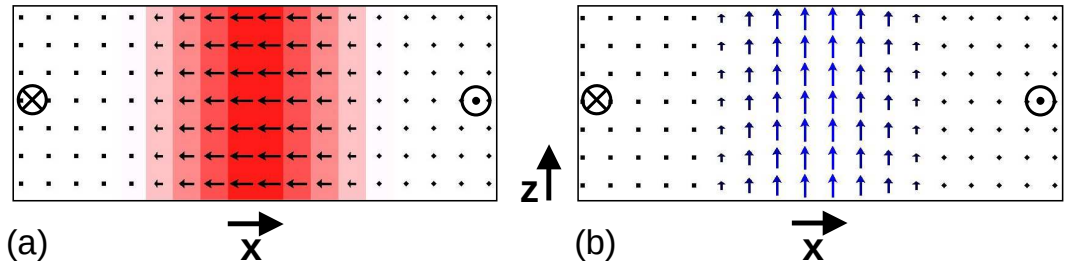

Figure 2.5: Two basic types of domain walls, (a) a Néel wall and (b) a Bloch wall as a cut through the particle. The film thickness is oriented along the z-direction.

The boundary between two domains is called domain wall. In this region, the magnetic moments have to turn by an angle of typically 90° or 180°. Here, the exchange energy is opposed to the anisotropy energy. The anisotropy energy favors a rapid change in magnetization, so that the magnetic moments lie parallel to the easy axis of the particle, whereas the exchange energy favors a slow change in magnetization between neighboring atoms. This results in a certain wall width a, which depends on material and thickness of the particle. Again the demagnetization energy is responsible for the shape of the resulting domain wall. There are basically two types of domain walls, which have to be distinguished. The first is called Néel wall [25] and is sketched in Fig. 2.5(a). Here the magnetization

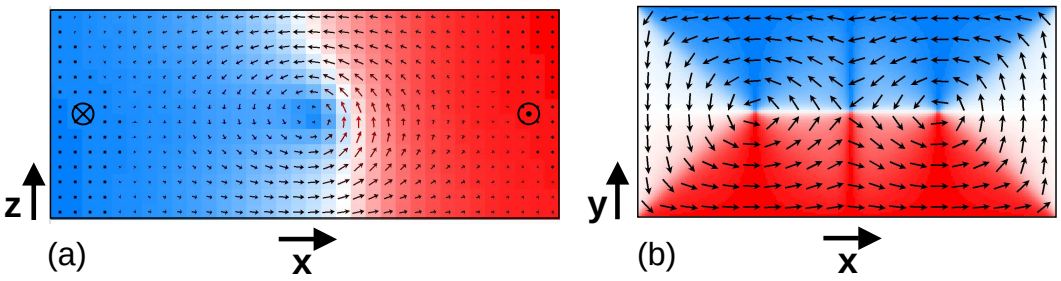

Figure 2.6: Two types of domain walls, which are a combination of a Néel and a Bloch wall, (a) shows an asymmetric Bloch wall in a 140 nm thick film and (b) a cross-tie wall in the center of a 1 μm×2 μm×20 nm large microstructure. Note that (a) is depicted as a cut through the particle with the film thickness in z-direction, whereas (b) illustrates a top view.

turns in the plane of the magnetization inside the two neighboring domains. For permalloy, this wall type is favored in thin films up to 40 nm (see below). In the second type, called symmetric Bloch wall (Fig. 2.5(b)), the magnetization points out of the plane in the middle of the wall before it turns back into the plane of the domains. This wall type is favored for thicker films, which can again be pictured in the model of magnetic charges. Depending on the thickness of the film, the distance between the magnetic charges is to be kept as large as possible. In thin films, the magnetic charges would be very close to each other in a Bloch wall, whereas in thicker films, a Néel configuration would result in close magnetic poles. This easy picture is supported by calculations of the domain wall energies of both wall types as shown below.

There are other types of domain walls, which can be thought of as combinations of Bloch and Néel contributions. Figure 2.6 shows two examples, which will be important later on. The first is an asymmetric or C-shaped Bloch wall [26, 27, 28, 29], shown in Fig. 2.6(a) as a cut through the particle. In this case, the 180° wall consists of a vortex structure in the interior and two Néel caps at the surfaces. The asymmetric Bloch wall exists in permalloy films with thicknesses above 100 nm [30, 31]. Figure 2.6(b) shows a top view of a cross-tie wall [32], which is a 180° wall, consisting of two vortices and a single point, where the magnetic moments are directed out-of-plane, representing the Bloch contribution. This causes “ties“, which reach into the antiparallel domains. In this area the wall is Néel like.

As a second analytical example for energy minimization after the Stoner-Wohlfarth problem described above, an estimation of the wall type and wall width as a function of film thickness in infinitely extended permalloy films without external magnetic fields will be presented, following calculations of Middelhoek [34]. At first, the wall energy of a 180° Bloch wall parallel to the easy axis will be ap-

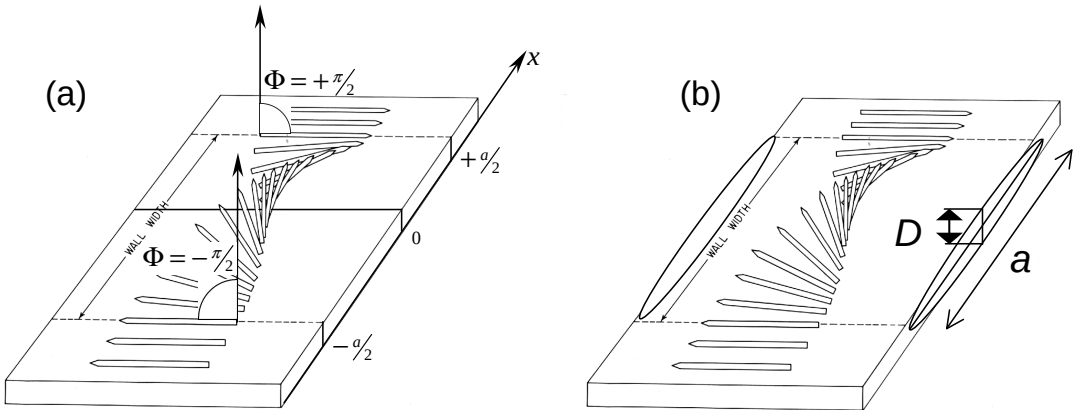

Figure 2.7: 180° Bloch wall with wall width a inside a thin film with thickness D. The parametrization of ϕ is sketched in (a). For the demagnetization term, the wall is approximated by a cylinder with elliptical cross section, as illustrated in (b) [33].

proximated, as illustrated in Fig. 2.7(a). The magnetization turns by an angle of 180° in the length of the wall width a. The angle between magnetization and the direction perpendicular to the film is called ϕ and is parameterized by $\phi = \pi(x/a)$ for $-a/2 < x < a/2$. Then, the energy contributions to the total energy in (2.9) are:

$$E_{EX} = A\left(\frac{d\phi}{dx}\right)^2 = A\left(\frac{\pi}{a}\right)^2 \tag{2.13}$$

$$E_K = \frac{1}{a}\int_{-a/2}^{a/2} K\cos^2\phi\, dx = \frac{1}{2}K \tag{2.14}$$

with A being the exchange constant and K the anisotropy constant. For the demagnetization energy, the wall is approximated by a cylinder with an elliptical cross section with the two axes a and D, where D is the film thickness (see Fig. 2.7(b)). An average magnetization M_{ave} is considered throughout the wall. With the demagnetization factor N for a cylinder with elliptical cross section [33], the stray field is $H_s = -NM_{\text{ave}} = -[4\pi a/(a+D)]M_{\text{ave}}$. Thus, the demagnetization energy density is

$$E_D = -\frac{1}{2}H_s M_{\text{ave}} = -\frac{1}{2}\left[-\frac{4\pi a}{a+D}M_{\text{ave}}\right]M_{\text{ave}} = \frac{2\pi a}{a+D}M_{\text{ave}}^2 \approx 2\pi M_{\text{ave}}^2 \tag{2.15}$$

for very thin films with $D << a$. Since the magnetization gradually changes its direction through the wall with the angle $\pi(x/a)$, the average magnetization can

be written as $M_{\text{ave}} = M_s \cos(\pi x/a)$, so that E_D becomes

$$E_D = \frac{1}{a} \int_{-a/2}^{a/2} 2\pi M_s^2 \cos^2(\pi \frac{x}{a})\, dx = \pi M_s^2 \tag{2.16}$$

and by comparison of equation (2.15) with (2.16) we find that $M_{\text{ave}} = M_s/\sqrt{2}$ in thin films.

In Fig. 2.8(a), the total energy of a Bloch wall per unit wall area γ_B is depicted. It is calculated by the sum of all components of the energy densities times the wall width a:

$$\gamma_B = A(\frac{\pi}{a})^2 a + \frac{1}{2} aK + \left[\frac{\pi a^2}{a+D}\right] M_s^2 \,. \tag{2.17}$$

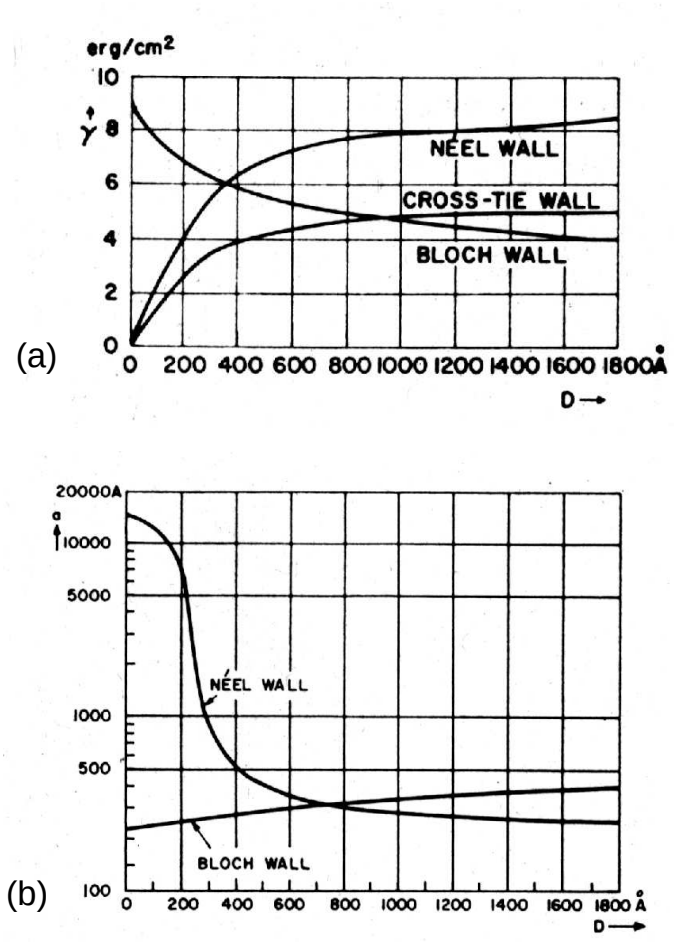

Figure 2.8: (a) Wall energy and (b) wall width of Bloch, Néel, and cross-tie walls in dependence of the film thickness as calculated by Middelhoek [34]. Note that the model is not suitable for cross-tie walls in the range of small film thicknesses since the approximation in equation 2.15 is not valid in that case.

In a Néel wall, the magnetization turns in the plane of the film by the angle $\phi = \pi(x/a)$ for $-a/2 < x < a/2$. However, now ϕ is the angle between magnetization and a direction normal to the wall, so in the plane of the film. The calculation of the energy density follows the same concept and reveals that, for film thicknesses below 40 nm, the total wall energy mainly consists of the demagnetization energy, whereas the wall width is determined by the exchange constant A and the anisotropy constant K. In comparison to the wall energy of a Bloch wall, Fig. 2.8(a) also illustrates the wall energy per unit area of a Néel wall depending on the film thickness. It can be seen that the Bloch wall energy decreases with increasing film thickness, whereas the Néel wall energy increases as discussed in the beginning of this section. Above a wall width of about 35 nm, a Bloch wall is energetically favored. The described model is not suitable for cross-tie walls for small film thicknesses. The energy of a cross-tie wall is treated in [31]. By minimizing the energy in (2.17) with respect to a, the wall width can be calculated in dependence of the film thickness D and is shown in Fig. 2.8(b) for Bloch and Néel walls. The wall width of Néel walls are much larger than those of Bloch walls, keeping in mind, that Néel walls only occur up to 35 nm film thickness in this model (see as well [5, 35]).

Chapter 3

Preparation and experimental setup

To investigate the micromagnetic behavior of structured ferromagnetic films in dependence of the film thickness experimentally, permalloy elements with different geometries and various thicknesses are prepared with electron-beam lithography and sputter deposition. The domain configurations of these particles are measured with magnetic-force microscopy in the as-prepared state, as well as in externally applied magnetic fields. The preparation process and the principle of magnetic-force microscopy are described in this chapter.

3.1 Preparation of ferromagnetic samples

The sample consists of permalloy rectangles in various sizes and several thicknesses, which are prepared by electron-beam lithography [36], permalloy sputtering, and a lift-off process. To achieve a wide range of film thicknesses, permalloy is partly deposited directly on the substrate and at the same time on top of an existing element. Therefore, electron-beam lithography requires a precise alignment. For this purpose, at first a marker system of gold is applied by optical lithography and thermal evaporation on a GaAs wafer. In a second step, the sample is coated with a double layer system of PMMA (Poly Methyl Methacrylate), namely a resist with a molecular weight of 950K on top of a resist with 50K. During exposure the molecules are cracked by the electron beam solubilizing them in the developer. The shorter molecules in the 50K resist are more easily cracked to soluble length than those of the 950K one. For this reason, the exposed and developed areas have a funnel shape as shown in Fig. 3.1(a) helping to reduce tear-off edges of permalloy at the boundaries of the single elements, that usually occur during lift-off (Fig. 3.1(c)). After electron-beam exposure, permalloy ($Ni_{83}Fe_{17}$) is deposited in a dc sputter process (Fig. 3.1(b)) described

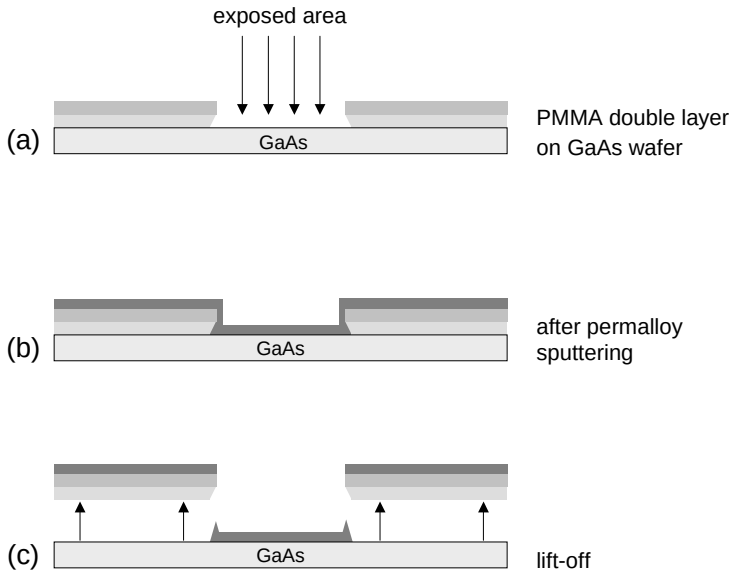

Figure 3.1: Preparation of the permalloy sample, showing (a) the funnel shape of the double layer of PMMA after exposure and development, (b) the sample with permalloy directly after the sputtering process, and (c) the sample after lift-off, completing the preparation process. During lift-off, tear-off edges can result as shown in (c), which can be partly avoided by using a double PMMA layer.

in detail in [37]. During a lift-off process with acetone the sample is cleaned from all undeveloped resist, so that only the exposed areas, coated with permalloy directly on GaAs, remain (see Fig. 3.1(c)). The preparation process, including the coating with PMMA resist, electron-beam lithography, permalloy sputtering, and the lift-off, is repeated five times with the same sample in order to achieve geometries with ten different film thicknesses next to each other, five of them prepared in a single process and five consisting of repeatedly sputtered material. The directly sputtered film thicknesses are 10 nm, 20 nm, 40 nm, 70 nm, and 100 nm. The assembled film thicknesses are 30 nm, 50 nm, 140 nm, and 170 nm. For a comparison, the thickness of 100 nm is prepared with both techniques. One sample comprises ten different lateral geometries (see Fig. 3.2(a)), namely 1 μm$\times$1 μm, 1 μm$\times$1.5 μm, 1 μm$\times$2 μm, 1 μm$\times$4 μm, 1.5 μm$\times$1.5 μm, 1.5 μm$\times$2 μm, 1.5 μm$\times$4 μm, 2 μm$\times$2 μm, 2 μm$\times$4 μm, and 4 μm$\times$4 μm. Figure 3.2(b) shows one group of elements with the same lateral geometry. The first row of particles nominally resembles the third prepared from the five directly sputtered films, and the second row comprises the same geometries as the fourth resulting from films sputtered on top of each other. This layout gives the possibility of measuring the domain pattern of the same lateral geometry in nine different film thicknesses in one measurement under exactly the same conditions, i.e. with the same MFM tip and in the same external magnetic fields.

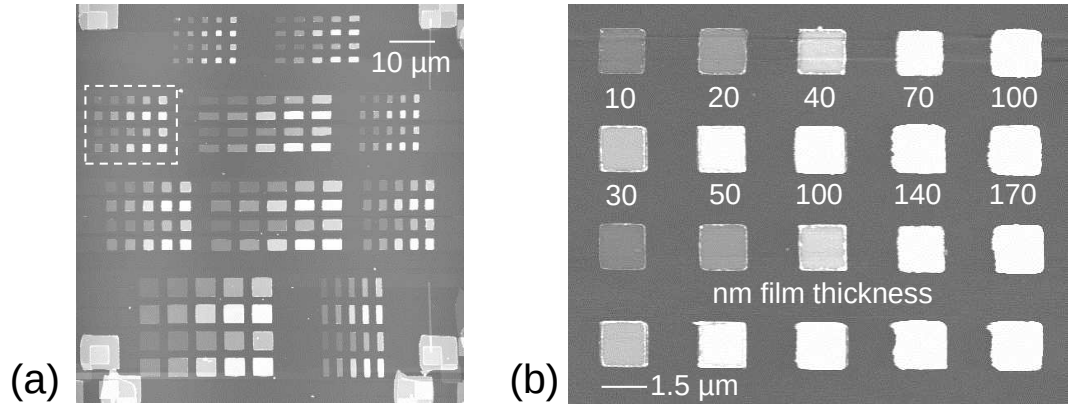

Figure 3.2: Topography of the permalloy sample measured by atomic-force microscopy, showing (a) ten different rectangular geometries in nine different film thicknesses, as shown in the group of 1.5 μm×1.5 μm sized elements as indicated by the white dashed frame in (a) and as a cut-out in (b). In the corners of the image in (a), parts of the alignment marks used in the preparation process can be seen.

3.2 Principles of magnetic-force microscopy

The operation principle of a magnetic-force microscope (MFM) is based on the technique of a scanning tunneling microscope [38, 39] and was first presented by Martin and Wickramasinghe in 1987 [40]. As shown in Fig. 3.3, the magnetic-force microscope consists of a cantilever with a tip coated with ferromagnetic material. The ferromagnetic sample to be measured is placed under the cantilever and can be moved via piezo electrical elements to be scanned line by line. The cantilever oscillates close to its resonance frequency at about 60-70 kHz. In a first scan the topography is measured in an atomic-force mode. The same line is afterwards scanned in the favored lift scan height of several 10 to 100 nm in the magnetic-force mode considering the topography of the sample so that the magnetic tip is always located in the same distance above the sample. Due to the interaction with the stray field of the ferromagnetic sample, the magnetic forces cause a phase shift in the oscillation of the cantilever which is detected by the reflection of a laser beam [41]. The phase shift is proportional to the force gradient in the direction perpendicular to the plane of the sample [42, 43, 44]:

$$\Delta\Phi \propto \hat{e}_z \nabla \vec{F} \,. \tag{3.1}$$

$\vec{F}$ is the force acting on the magnetic tip in the stray field of the ferromagnetic sample and is equal to the negative gradient of the Zeeman energy:

$$\vec{F} = -\nabla E_Z = \int\limits_{V_{Tip}} \nabla(\vec{M}\vec{H})\, dV \,. \tag{3.2}$$

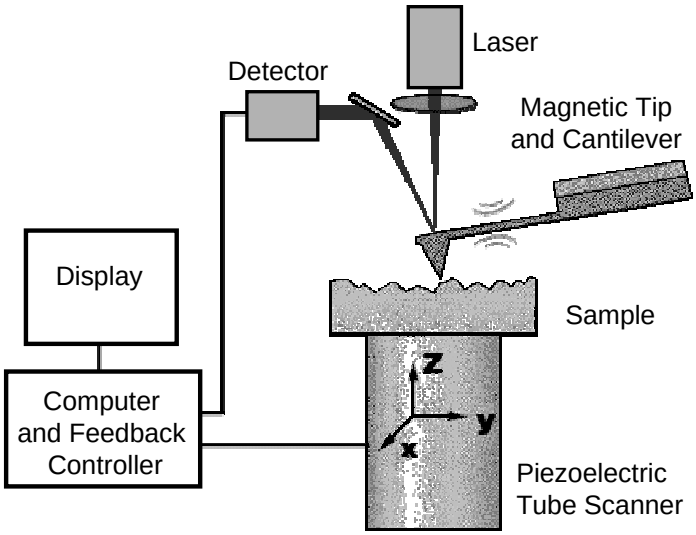

Figure 3.3: Measurement principle of a magnetic-force microscope.

Details of the interpretation of the MFM signal and an expansion of the computer code to calculate the signal will be discussed in the next chapter.
The present microscope is equipped with an integrated Helmholtz coil providing external magnetic fields of up to 100 mT. The resolution of magnetic-force microscopy depends on the radius of the magnetic tip of the microscope as well as on the tip-sample distance and lies between 10 and 100 nm [45]. An important advantage of magnetic-force microscopy is the fact that there are no requirements concerning the preparation of the samples. On the other hand, magnetic-force microscopy is a rather slow measurement technique. The magnetic-force microscope used for the present investigations is a Nanoscope IIIa sold by Digital Instruments/Veeco [46, 47, 48]. The interpretation of the resulting MFM images is not straightforward since the stray fields of all layers of the sample are superimposed in a complicated way. To interpret the measured signal, it is compared to simulations in the following chapters of this work.

Chapter 4

Micromagnetic simulations

All micromagnetic simulations presented in this work are based on the computer code called Oommf (for Object oriented micromagnetic framework) by M. Donahue and D. Porter (NIST) [49], founded on solving the Landau-Lifshitz-Gilbert (LLG) differential equation for the magnetization vector. The first section of this chapter will briefly introduce the LLG equation, specifying the energy contributions, the algorithm used by Oommf, and the material parameters. In the following, our extensions of this code based on results of the micromagnetic simulations are described, namely the signals of Hall μ-magnetometry and magnetic-force microscopy.

4.1 Object Oriented Micromagnetic Framework: Oommf

In chapter 2 the energy contributions for a ferromagnetic system are described in a continuous formulation. For a numerical calculation of the magnetization behavior of ferromagnetic elements, the problem needs to be discretized [50]. There are several possibilities [51]. To be able to treat a large range of possible particle shapes as rectangles, cylinders, and spheres, it would be advantageous to use a tetrahedral mesh where all cells are different, and an arbitrary surface could be sampled with any accuracy to account for the corresponding boundary conditions and surface effects. However, this non-periodic grid becomes inconvenient for the long-range demagnetization energy, in which the interaction of all cells has to be taken into account. For a non-periodic grid this means to evaluate all N^2 elements of the interaction matrix in each iteration or to keep them in memory, which becomes unacceptable already for small grids with 10^3 to 10^4 cells because of computing time or storage capacity problems, respectively. In contrast, for the periodic grid with cartesian coordinates, only the distance between the cells has to be taken into account so that the interaction matrix only consists of N

elements. Furthermore, mostly rectangular particles or at least volumes with flat surfaces are simulated. Therefore, a rectangular cartesian discretization is chosen as most adequate.
Until the three-dimensional code was available, the two-dimensional solver was used. The three-dimensional code offers two evolvers, the so called minimization evolver, which applies direct minimization techniques to find local minima in the energy surface, and a time evolver, that makes use of the LLG [52, 53, 54] equation. In this work, the latter type is chosen.
For the energy contributions to the total energy (compare equation (2.9)), the computer code offers diverse possibilities [55] of which the following are chosen:

- The external magnetic field is applied homogeneously, so that the Zeeman energy is uniform.

- For the demagnetization energy the magnetization is assumed to be constant in each cell. The average demagnetization field through the cell is computed after [56, 57]. The calculation of the demagnetizing field is the most time consuming part of the simulation.

- The exchange energy is chosen to be a standard six-neighbor exchange energy in the three-dimensional case. The exchange energy density contributed by a cell i is given by:

$$E_i = \sum_{j \in N_i} A \frac{\vec{m}_i \cdot (\vec{m}_i - \vec{m}_j)}{\Delta_{ij}^2}$$

  with N_i being the set of the six neighboring cells to cell i, A the exchange constant, which is considered uniform across all space, and Δ_{ij} the discretization step size between cells i and j. In the two-dimensional code, an eight neighbor exchange term is used [58, 59].

- The anisotropy energy requires the crystalline anisotropy constant K_1 and the anisotropy directions, which are chosen uniaxial for permalloy and cubic for iron. In both cases, the anisotropy directions are randomly varied cellwise across the mesh to account for the polycrystalline character of the ferromagnetic films. Also, a surface anisotropy can be included. However, this feature is neglected in the present simulations as suggested by [30, 60].

For the further calculations, an effective field $\vec{H}_{\text{eff}}$ acting on a given magnetic moment is introduced, which is defined as

$$\vec{H}_{\text{eff}} = -\frac{1}{\mu_0} \frac{\partial E}{\partial \vec{M}}$$

where E is the average energy density consisting of the above mentioned components, $\vec{M}$ is the pointwise magnetization and $\vec{H}_{\text{eff}}$ the pointwise effective field.

In this effective field, the magnetization will precess around the direction of the field, and the rate of change of the magnetization is equal to the torque:

$$\frac{d\vec{M}}{dt} = -|\bar{\gamma}|\vec{M} \times \vec{H}_{\text{eff}} ,$$

with $|\bar{\gamma}|$ being the Landau-Lifshitz gyromagnetic ratio ($2.211 \cdot 10^5$ m/(As)). In this formulation, the magnetization would precess without ever reaching an equilibrium. For a realistic description of the problem, a damping torque requires to be introduced into the equation of motion, describing the energy loss in the solid. The damping term has been expressed in different forms, which are all based on phenomenological considerations. Using the formulation of Landau and Lifshitz [52] the equation of motion is

$$\frac{d\vec{M}}{dt} = -|\bar{\gamma}|\vec{M} \times \vec{H}_{\text{eff}} - \frac{|\bar{\gamma}|\alpha}{M_s}\vec{M} \times \left(\vec{M} \times \vec{H}_{\text{eff}}\right) , \tag{4.1}$$

where α is a dimensionless damping coefficient. In each iteration of the simulation, as a first step the effective field $\vec{H}_{\text{eff}}$ is evaluated for all cells based on the current direction of the pointwise magnetization $\vec{M}$. Then the LLG equation is integrated in an iterative way [55, 61]. For the next iteration the value of the right hand side of equation (4.1) is extrapolated from the previous and the current value in a linear way. Then it is integrated across a new time interval Δt, giving a quadratic prediction for $\vec{M}$ at the next time step. This predicted value for $\vec{M}$ is inserted in the right side of equation (4.1), and $\frac{d\vec{M}}{dt}$ is evaluated. The resulting value is combined with the value of the current iteration by linear interpolation to obtain $\frac{d\vec{M}}{dt}$ across the new time interval Δt. At last, this resulting $\frac{d\vec{M}}{dt}$ is integrated to obtain a final estimate for $\vec{M}$ at the new step. If the maximum error between the predicted and the final estimate for $\vec{M}$ is below a certain value, and if the total energy of the system decreases with the new value for $\vec{M}$, the step is accepted. In that case, the error between predicted and final $\vec{M}$ is used to evaluate a new interval Δt for the next iteration. If, however, the step is rejected, the iteration is repeated with a reduced step size Δt.

Corresponding to the evolvers mentioned in the beginning of this section, the computer code uses so called drivers for the coordination of the simulation as a whole. A simulation run is divided into stages during which the problem parameters are not allowed to change in a discontinuous way. One stage consists of several iterations. During each iteration, the energy of the system is lowered, and if a certain stopping criterion is fulfilled, the stage is complete. For example, an external magnetic field is increased in several steps, being constant during one stage and changed as soon as the next stage is reached, so that for each applied field the energy is minimized. The stopping criteria for a completed stage are either an iteration limit, a time limit, which refers to the time in the LLG equation, or a value for $d\vec{m}/dt$ (with $\vec{m}$ being the normalized magnetization), so that

Table 4.1: Material parameters for common ferromagnetic materials with M_s saturation magnetization, A exchange constant, K_1 anisotropy constant, B_s magnetic inductance of saturation, $K_d = B_s^2/(2\mu_0)$ stray field coefficient , and $L_{ex} = \sqrt{A/K_d}$ exchange length [49, 62].

material parameters	**permalloy**	**iron**	**nickel**	**cobalt**
M_s [A/m]	860 000	1 700 000	490 000	1 400 000
A [J/m]	13×10^{-12}	21×10^{-12}	9×10^{-12}	30×10^{-12}
K_1 [J/m^3]	100	48 000	-5 700	520 000
derived quantities				
B_s [T]	1.081	2.136	0.616	1.758
K_d [J/m^3]	464 960	1 815 360	150 980	1 231 100
L_{ex} [nm]	5.3	3.4	7.7	4.9

the criterion is fulfilled, if $|d\vec{m}/dt|$ across all magnetic moments drops below the specified value. This latter condition is used in the present simulations and is chosen to be in the range of 0.001 to 0.01 degree per nanosecond. Due to the limited numerical precision of the energy calculations, it is usually not possible to obtain values much below 0.001 degree per nanosecond [55].
The material parameters used for the simulations are summarized in table 4.1. For comparison, the data for nickel and cobalt are as well presented although the simulations are performed on permalloy and iron only. For simulations with a two-dimensional grid, the cell size in the direction perpendicular to the plane of the particle is always as thick as the particle. For three-dimensional simulations, the cells are chosen to be cubic. The favorable cell size depends on the exchange length of the material (see table 4.1) and should be of similar magnitude. However, the computing time depends strongly on the number of cells so that compromises need to be considered. The cell size was chosen between 5 nm (mostly for iron) and 10 nm (mostly for permalloy). The damping parameter α is selected to be 0.5, which is large compared to experimental values, but results in a faster convergence of the simulation. Only for accurate dynamic studies not performed in the framework of this thesis, the damping needs to be chosen adequately [30, 63]. Further, an initial magnetization has to be defined. This can be done by a vector script, making it possible to define for example patterns consisting of several domains, a vortex structure or a homogeneous magnetization. Also a random distribution of magnetic moments can be chosen. Since the iteration process leads to local energy minima rather than to absolute minima, the final magnetization pattern depends also on the history of the simulation, i.e., on the initial magnetization. Especially in the case of a random initial magnetization,

two simulation processes do not yield the same result, unless exactly the same random distribution is used. So the favorable initial magnetization depends on the problem and is not unique in the present simulations. If several simulations with different initial magnetization patterns are performed, the total energy of the system can be compared for all resulting magnetization configurations in order to select the energetically favorable one. It has to be mentioned that also in experiments different domain patterns can result for exactly the same samples. Besides the simulations, this also proves that the energies of the different configurations can be in close proximity to each other.
The output of the computer program consists of several parts. One is an array of magnetization vectors, which can be displayed in Oommf, illustrating the detailed domain configuration with the resolution of the cell size. Examples are shown in Figs. 2.5-2.6 in chapter 2. The other is a list of diverse parameters, including among others the energy contributions as well as the total energy, the magnetization components M_x, M_y, and M_z, the maximum torque $|\vec{M} \times \vec{H}|$, the values corresponding to the stopping criteria, the iterations needed for the preceding step, and the maximum angle between neighboring magnetic moments [59].
The integral magnetization can be plotted versus the external magnetic field to achieve a hysteresis curve. This simulated data is to be compared to experimental results. On the one hand, the stray field in a section of a ferromagnetic particle can be measured by Hall μ-magnetometry in dependence of an external magnetic field [64] and can be compared to the simulated integral magnetization. In that case, the magnetic field of saturation or irreversible changes in the signal can be analyzed. For quantitative investigation the computer code is expanded so as to simulate the Hall μ-magnetometry signal as described in the next section. On the other hand, the domain configuration can be visualized experimentally by magnetic-force microscopy (MFM), as described in the previous chapter. However, the interpretation of the measured signal in comparison to the simulated magnetization pattern is not straightforward. For a direct comparison between simulation and experiment, a signal corresponding to the experimental signal is calculated from the simulated data for both measurement techniques, as presented in the following.

4.2 Simulation of Hall μ-magnetometry

By means of Hall μ-magnetometry [65], the stray field of a ferromagnetic particle is measured making use of the Hall effect [66]. The Hall effect is based on the Lorentz force $\vec{F}_L = -e\left(\vec{v} \times \vec{B}\right)$ acting on a moving electron in a magnetic field. If the magnetic field is applied perpendicular to the current, this results in the Hall voltage U_H in the direction perpendicular to the current I and to the magnetic

field B. A material parameter is the Hall coefficient, which is defined as:

$$R_H = \frac{U_H d}{IB} = \frac{1}{n_e e}\,.$$

n_e is the three-dimensional electron density and d the particle thickness. The external field can for example be the stray field of a ferromagnet. For the measurement, the ferromagnetic particle has to be prepared on top of a Hall bar as sketched in Fig. 4.1 [64]. The stray field generated by that section of the ferromagnetic particle lying directly above the so called Hall cross is measured in a distance of 90 nm under the surface of the element by analyzing the Hall effect in the two-dimensional-electron system (2DES) [67]. Details of the preparation process and the experimental setup are described in the publication [P2] in chapter 5.

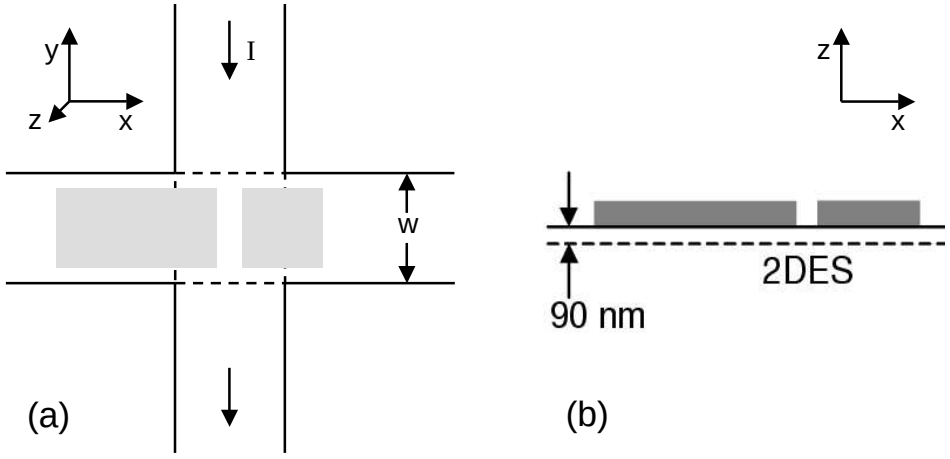

Figure 4.1: Pair of ferromagnetic contacts on a Hall cross, (a) as a top view and (b) as cross section along the x axis.

The signal measured is the out-of-plane component of the stray field generated by the ferromagnet averaged over the sensor area. The corresponding signal can be easily calculated from the simulation data, if the output is interpreted as an array of magnetic dipoles, so that each cell is described by one dipole (see Fig. 4.2). Their direction is determined by the output data of the simulation. The magnitude of the magnetic dipoles is given by multiplying the data with the volume of a lattice cell and the saturation magnetization of the material. The stray field of such a dipole is calculated by the common formula [68]:

$$\vec{H} = \frac{1}{4\pi}\left[\frac{3(\vec{r}\vec{m})\vec{r}}{r^5} - \frac{\vec{m}}{r^3}\right]\,. \tag{4.2}$$

Here, $\vec{m}$ is the magnetic dipole moment of the dipole in the lattice cell of the particle, and $\vec{r}$ is the distance in which the stray field is to be calculated with

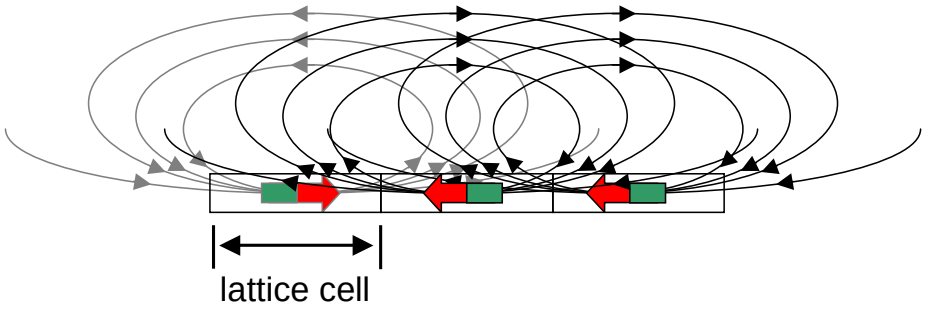

Figure 4.2: Schematic view of the stray field of magnetic dipoles, which represent the magnetization of individual lattice cells used in the simulation.

respect to the magnetic dipole. If the stray fields of all magnetic dipoles in the array are superimposed, the stray field generated by the particle is obtained. Since the 2DES in the Hall magnetometer is solely sensitive to the out-of-plane or z component of the stray field, only the z component has to be calculated. The actual Hall μ-magnetometer signal is sensitive to the average field component

$$\langle H_z \rangle = \frac{1}{w^2} \int_{x_{\min}}^{x_{\max}} \int_{y_{\min}}^{y_{\max}} H_z(x,y)\, dx\, dy\,. \tag{4.3}$$

Here, w is the electronic width of the Hall cross (compare Fig. 4.1(a)). The calculation of the stray field facilitates the direct comparison between Hall-magnetometry and simulation and enables a quantitative analysis.

4.3 Simulation of magnetic-force microscopy

As already mentioned in the previous chapter, the signal of magnetic-force microscopy is proportional to the phase shift (see equation (3.1)) of the oscillating cantilever resulting from the stray field of the ferromagnetic sample which is to be measured. The Zeeman energy, which causes the force on the magnetic tip, can be calculated with help of the approximation that the magnetic tip can be thought of as a magnetic dipole [69] inside the volume of the tip [70] with the dipole moment $\vec{m}$. Then equation (3.2) can be calculated as follows:

$$\vec{F} = -\nabla E_H = \int_{V_{Tip}} \nabla(\vec{M}\vec{H})\, dV = \nabla(\vec{m}\vec{H}) = \begin{pmatrix} \frac{\partial}{\partial x}(\vec{m}\vec{H}) \\ \frac{\partial}{\partial y}(\vec{m}\vec{H}) \\ \frac{\partial}{\partial z}(\vec{m}\vec{H}) \end{pmatrix} \tag{4.4}$$

with the magnetization

$$\vec{m} = \int_{V_{Tip}} \vec{M}\, dV \tag{4.5}$$

of the tip. In the right part of equation 4.4 the point dipole approximation enters. $\vec{H}$ is the stray field of the sample. Further the orientation of the magnetic dipole moment of the MFM tip can be considered in z-direction (out-of-plane) only, so $m_x = m_y = 0$. Then:

$$\vec{F} = \begin{pmatrix} \frac{\partial}{\partial x} \sum_{i=1}^{3} m_i H_i \\ \frac{\partial}{\partial y} \sum_{i=1}^{3} m_i H_i \\ \frac{\partial}{\partial z} \sum_{i=1}^{3} m_i H_i \end{pmatrix} = \begin{pmatrix} \sum_{i=1}^{3} m_i \frac{\partial H_i}{\partial x} \\ \sum_{i=1}^{3} m_i \frac{\partial H_i}{\partial y} \\ \sum_{i=1}^{3} m_i \frac{\partial H_i}{\partial z} \end{pmatrix} = \begin{pmatrix} m_z \frac{\partial H_z}{\partial x} \\ m_z \frac{\partial H_z}{\partial y} \\ m_z \frac{\partial H_z}{\partial z} \end{pmatrix} . \tag{4.6}$$

As a final approximation, it can be assumed that $\frac{\partial H_z}{\partial x}, \frac{\partial H_z}{\partial y} << \frac{\partial H_z}{\partial z}$, so the signal measured by magnetic-force microscopy is proportional to the second derivative of the z component of the stray field in z-direction:

$$\Delta\Phi \propto \hat{e}_z \nabla \vec{F} = \frac{\partial F_z}{\partial z} = m_z \frac{\partial^2 H_z}{\partial z^2} . \tag{4.7}$$

The derivatives of the stray field are calculated in detail in appendix A. In the present computer code, the last approximation is not needed and the full set of derivatives $\partial H_z/\partial x$, $\partial H_z/\partial y$, and $\partial H_z/\partial z$ can be included. The computer code for the simulation of measurement signals developed in this work has also been used by other groups [71, 72].

Chapter 5

Results for permalloy and iron contacts

In this chapter, the results of micromagnetic simulations in comparison to experiments are presented. Large parts of the results have already been published, and the publications are included in this chapter with a small introduction. Supplementary results to the publications are shown. The publications are presented in chronological order to illustrate the necessity of simulating measurement signals for a better comparison and the successful application of these calculations.

5.1 Permalloy contacts in external fields

In the following publication [P1], permalloy contacts are investigated by means of magnetic-force microscopy in comparison to micromagnetic simulations at zero magnetic fields as well as by simulations in external magnetic fields. The micromagnetic behavior of the electrodes is examined in a pair of contacts and in the single electrodes to learn about the interaction between them. The contacts investigated experimentally have a size of 1 μm$\times$1 μm and 1 μm$\times$2 μm with a distance of 200 nm between them. The simulations in external magnetic fields are performed on smaller electrodes with a size of 0.5 μm$\times$0.5 μm and 0.5 μm$\times$1 μm for computational reasons. For the present calculations, the two dimensional code is employed, so that the cell size in the z-direction (out of plane) corresponds to the film thickness of 20 nm. The cell size in the plane of the particle is chosen to be 10 nm. The material parameters for permalloy are taken from table 4.1.

JOURNAL OF APPLIED PHYSICS VOLUME 89, NUMBER 11 1 JUNE 2001

Investigation of ferromagnetic microstructures as electrodes for spin-polarized transport experiments

G. Meier,[a] M. Halverscheid, T. Matsuyama, and U. Merkt
Universität Hamburg, Institut für Angewandte Physik and Zentrum für Mikrostrukturforschung, Jungiusstraße 11, D-20355 Hamburg, Germany

Patterned ferromagnetic structures are intended as electrodes to drive a spin-polarized current through the quasi two-dimensional electron system of a semiconductor. To utilize such structures in transport experiments it is important to know their micromagnetic behavior. We have prepared Permalloy electrodes for the ballistic transport regime by electron-beam lithography on InAs single crystals. Using magnetic-force microscopy we measure the magnetization configurations at zero external magnetic fields. Micromagnetic simulations verify that the observed magnetization states are the energetically most favorable ones. In addition, the micromagnetic behavior in external magnetic fields is simulated. © *2001 American Institute of Physics.* [DOI: 10.1063/1.1355350]

I. INTRODUCTION

A great deal of interest has been paid to the investigation of spin-polarized transport in ferromagnet-normal-metal-systems[1,2] and more recently in ferromagnet-semiconductor systems.[3–5] In metal systems spin transport is feasible and has proven to be very successful.[2] The underlying spin-dependent scattering effects have improved the sensitivity of magnetic field sensors such as read heads of hard disks by at least an order of magnitude. However, in metal systems spin transport can only be influenced by magnetic fields. Hybrid systems incorporating semiconductors would provide the possibility of tuning the coherent spin state by electric fields. While for the diffusive regime significant spin injection from ferromagnetic metals into semiconductors seems to be difficult,[6] there is an ongoing discussion for the ballistic limit. New theoretical work predicts effects of up to several 10% in this regime.[7] The electrode structures described here fulfill this requirement since the spacing between the electrodes is smaller than the ballistic mean free path in the semiconductor. A second important prerequisite is the lack of inversion symmetry in the semiconductor that leads to strong spin orbit interaction.[8] In this regard InAs is a semiconductor of choice since it exhibits a strong spin orbit interaction which can be tuned by a gate voltage.[9,10] This is a central goal for a tunable spin dependent transport device.[11] Even so, a profound understanding of the micromagnetic behavior of two interacting ferromagnetic electrodes applied in all of the hybrid systems mentioned above is crucial.

II. EXPERIMENTS

We have deposited asymmetric Permalloy electrode pairs on InAs single crystals by electron-beam evaporation in the low 10^{-8} mbar pressure range. Their asymmetric geometry provides different micromagnetic behavior and thus different switching fields in external magnetic fields. This is desirable for the investigation of effects of different magnetization states on the resistance of the device. Permalloy is chosen because it combines a high saturation magnetization with a considerable degree of spin polarization (40%) of the charge carriers at the Fermi energy.[12] The composition of the electrode structures was determined by energy dispersive x-ray (EDX) analysis to be 80% Ni and 20% Fe, which is the desired ratio to minimize magnetostriction.[13]

We have utilized magnetic-force microscopy (MFM) in the LiftMode™[14] to image the electrodes at remanence and found magnetization patterns for the *single* structures that have been reported previously with MFM and other techniques.[15,16] In all of the four smaller electrodes shown in the MFM image in Fig. 1 the magnetization exhibits a Landau pattern. In the larger electrodes on the left sides two possible magnetization patterns are observed: a double Landau structure (upper right) and a magnetization pattern with long side domains in the other three electrode configurations.

III. RESULTS AND DISCUSSION

To describe the observed magnetization states we have simulated the micromagnetic behavior of the single electrodes and of complete electrode pairs using a computer code supplied by Porter and Donahue.[17] This code numerically integrates the Landau–Lifshitz–Gilbert equation. A solution of this equation represents a local energy minimum. It depends essentially on the chosen start configuration which local minimum is finally reached. We have checked different

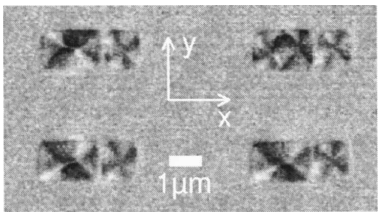

FIG. 1. Magnetization patterns of four Permalloy electrode pairs on a *p*-type InAs(100) single crystal measured with magnetic-force microscopy at room temperature. The electrodes are patterned from an 18-nm-thick Permalloy layer covered by 9 nm Au as protective cap.

[a]Electronic mail: meier@physnet.uni-hamburg.de

7470 J. Appl. Phys., Vol. 89, No. 11, 1 June 2001 Meier *et al.*

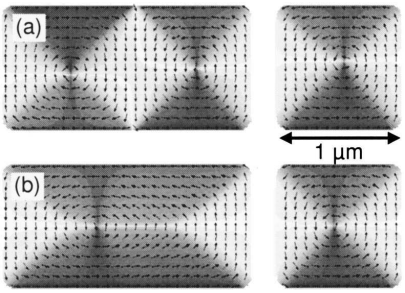

FIG. 2. Magnetization states at remanence of two 20-nm-thick Permalloy electrode structures 200 nm apart calculated from different start configurations. The total energy for pattern (a) is 704 eV and for (b) 734 eV. An angle dependent gray scale is used to emphasize the magnetization state. The rounded corners are introduced to improve the correspondence between real and simulated geometry. As material parameters a saturation magnetization $M_s = 800$ kA/m, an exchange constant $A = 13 \times 10^{-12}$ J/m, and an anisotropy constant $K_1 = 500$ J/m^3 are used. In both cases the smaller electrode exhibits a Landau structure while for the larger electrode a double Landau structure (a) and a magnetization pattern with longer side domains (b) are calculated.

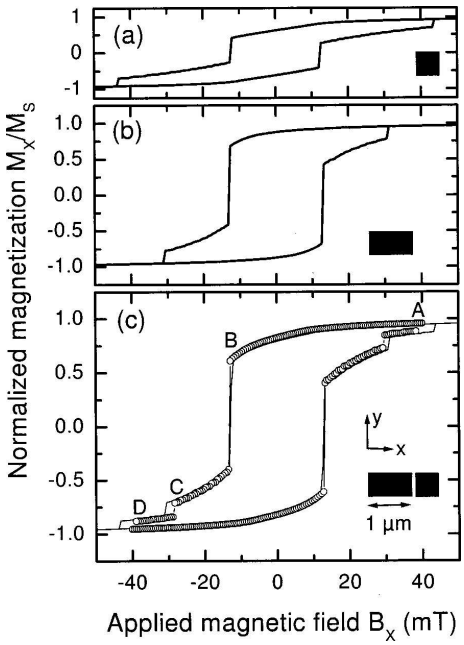

FIG. 3. Calculated hysteresis curves of Permalloy electrodes for (a) a single small electrode, (b) a single large electrode, and (c) their combination. The magnetic field is applied along the *x* direction and the normalized magnetization is plotted. In (c) the sum of the hysteresis curves from (a) and (b) (solid line, no interaction) and a hysteresis curve calculated for both electrodes together (open symbols, with interaction) is shown. The lettering relates to the magnetization patterns shown in Fig. 4.

start configurations and found that after the energy minimization the two magnetization patterns with the lowest energies (see Fig. 2) are the ones measured with MFM. Note that the MFM signal is proportional to the second derivative of the stray field of the investigated object in the direction of the tip magnetization while the simulated images depict the magnetization directly. The rather good agreement is a strong hint at the absence of magnetostriction in the Permalloy–InAs system that in fact needs not be considered in the simulation.

In the following we discuss the micromagnetic behavior of the electrode pair in Fig. 3 in an external magnetic field added step by step in the simulation. Although these calculations are performed on smaller electrode structures for the purpose of reducing the computing time to reasonable values, the general, idea is not altered and especially the magnetization states at remanence exhibit the same pattern as in the larger electrodes described above. In contrast to an earlier publication[18] where the external field is applied in the *y* direction resulting in a spin-valve geometry, in this article we investigate the electrode pair in a field applied in the *x* direction which is the current direction in a ballistic spin transistor device [see Fig. 3(c)].

To understand the shape of the resulting hysteresis curves it is useful to calculate the micromagnetic behavior for each single electrode. The virgin curves—not shown here—are calculated by increasing the field by 0.53 mT in 75 steps up to a maximum field of $B_x = +40$ mT where a nearly saturated magnetization state in the *x* direction is reached. The hysteresis curves are completed by calculating all energy minima at external magnetic fields between +40 mT down to −40 mT and back again to +40 mT in 300 steps. The resulting hysteresis curves for the individual structures are shown in Figs. 3(a) and 3(b) both exhibiting two irreversible jumps on the way from the nearly saturated state at positive and negative field values, respectively. For the smaller structure the second jump appears at a higher value of B_x. To obtain the hysteresis curve for the limiting case of a noninteracting electrode pair one can add the individual curves taking into account their volumes [see Fig. 3(c), solid curve]. A simulation of both electrodes together for an electrode spacing of 100 nm is plotted for comparison. The number of irreversible jumps is the same for both curves indicating that the general micromagnetic behavior is unchanged. Due to magnetostatic interaction the values of the switching fields are slightly reduced. We have calculated the hysteresis curves for different electrode spacings (30, 80, 100, 150, 250, 400, and 500 nm) and found a monotonous behavior with the asymptotic hysteresis curve of noninteracting electrodes approximately reached at 500 nm electrode spacing.

Within the remaining space we discuss the magnetization patterns which are important for transport experiments. We start with the nearly saturated state at $B_x = +40$ mT [point A in Fig. 3(c)]. The corresponding magnetization pattern is shown in Fig. 4(a). While the magnetic moments some distance from the edges are nearly aligned in the *x* direction as a genuine spin-transistor geometry would require[11] the local magnetic moments next to the structure edge bend away from this direction to minimize the demagnetization energy contribution. If the external field is reduced to a value of −12.8 mT [point B in Fig. 3(c)] the moments in the two electrodes are aligned antiparallel in the *y* direction

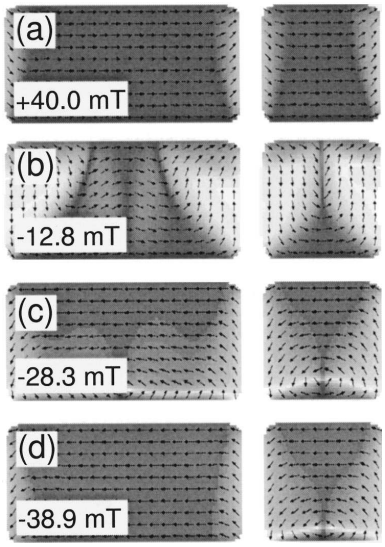

FIG. 4. Simulated magnetization state of two Permalloy electrodes at different values of the applied magnetic field. The magnetization patterns correspond to the lettering in Fig. 3(c).

approximating the spin-valve situation. At a field value of $B_x = -28.3\,\mathrm{mT}$ the magnetization in large areas of both electrodes has reversed its direction [Fig. 4(c)]. The next magnetization jump occurs at $B_x = -38.9\,\mathrm{mT}$ [Fig. 4(d)] where the magnetization of the larger electrode is already in a magnetization state near to saturation. Finally, at $B_x = -40\,\mathrm{mT}$ the magnetization of the small electrode has switched, too, and a magnetization state close to saturation magnetization is reached again.

In conclusion, rather good agreement between the experimentally observed magnetization patterns in electrode configurations for ballistic transport measured by MFM in zero external magnetic field and micromagnetic simulations is obtained. The micromagnetic behavior in external magnetic fields is analyzed and discussed. It is clear that an experimental proof of the calculated micromagnetic behavior is important and can be done with a magnetic-force microscope with integrated coils to apply the required fields as demonstrated by Gomez, Burke, and Mayergoyz for isolated structures.[15] Such an experiment would give important feedback to micromagnetic simulations.

ACKNOWLEDGMENTS

The authors would like to thank R. Wiesendanger for his advice and help in magnetic-force microscopy and W. Pfützner for Permalloy evaporation and EDX analysis of the electrode structures. The authors acknowledge financial support of the Deutsche Forschungsgemeinschaft via the Sonderforschungsbereich 508 ''Quantenmaterialien'' and by the NEDO international joint research grant program.

[1] P. Grünberg, R. Schreiber, Y. Pang, M. B. Brodsky, and H. Sowers, Phys. Rev. Lett. **57**, 2442 (1986).
[2] G. A. Prinz, Phys. Today **48**, 58 (1995).
[3] F. G. Monzon and M. L. Roukes, J. Magn. Magn. Mater. **198**, 632 (1999).
[4] P. R. Hammar, B. R. Bennett, M. J. Yang, and M. Johnson, Phys. Rev. Lett. **83**, 203 (1999).
[5] C. M. Hu, J. Nitta, A. Jensen, J. B. Hansen, and H. Takayanagi Phys. Rev. B (accepted).
[6] G. Schmidt, D. Ferrand, L. W. Molenkamp, A. T. Filip, and B. J. van Wees, Phys. Rev. B **62**, R4790 (2000).
[7] D. Grundler, Phys. Rev. Lett. (accepted).
[8] E. A. de Andrada e Silva, G. C. La Rocca, and F. Bassani, Phys. Rev. B **55**, 16293 (1997).
[9] T. Matsuyama, R. Kürsten, C. Meißner, and U. Merkt, Phys. Rev. B **61**, 15588 (2000).
[10] D. Grundler, Phys. Rev. Lett. **84**, 6074 (2000).
[11] S. Datta and B. Das, Appl. Phys. Lett. **56**, 665 (1990).
[12] R. J. Soulen *et al.*, Science **282**, 85 (1998).
[13] A. Hubert and R. Schäfer, *Magnetic Domains—The Analysis of Magnetic Microstructures* (Springer, Berlin, 1998).
[14] V. Elings and J. Gurley, US Patent No. 5,308,974 (1994), Digital Instruments, Santa Barbara, CA, May 3, 1994.
[15] R. Gomez, E. Burke, and I. Mayergoyz, J. Appl. Phys. **79**, 6441 (1996).
[16] A. Johnston, J. Chapman, B. Khamsehpour, and C. Wilkinson, J. Phys. D **29**, 1419 (1996).
[17] Oommf, object oriented micromagnetic framework, http://math.nist.org/oommf
[18] G. Meier and T. Matsuyama, Appl. Phys. Lett. **76**, 1315 (2000).

5.2 Interaction between two contacts

As mentioned in the previous publication [P1], the pairs of permalloy contacts are further examined by micromagnetic simulations. Therefore, the two rectangles with a size of 0.5 μm×0.5 μm and 0.5 μm×1 μm are placed in various distances to each other, namely 30, 50, 80, 100, 150, 250, 400, and 500 nm. Note that this corresponds to a distance twice as large if compared to the larger contacts with a size of 1 μm×1 μm and 1 μm×2 μm. In Fig. 5.1 the simulated hysteresis curves, namely the magnetization in the direction of the external field plotted versus the external field, are shown for selected distances between the contacts. Here the magnetic field is applied along the easy axis of the contacts. The remanence of the particles is similar in all cases. Also the first irreversible changes in magnetization - coming from positive magnetic fields - take place at almost identical magnetic field strengths at -13 to -16 mT. For a better overview, a close-up of the last irreversible steps before negative saturation is shown in Fig. 5.2. This figure reveals that in general two irreversible steps proceed saturation. With increasing particle distance, the field needed for saturation increases, meaning that the interaction between the contacts becomes smaller. As an exception, the particles with a distance of 50 nm have the smallest saturating magnetic field. This is connected to the fact that here only one irreversible change in magnetization leads to saturation. In Fig. 5.3 the magnetic fields for the last irreversible steps are plotted for all investigated distances between the contacts (see open circles). Except for 50 nm, the field strength of the last irreversible step becomes stronger with increasing particle distance, revealing smaller interaction with increasing

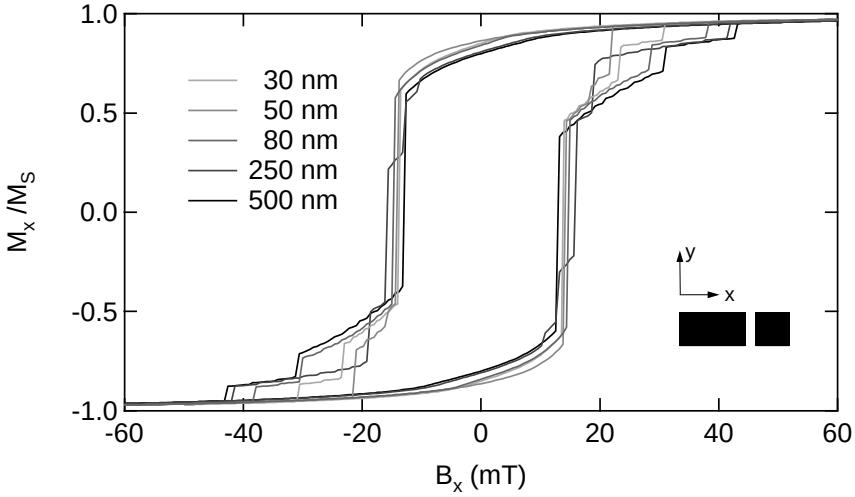

Figure 5.1: Hysteresis curves for particles with selected distances as noted in the graph. The external field is applied along the long axis of the contacts.

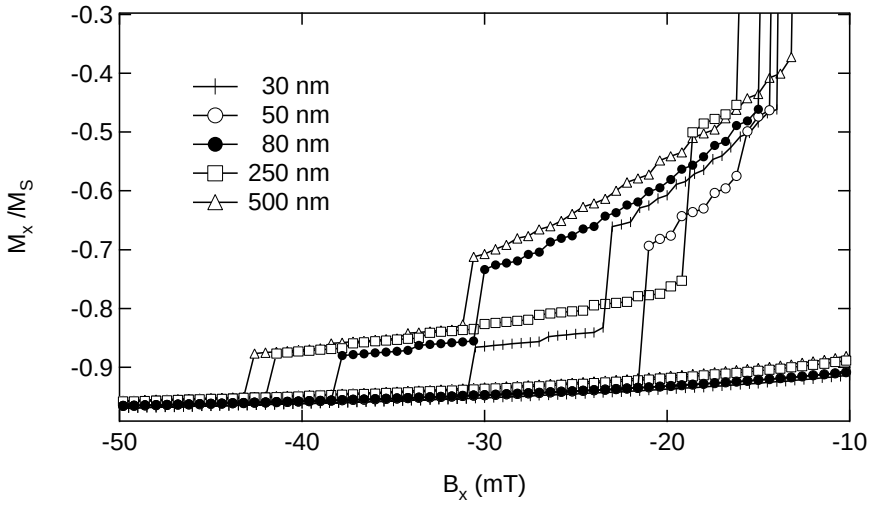

Figure 5.2: Cut-out of the hysteresis curves shown in Fig. 5.1.

distance. The question remains, how far the interaction between the contacts does reach. This is shown in Fig. 5.4. Here, as in the publication, the sum of the hysteresis curves of the single small and the single large contacts is plotted in comparison to the interacting electrodes with a distance of 500 nm, being of the same magnitude as the particle sizes. The irreversible changes in magnetization occur at virtually the same external magnetic field strengths. It can be concluded that the interaction of the particles can be neglected for this distance.
If the magnetic field is applied along the y-direction, i.e., parallel to the hard axis of the larger contact, the magnetization behavior changes in so far as the remanence is reduced in all cases. Comparing the saturating fields (see solid dots in Fig. 5.3), it is obvious that the particles emerge saturation in higher fields

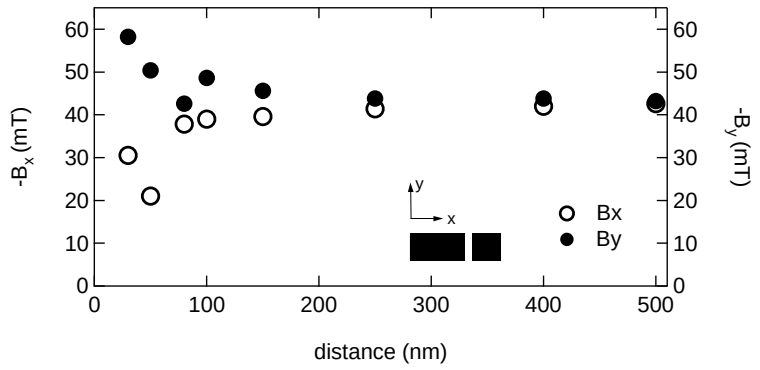

Figure 5.3: External magnetic field needed for saturation in dependence of the particle distance. The data is taken from Fig. 5.2.

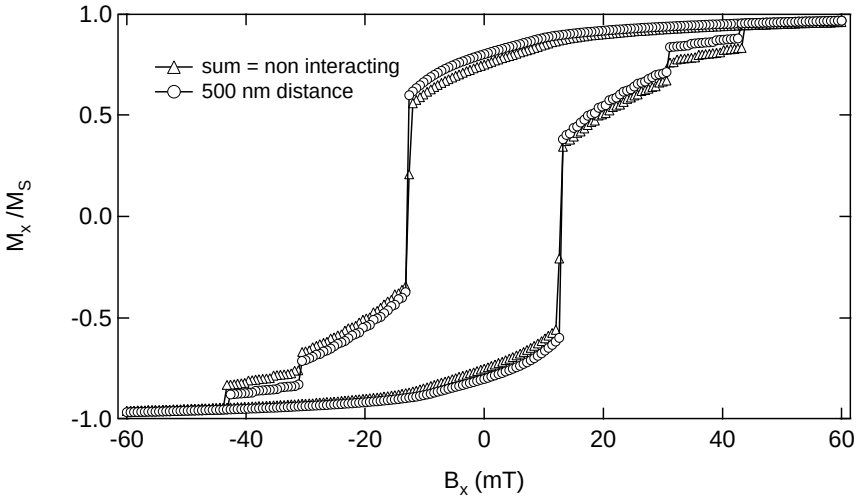

Figure 5.4: The sum of the hysteresis curves of the single contacts in comparison to the interacting particles at a distance of 500 nm. The external field is applied along the easy axis of the rectangular particle.

only, because of shape anisotropy. However, it is remarkable that the saturation field increases with decreasing particle distances, i.e., the interaction increases the saturation field in contrast to the case of magnetization in x-direction. This can be explained by looking at the domain pattern at the channel between the two contacts. As shown in Fig. 4(a) in publication [P1], close to saturation in x direction the magnetization of the particles is aligned slightly antiparallel at the channel. This configuration is conserved throughout the hysteresis curve (see Figs. 4(b)-(d)). In contrast, when applying a magnetic field in y-direction, the particles are magnetized parallel at the channel. This configuration also remains throughout the hysteresis curve and is more stable with respect to the external field than the antiparallel configuration, i.e., a higher magnetic field has to be applied for saturation.

5.3 Stray fields of iron contacts

In the proceeding section, simulated magnetization patterns have been compared to experimental ones measured by magnetic-force microscopy. Further, the magnetization behavior has been analyzed by simulated hysteresis curves. It is desirable to compare the theoretical results to experiments. This is done in the following publication [P2], which deals with the comparison of hysteresis curves achieved with help of micromagnetic simulations and Hall μ-magnetometry. These investigations are performed on iron contacts, which can in principle be used in spintronic devices.

JOURNAL OF APPLIED PHYSICS VOLUME 92, NUMBER 12 15 DECEMBER 2002

Hall micromagnetometry on iron electrodes suitable for spin-polarized transport

G. Meier,[a] R. Eiselt, and M. Halverscheid
Institut für Angewandte Physik and Zentrum für Mikrostrukturforschung, Universität Hamburg, Jungiusstrasse 11, D-20355 Hamburg, Germany

(Received 19 April 2002; accepted 17 September 2002)

Iron electrodes suitable as injectors and detectors for spin-polarized transport in ferromagnet/semiconductor hybrid devices are investigated by Hall micromagnetometry. The Hall effect generated by the stray field of the iron structures is measured for single electrodes and electrode pairs with the external magnetic field aligned in plane either parallel or perpendicular to their easy axes. The strength of the stray field of the double structure in the sensor area is comparable for both configurations. © *2002 American Institute of Physics.* [DOI: 10.1063/1.1519939]

I. INTRODUCTION

Spin injection at room temperature is a key issue for spintronic devices based on semiconductors.[1,2] In this regard iron as a spin injector has attracted a lot of interest theoretically as well as experimentally. From the theoretical point of view it is interesting because of its band structure and concomitant distinct group velocities for spin-up and spin-down subbands at the Fermi energy[3,4] and because of the symmetries of the Bloch part of the wave functions.[5] Experimentally it has been shown recently by optical means that an iron layer can inject a spin-polarized current into a GaAs quantum well through a Schottky barrier with a spin-injection efficiency of about 2%.[6] This proof of principle strengthens the case that iron is a good candidate as an electrode material in room temperature spintronics. In-plane magnetization has been proposed for real spintronic device applications where the magnetic hysteresis behavior can be utilized to sustain spin injection without any external magnetic field.[6] In a spin-transistor device like that proposed by Datta and Das[7] two limiting magnetization geometries are possible, and they have been introduced as spin-valve geometry and spin-transistor geometry.[4] In the former the magnetizations of the electrodes are aligned parallel to each other, whereas in the latter case they are collinear.

In this work we present results of Hall micromagnetometry on individual micrometer-sized iron electrodes with in-plane magnetizations suitable for spin-polarized transport. Structures of similar geometry made of permalloy ($Ni_{80}Fe_{20}$) have been investigated previously by magnetic-force microscopy (MFM) at remanence as well as by micromagnetic simulations in externally applied magnetic fields.[8,9] Electrodes of this geometry have also been used for transport measurements in ferromagnet/InAs hybrid transistors.[10] In these experiments the field effect was examined as a function of the gate voltage in external magnetic fields whereby the observed resistance has indicated spin-polarized transport via an oscillatory gate–voltage dependence of resistance jumps when the magnetization of the ferromagnetic electrodes reverses. However, spin-polarized transport in ballistic hybrid devices based on common ferromagnets to date has resulted in rather subtle effects in the range of percent and is difficult to determine. This is mainly due to the small degree of spin injection as well as to competing effects.[10] Amongst them are weak localization/antilocalization, anisotropic magnetoresistance, and fringe or stray field Hall effects. In this work we focus on the stray fields of microstructured ferromagnets utilized in ferromagnet/semiconductor hybrid devices. In particular, we address their magnitude, their dependence on the strength of an in-plane external magnetic field applied either parallel or perpendicular to the easy axis of the large electrode, as well as the magnetostatic interaction between the electrodes.

II. PREPARATION

The micrometer-sized Hall magnetometers are prepared from modulation doped GaAs/AlGaAs heterostructures with a two-dimensional electron system (2DES) 90 nm below the surface. Hall crosses of geometrical width $w = 1.15\ \mu$m are patterned as mesas by electron-beam lithography and chemical etching (depth 100 nm) with a standard etch solution ($1H_2SO_4:8H_2O_2:200H_2O$). Optical lithography and electron-beam evaporation are used for the wiring and bond pads. Each sample consists of four sensor areas which incorporate the micro-Hall crosses. In a subsequent step the ferromagnetic structures are defined on top of the Hall crosses by electron-beam lithography employing alignment marks defined in a previous step. Iron thin films with a thickness of 27 nm were deposited by thermal evaporation. Figure 1(a) shows an atomic force microscope (AFM) image of an iron double structure located on top of a Hall cross. In the preparation process the exposure of the corners of the structures are corrected for proximity effects in electron-beam lithography in order to optimize their shapes. The AFM measurements revealed that the rectangular shape of the mask was completely transferred to the material.

[a]Electronic mail: meier@physnet.uni-hamburg.de

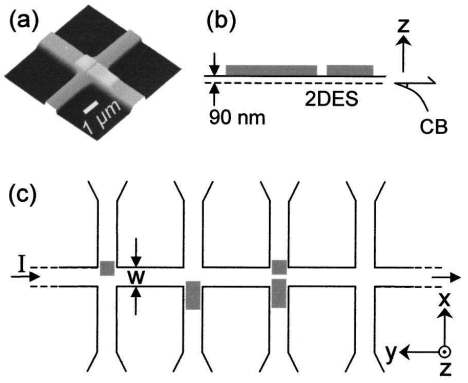

FIG. 1. (a) Atomic force microscope image of a micro-Hall cross ($w = 1.15\ \mu$m) with a pair of iron electrodes on top. (b) Sketch of the cross section. The 2DES is located 90 nm below the surface. (c) Top view of the complete device with a quadratic ($1\ \mu$m$\times 1\ \mu$m), a rectangular ($1\ \mu$m $\times 2\ \mu$m), and a double structure ($1\ \mu$m$\times 2\ \mu$m and $1\ \mu$m$\times 1\ \mu$m). The fourth Hall cross is empty and serves as a reference.

III. EXPERIMENTAL TECHNIQUE AND CALIBRATION

For the measurements an ac current of typically 0.5 μA amplitude and 37.8 Hz frequency is driven through the sensor. The Hall voltages of the crosses are measured simultaneously. A sensor chip is mounted on a chip carrier, which is positioned on a rotatable stage in a probe stick suitable for measurements in the temperature range of 1.6–300 K. The rotatable stage enables characterization of the 2DES with a superconducting magnet in fields of up to 9 T along the z direction directly prior to stray field measurements of the iron structures with the magnetic field in the x or y direction (see Fig. 1). The x and y directions correspond to the spin-transistor and spin-valve geometry, respectively.[4] From carrier concentration of $n_s = 5\times 10^{11}$ cm^{-2} and mobility of $\mu = 700.000$ cm^2 V^{-1} s^{-1} the sensor sensitivity, i.e., the ratio of the Hall voltage to the average stray field $V_H/\langle B_H\rangle$ can in principle be calculated.[11] On the other hand, the most reliable and easiest way to calibrate the sensor is to use the well-known field of the superconducting magnet aligned in the z direction to measure sensor response. It is important to note that this type of calibration procedure is only valid if the Hall sensor is operated in the ballistic regime, i.e., the mean free path l_e of the electrons must exceed the size of the Hall cross.[11,12] In the diffusive regime interpretation of the Hall signal is more complex.[13] In the present samples the ballistic condition is easily satisfied since $l_e = 8.2\ \mu$m.

It is well known that both longitudinal and transverse resistance in a ballistic narrow channel in a 2DES show a nonlinear dependence on weak perpendicular magnetic fields.[14] In our micro-Hall sensors these effects could be observed at low temperatures. In Fig. 2 the longitudinal and the transverse voltage measured at $T = 2$ K exhibit features that have been called the "last Hall plateau" and "camel back."[14] From the data in Fig. 2 we calculate an electronic width of the sensor of $w_e = 0.85\ \mu$m, i.e., the depletion width of our mesas is approximately 150 nm.

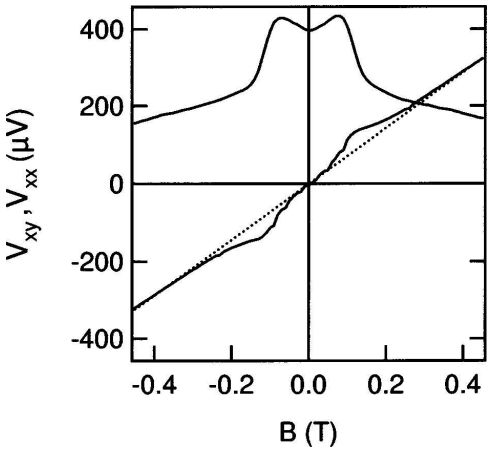

FIG. 2. Transverse and longitudinal voltage measured for a micro-Hall cross at temperature of $T = 2$ K with bias current of $I = 0.5\ \mu$A. Mesoscopic effects known as the last Hall plateau and camel back are clearly observed. The dotted line is a guide to the eye and is the linear sensor response in the absence of mesoscopic effects. From these data an electronic width $w_e = 0.85\ \mu$m is estimated.

IV. RESULTS AND DISCUSSION

We have simultaneously measured three micro-Hall sensors containing a single small ($1\ \mu$m$\times 1\ \mu$m), a single large ($1\ \mu$m$\times 2\ \mu$m), and a double structure ($1\ \mu$m$\times 1\ \mu$m and $1\ \mu$m$\times 2\ \mu$m with a spacing of 150 nm). An empty sensor serves as a reference. This setup ensures that the bias current, temperature, and external magnetic field are identical for all the sensors as well as for the reference.

Figures 3(a)–3(c) show MFM images of the iron electrodes on top of the micro-Hall sensors measured in zero external magnetic field at room temperature in the as-prepared state. The magnetization patterns of the small structures are close to Landau patterns.[15] While in the double structure this is easily seen, the single small structure exhibits a more complex pattern with an additional small closure

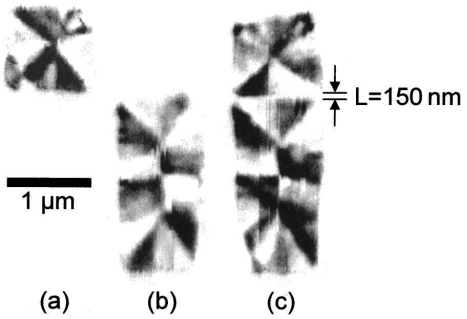

FIG. 3. (a) Magnetic-force microscope images of the iron structures on top of the sensors measured at room temperature. (a) Single small electrode, (b) single large electrode, and (c) electrode pair. The thickness of the structures is 27 nm. The magnetization configuration of the electrode pair right at gap of width $L = 150$ nm is antiparallel.

7298 J. Appl. Phys., Vol. 92, No. 12, 15 December 2002 Meier, Eiselt, and Halverscheid

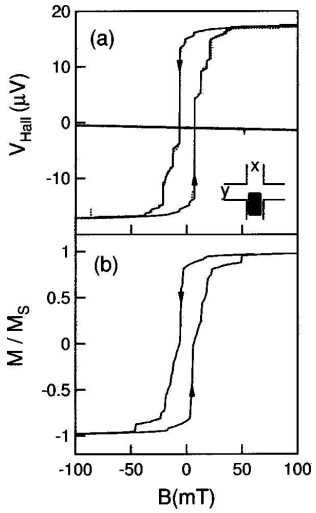

FIG. 4. (a) Hall voltage of the sensor with the single large electrode and the empty reference cross (flat line) at $T=36.5$ K. Shown are two successive sweeps that exhibit nearly no deviations (solid and dotted lines). (b) Simulated hysteresis curve of the integral magnetization for a rectangular ($1\ \mu m \times 2\ \mu m$) iron structure with a thickness of 20 nm.

domain in its lower left corner. In polycrystalline ferromagnetic thin film elements with low overall anisotropy symmetric Néel walls and cross-tie walls are expected for a thickness of 27 nm.[15,16] The large structures in the single as well as in the double structure in Figs. 3(b) and 3(c) exhibit essentially the same magnetization state with closure domains consisting of 90° Néel walls at each end and one cross-tie wall in the middle. The latter can be identified by the chirality of the pattern measured and is not a curl in the magnetization as is often observed in permalloy structures of the same geometry.[17] With respect to transport experiments that use such electrodes as injectors and detectors, the magnetization in the vicinity of the small spacing of the double structure is particularly important. In the MFM image of the double structure antiparallel alignment of the domains next to the spacing is observed in Fig. 3(c), which would correspond to the spin-valve geometry. This behavior is also known from experiment as well as from micromagnetic simulations for permalloy electrodes of the same geometry.[8,9] These calculations also predict that a parallel and an antiparallel magnetization configuration in these domains can be adjusted at will.

Prior to magnetometer measurements the 2DES was characterized by Shubnikov–de Haas oscillations and quantum Hall effect in external magnetic fields aligned perpendicular to the 2DES as previously mentioned. For the stray field measurements that we are pursuing, the sample is within the same cooling cycle, rotated so that the magnetic field becomes aligned in the plane of the 2DES in either the x or y direction. In Fig. 4(a) the transverse voltages of two sensors are shown as a function of the external magnetic field applied along the x direction in two subsequent sweeps (shown by solid and dotted lines).[18] The flat line is the result of the empty reference where the second sweep perfectly reproduces the first. This curve proves that the 2DES itself is not sensitive to magnetic fields applied in plane. It can be used to optimize adjustment of the sensor in the external field. Small constant deviations of the transverse voltage from zero could be caused by structural irregularities on a mesoscopic scale. The voltage measured for the single large electrode in Fig. 4(a) closely resembles a classical hysteresis curve of the integral magnetization. Moving from positive to negative saturation, the transverse voltage displays a reversible change in magnetization followed by two tiny irreversible steps at 6.4 and -1.6 mT, three huge irreversible magnetization jumps at -6.2, -12.2, and -21.2 mT, and again some tiny steps. The way back to positive saturation closely matches the downward sweep, yielding highly reproducible symmetric hysteresis. A simulated hysteresis curve calculated with a computer code supplied by Porter and Donahue[19] displays the normalized magnetization versus the external magnetic field and is shown in Fig. 4(b). Good overall correspondence between both curves is observed, i.e., the squarenesses of the loops and the values of the coercive fields agree well. Still, deviations between experiment and simulation in details of irreversible magnetization switching are evident. Details of the simulation are discussed below.

The temperature dependence of the hysteresis curves measured is rather small. In the regime between 2 and 50 K the amplitude of the Hall signal is constant. Changes of the switching fields between subsequent sweeps are generally small. They tend to be more prominent at the lowest temperatures. Even at 36.5 K almost perfect agreement between two successive sweeps is observed [see Fig. 4(a)]. Above 50 K the signal strength, i.e., the amplitude of the Hall voltage, decreases slowly with an increase in temperature. This can be understood in terms of an increase in carrier concentration n_s in the 2DES which yields a reduced Hall voltage since $V_H \propto 1/n_s$.

An interesting feature was observed when passing through the hysteresis sweep multiple times. While in the first few runs the changes between subsequent sweeps were prominent, the deviations diminished in further sweeps. This training effect was observed in all structures at low temperatures. We attribute this to the special magnetization pattern in the as-prepared state. Although a rather strong magnetic field of 200 mT is applied some field sweeps are required to place the magnetization under the influence of the external field to reach an energetically favorable state. With respect to the application of ferromagnetic structures in spintronics this observation is important because a defined reproducible magnetization state is required.

As mentioned above the sensors are operated in the ballistic regime, i.e., the voltage measured can easily be converted into the average stray field in the sensor area using the calibration in homogeneous perpendicular external magnetic fields. From this procedure the average stray field $\langle B_H \rangle$ generated by the single small structure is obtained. A maximum value of 10.7 mT is observed at saturation, which becomes understandable from a simple model of magnetic charges located right in the sensor area. Accordingly, the stray field measured in the opposite saturation state is equal but re-

versed in sign. By driving the magnetic field up to values of 9 T we examined the possible pinning of domain walls, which could possibly prevent a fully saturated state. However, we observe no difference in the hysteresis curve after the application of such strong fields and conclude that the magnetization state at ± 100 mT is indeed closest to saturation.

This finding is supported by micromagnetic simulations of the hysteresis curve and the corresponding magnetization patterns for the single large electrode. For each external magnetic field a local energy minimum is sought and the corresponding magnetization is calculated. The thermal evaporation process yields polycrystalline iron films and therefore we use a random distribution of the anisotropy direction in the simulation. Different radii of the corners are tested whereby the best agreement is in fact obtained for a rectangular structure. For calculation of the remanent state a grid size of 5 nm is used. The magnetization pattern obtained is in good agreement with the magnetization state observed with the MFM [see Fig. 3(b)]. The resulting magnetization pattern is used as the starting point for computation of the hysteresis curve, which is performed with a grid size of 10 nm. This is a compromise between the actual exchange length $l_{\mathrm{ex}} = \sqrt{A/K_d} = 3.4$ nm of iron,[15,19] where A is the exchange constant and $K_d = \mu_0 M_s^2/2$ the stray field energy constant, on the one hand, and a reasonable computing time on the other. The hysteresis simulated this way is shown in Fig. 4(b). It is in good overall correspondence with the measured curve. The Hall voltage in Fig. 4(a) and the calculated hysteresis curve show a number of irreversible magnetization changes that occur approximately at the same values of the external magnetic field. The deviation of the magnitudes of the jumps between the simulated and experimental curves is expected since the measured transverse voltage is not directly comparable to the normalized integrated magnetization M/M_s plotted in the hysteresis curve.

In the following we discuss the results of the measurements in terms of magnetic stray fields, but the original transverse voltage can easily be recovered via a conversion factor of 0.66 μV/mT (see Fig. 2). With respect to the application of such iron structures in spin-polarized transport it is interesting to compare the behavior of isolated single structures with interacting double ones. The question is whether the interaction completely changes the micromagnetic behavior of the individual structures or if the interaction is small enough to be regarded as a minor correction. Furthermore it is interesting to investigate the difference in magnetic behavior between the two magnetic field configurations when the field is applied in the x and the y directions, respectively. In the y direction a parallel and an antiparallel state should be achievable which corresponds to spin-valve geometry.[4] With the field applied in the x direction a magnetization state close to spin-transistor geometry[4] should be obtainable. To answer these questions we have investigated the structures shown in Fig. 1(c) by recording four transverse voltages simultaneously. Typical data are depicted in Figs. 5(a)–5(c) for the single small, the single large, and the double structure. The solid (and dotted) lines denote measurements for the magnetic field in the x and the y direction, respectively.

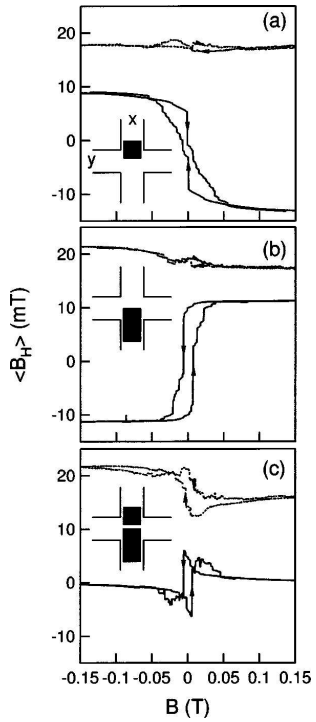

FIG. 5. Measured Hall curves for the (a) small, (b) large, and (c) double structures. Measurements with the external magnetic field aligned in the x direction (solid line) and in the y direction (dotted line) are shown. The latter are offset by $+20$ mT for clarity.

We start with the spin-transistor geometry, i.e., the magnetic field aligned in the x direction (solid lines). As can be seen in Fig. 5(a) the sign of the average stray field for the single small structure deviates from the loop of the single large electrode in Fig. 5(b). This is caused by the mirrored position of the structure on the sensor with respect to the current. This indicates again that the measured stray field curves are not directly comparable to conventional hysteresis curves. Also, details of the micromagnetic behavior in the two electrodes deviate, implying that the shape anisotropy governs the overall micromagnetic behavior. Obviously, other anisotropy contributions play a minor role, presumably because they are averaged out by the polycrystalline composition of the iron. As a matter of fact, in the easy direction with the magnetic field parallel to the x direction the saturated state of the large structure is more readily reached than that of the smaller one. Notice, however, the main irreversible change in magnetization is observed at smaller magnetic field values for the small structure. The stray field strengths of the two single structures are comparable in this field geometry. This is obvious because the magnetic charges at the edge of the electrodes in the sensor areas, i.e., the magnetic

line charge density times the width of the structure, are nearly the same at saturation.

Results for the double structure are shown in Fig. 5(c). Here the stray field curves deviate strongly from conventional hysteresis. This is expected because the simple connection between average stray field in the sensor area and integral magnetization is no longer valid. Interestingly, the stray field is considerably reduced in the double structure, with a maximum value of only 6.3 mT. The main irreversible jumps observed for the single structures can be identified in the measurement for the double structure at approximately the same field values. For example, the first huge jump in the downward sweep of the single large structure at -6.2 mT appears at -5.8 mT in the downward sweep of the double structure. This suggests magnetostatic interaction between the two electrodes which is however a small perturbation for a spacing of 150 nm. This is supported by the magnetization pattern in Fig. 3(c), which closely resembles the pattern of the noninteracting structures in Figs. 3(a) and 3(b). Accordingly, the overall micromagnetic behavior of the single structures can be identified in the loop measured for the double structure. This is consistent with micromagnetic simulations based on permalloy structures of comparable geometry.[9] On the other hand, the stray field in the sensor area, which should be kept at a minimum in spin-polarized transport, is considerably reduced. This is caused by interaction of the two ferromagnetic contacts being in close proximity which tends to reduce the demagnetization energy, i.e., the stray field.

The consistency of our interpretation becomes even more evident when the sum of the curves for the single structures is compared to the directly measured trace of the interacting electrodes. This can be seen in Figs. 6(a) and 6(b). The shape of the total curve for the noninteracting structures exhibits the same features as the directly measured curve for the interacting electrodes. Remarkably, it is possible to identify the irreversible jumps and their switching fields which are only slightly reduced for the interacting structures. As an example, we concentrate on the jumps indicated by arrows that are marked in both curves. Altogether, the interaction seems to reduce the coercivity.

In the following we proceed to the experiments in spin-valve geometry, i.e., the magnetic field is aligned in the y direction. The corresponding traces are shown by dotted lines in Fig. 5(a)–5(c). The stray fields measured for the single structures are small in comparison to the ones in spin-valve geometry discussed before. Their amplitudes are in the range of 1 mT for both structures. In the model of magnetic charges they now reside on the edges which do not lie in the sensitive area of the sensor, i.e., the stray field is expected to be strongly reduced. For spintronic devices based on ferromagnet/semiconductor hybrids this means that electron transport through the channel is hardly affected by stray fields in spin-valve geometry. The shape of these curves is not as regular as in spin-transistor geometry. When repeating the magnetic field sweep the coarse shape of the curve remains the same but the deviations are more pronounced in comparison to in spin-transistor geometry. The result for the double structure depicted in Fig. 5(c) cannot be associated straightforwardly with the sum of the single structures.

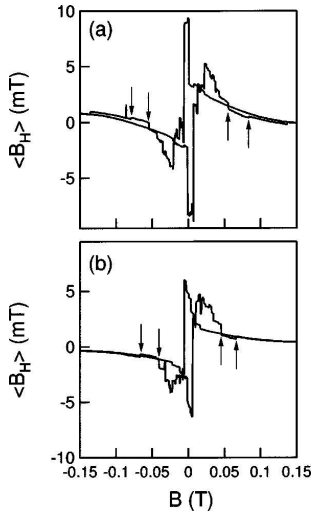

FIG. 6. Comparison of (a) the sum of the Hall signals for the single small and the single large structures with (b) the Hall signal measured for the double structure. The arrows indicate examples of irreversible magnetization changes which can be found in (a) and (b). The external magnetic field is applied parallel to the x direction.

An important consequence for the application of such structures in spin-polarized transport is that the stray field strength produced by ferromagnetic electrodes is comparable for both geometries. One might expect at first glance that the stray field is strongly enhanced if the external magnetic field is applied along the x direction in comparison to along the y direction. The experimental result, however, is that the stray field strength in both configurations is virtually equal for ferromagnetic electrodes in close proximity. In principle, this can be understood as a reduction of demagnetization energy of the two adjacent electrodes.

V. CONCLUSIONS

By means of Hall micromagnetometry we have studied thin individual and interacting iron structures in the μm-size range. Such structures are suitable as electrodes for spin-polarized transport experiments in ferromagnet/semiconductor hybrid devices. The interaction between the closely coupled electrodes is small because the hysteretic behavior of the single structures can be retrieved in the hysteresis curve of the double structure. The measured stray field of the double iron structure is considerably reduced in comparison to that of the single structures and it is found to be of the same size independent of the alignment of the external in-plane magnetic field.

ACKNOWLEDGMENTS

The authors would like to thank U. Merkt for valuable discussions and encouragement, D. Grundler for his support in Hall micromagnetometry, and Ch. Heyn for the MBE

samples. They thank S. McVitie for discussion about the interpretation of MFM images. The expertise and technical assistance of J. Gancarz is appreciated. The authors acknowledge financial support by the Deutsche Forschungsgemeinschaft through the Sonderforschungsbereich 508 ''Quantenmaterialien'' and by the NEDO international joint research grant program.

[1] G. A. Prinz, Phys. Today **48**, 58 (1995).
[2] S. A. Wolf, D. D. Awschalom, R. A. Buhrman, J. M. Daughton, S. von Molnár, M. L. Roukes, A. Y. Chtchelkanova, and D. M. Treger, Science **294**, 1488 (2001).
[3] D. Grundler, Phys. Rev. B **63**, 161307 (2001).
[4] T. Matsuyama, C.-M. Hu, D. Grundler, G. Meier, and U. Merkt, Phys. Rev. B **65**, 155322 (2002).
[5] O. Wunnicke, Ph. Mavropoulos, R. Zeller, P. H. Dederichs, and D. Grundler, Phys. Rev. B **65**, 241306 (2002).
[6] H. J. Zhu, M. Ramsteiner, H. Kostial, M. Wassermeier, H.-P. Schönherr, and K. H. Ploog, Phys. Rev. Lett. **87**, 0166011 (2001).
[7] S. Datta and B. Das, Appl. Phys. Lett. **56**, 665 (1990).
[8] G. Meier and T. Matsuyama, Appl. Phys. Lett. **76**, 1315 (2000).
[9] G. Meier, M. Halverscheid, T. Matsuyama, and U. Merkt, J. Appl. Phys. **89**, 7469 (2001).
[10] G. Meier, T. Matsuyama, and U. Merkt, Phys. Rev. B **65**, 125327 (2002).
[11] A. Geim, S. V. Dubonis, J. G. S. Lok, I. V. Grigorieva, J. C. Maan, L. Theil Hansen, and P. E. Lindelof, Appl. Phys. Lett. **71**, 2378 (1997).
[12] F. M. Peeters and X. Q. Li, Appl. Phys. Lett. **72**, 572 (1998).
[13] I. S. Ibrahim, V. A. Schweigert, and F. M. Peeters, Phys. Rev. B **57**, 15416 (1998).
[14] C. W. J. Beenakker and H. van Houten, Phys. Rev. Lett. **63**, 1857 (1989).
[15] A. Hubert and R. Schäfer, *Magnetic Domains—The Analysis of Magnetic Microstructures* (Springer, Berlin, 1998).
[16] S. Middelhoek, J. Appl. Phys. **34**, 1054 (1963).
[17] S. McVitie, G. S. White, J. Scott, P. Warin, and J. N. Chapman, J. Appl. Phys. **90**, 5220 (2001).
[18] An offset in magnetic field B of -6 mT observed in all measurements is presumably generated by remanence of the superconducting coil and is corrected.
[19] Oommf, object oriented micromagnetic framework, http://math.nist.org/oommf.

As mentioned in the publication [P2], the simulated and measured hysteresis curves can be compared qualitatively, and the positions of irreversible magnetization changes even quantitatively. But no statements could be made concerning the strength of the signal, since a stray field on the one hand is compared to the normalized magnetization on the other.

The solution to this problem is to calculate a signal corresponding to the measurement, based on the data of the micromagnetic simulation. The calculation is described in section 4.2 in chapter 4. The Hall signal consists of an average value of the stray field in the region of the Hall cross. Figure 5.5 shows the resulting signals for the single large (Fig. 5.5(c)) and the single small electrode (Fig. 5.5(d)) in comparison to the experimental results (lower curves in Fig. 5.5(a) and (b)) taken from Fig. 5 in publication [P2]. The strength of the stray field can now be analyzed and is in good agreement for the single large electrode. The simulated signal of the small contact also closely resembles the measured one. However, the

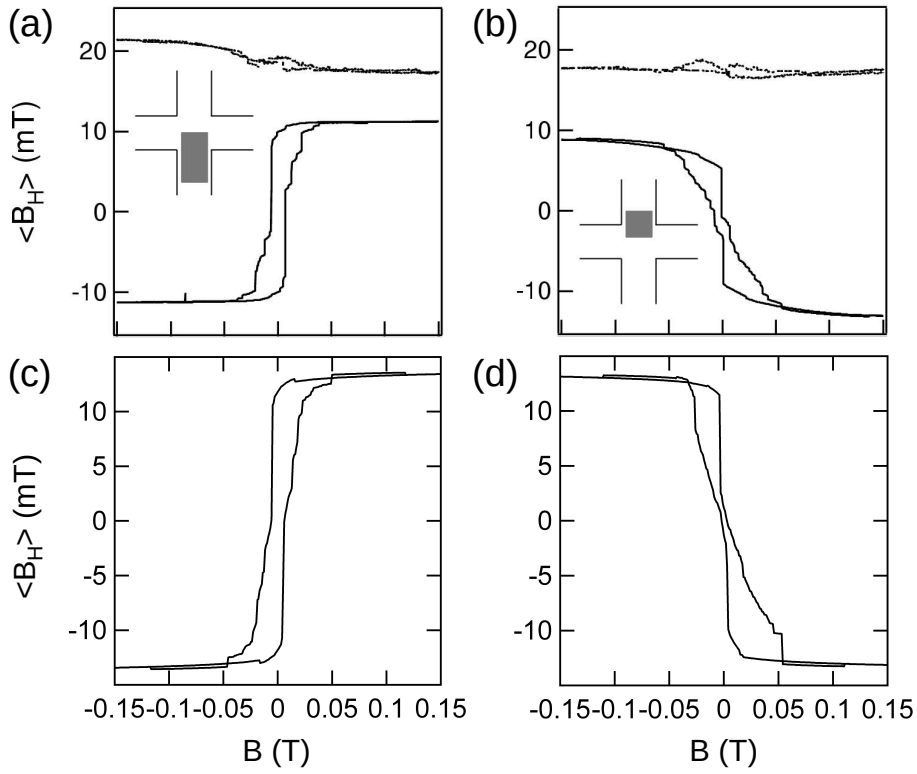

Figure 5.5: Hysteresis curves, showing the averaged stray field of the particle versus the external magnetic field, for (a) a single large iron electrode and (b) a single small contact as measured by Hall μ-magnetometry with the magnetic field aligned in x- and y-direction, corresponding to the solid and dotted line, respectively. These graphs are copied from Publication [P2]. (c) and (d) illustrate the calculated Hall μ-magnetometry signal with the external field in x-direction.

signal strength deduced from the simulated magnetization is slightly stronger. A possible source of error in the calculation is the choice of the electronic width of the Hall cross, which does not correspond to the geometrical width because of a depletion region at the boundaries.

The next publication [P3] deals with the comparison of a measured MFM signal with the simulated magnetization pattern. To do that, the gray scale of the measured image has to be analyzed in terms of magnetization directions. However, the magnetization configuration resulting in a certain stray field pattern is not necessarily unique. This means that micromagnetic simulations help to interpret measured images, if the stray field pattern resulting from the domain configuration is known. Therefore, it is desirable to calculate the measurement signal of magnetic-force microscopy from simulated magnetization data. These calculations are described in chapter 4 and are utilized for further investigations on the pair of iron contacts as presented in publication [P3]. Here, also the stray field in the channel between the electrodes is visualized by the calculations.

JOURNAL OF APPLIED PHYSICS VOLUME 93, NUMBER 10 15 MAY 2003

Stray fields of iron electrodes for spin-polarized transport

M. Barthelmess,[a] A. Thieme, R. Eiselt, and G. Meier
Institut für Angewandte Physik und Zentrum für Mikrostrukturforschung, Universität Hamburg Jungiusstraße 11, D-20355 Hamburg, Germany

(Presented on 15 November 2002)

In semiconductor spintronic devices that incorporate ferromagnetic materials the stray-field configuration in the plane of the two-dimensional electron system is of crucial importance. We investigate the stray fields of iron electrodes suitable as injector and detector for spin-polarized transport in hybrid semiconductor/ferromagnet devices. Magnetic-force microscopy images of an electrode pair are derived from simulated magnetization patterns. The calculated averaged stray field is compared to the experimental signal of a ballistic Hall micromagnetometer comprising a two-dimensional electron system in a GaAs/AlGaAs-heterostructure 90 nm below the electrodes. Good agreement between simulation and experiment is obtained. © *2003 American Institute of Physics*. [DOI: 10.1063/1.1543131]

I. INTRODUCTION

Spintronics with semiconductors and ferromagnets is a vivid and intensively investigated research field.[1,2] Electrical spin injection has been demonstrated successfully for ferromagnet/semiconductor hybrid systems utilizing the degree of circular polarization of light emitted from the semiconductor.[3–5] All-electrical detection of spin-polarized transport has been observed, e.g., by Hu *et al.*[6] Recently, we could measure a gate-voltage-dependent magnetoresistance in InAs/permalloy hybrid transistors.[7] However, the amplitudes in these transport experiments are rather small and difficult to interpret since parasitic effects in the semiconductor could mimic spin-dependent transport. To exclude them and to corroborate the interpretation of the magnetoresistance as spin effect detailed investigations of the stray fields are imperative. Here we compare experimental results obtained from magnetic-force microscopy (MFM) and Hall micromagnetometry with stray fields inferred from micromagnetic simulations of the domain structure of the electrodes. We take advantage of the fact that Hall micromagnetometry seizes the averaged stray field in the channel of a ballistic two-dimensional electron system (2DES).[8–11]

II. MICROMAGNETIC SIMULATIONS

The iron electrodes have a thickness of 20 nm and a size of $2\ \mu\text{m}\times 1\ \mu\text{m}$ and $1\ \mu\text{m}\times 1\ \mu\text{m}$, respectively. They are separated by a 150 nm wide spacing (see Fig. 1). The asymmetric geometry results in distinct micromagnetic behaviors. In particular, it provides different switching fields in externally applied magnetic fields. The magnetization pattern of the electrodes is simulated with a computer code supplied by Porter and Donahue.[12] For iron, a saturation magnetization of 1 700 000 A/m, an exchange constant of 21×10^{-12} J/m, and an anisotropy constant of 48 000 J/m^3 are chosen. A grid size of 5 nm close to the exchange length of iron is employed to calculate the as-prepared $B=0$ state. In order to obtain a reasonable computing time, the hysteresis loop itself is calculated with a grid size of 10 nm using the as-prepared state as starting magnetization configuration. The external magnetic-field B is applied parallel to the easy axis of the larger structure (x direction, see Fig. 1) and is increased in steps of 1 mT up to +200 mT, then decreased to −200 mT. The loop is completed by increasing the field again to +200 mT.

To be able to compare the simulation to the Hall-micromagnetometer measurements,[8,11] the stray fields of the iron electrodes are determined from the array of magnetic dipoles resulting from the micromagnetic calculation. The strength of each dipole is given by the volume of the lattice cell $10\times 10\times 20\ \text{nm}^3$ times the saturation magnetization. With this model the z component of the stray field, that is effective for a 2DES, can easily be calculated for various distances. The second derivative of the z component of the stray field with respect to the z direction corresponds to the signal measured with magnetic-force microscopy.[13]

III. COMPARISON TO EXPERIMENTAL RESULTS

Figure 1(a) shows the magnetization of both electrodes calculated for $B=0$. The sketch in Fig. 1(b) illustrates the domains. The quadratic electrode exhibits a Landau pattern, the larger electrode two vortices separated by a cross-tie wall. The vortices consist of 90° and 180° Neél walls, while the cross-tie wall is a combination of a 180° Neél wall and a 180° Bloch wall, such that the magnetization is oriented out-of-plane at the center of the cross-tie wall. Figure 1(c) represents the z component of the second derivative of the stray field calculated in a vertical distance of 70 nm, which is a typical MFM lift-scan height. Here, the cross-tie wall can be clearly observed and should not be misinterpreted as a magnetization curl which is often observed in permalloy structures of the same geometry.[11,14,15] Most interesting is the region in the gap between the electrodes since in a spin-transistor device this is the semiconductor channel. At $B=0$, the magnetizations at the channel are aligned antiparal-

[a]Electronic mail: mbarthel@physnet.uni-hamburg.de

J. Appl. Phys., Vol. 93, No. 10, Parts 2 & 3, 15 May 2003 Barthelmess *et al.* 8401

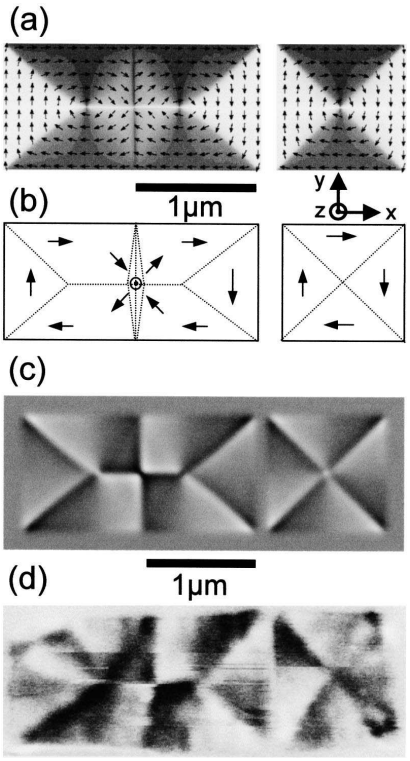

FIG. 1. (a) Calculated magnetization pattern of two 20-nm-thick iron electrodes separated by a 150-nm-wide gap at $B=0$. (b) Sketch of the domains illustrating the formation of the cross-tie wall in the larger electrode. (c) Second derivative of the stray field calculated at a vertical distance of 70 nm. (d) MFM image of the electrode structure prepared by electron-beam lithography. Note that the upper scale is valid for (a) and (b) and the lower for (c) and (d).

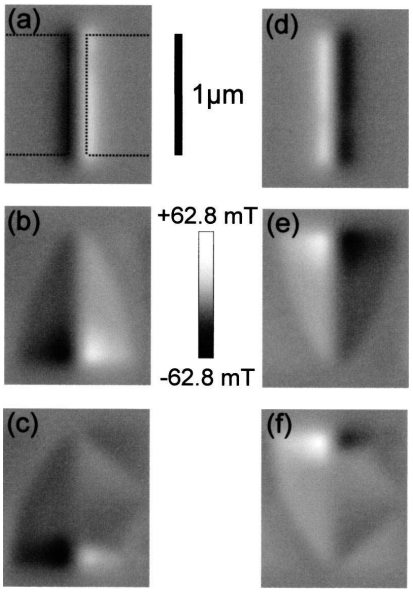

FIG. 2. Stray field strengths in a 1150 nm×1400 nm section of the structure in Fig. 1 calculated for six external magnetic fields. The large and small electrodes lie on the left- and right-hand side, respectively. Downsweep: (a) +200 mT which is next to positive saturation, (b) 0 mT, and (c) −5 mT after the first irreversible magnetization change. Upsweep: (d) −200 mT, (e) 0 mT, and (f) +5 mT. The maximum and minimum local stray-field strengths are +62.8 mT and −62.8 mT, respectively.

lel as can be seen in Fig. 1(c). This results in an overall stray field smaller than in the parallel configuration.

Polycrystalline iron electrodes of the geometry discussed above are prepared by electron-beam lithography, thermal evaporation, and a lift-off process. Their MFM image in Fig. 1(d) agrees well with the simulated one, see, e.g., the chessboardlike structure at the cross-tie wall in Figs. 1(c) and 1(d). The antiparallel magnetization next to the spacing causes the reversed gray scale along the channel in the large and small electrode observed in the simulated as well as in the measured MFM image.

In the following we analyze the region between the ferromagnetic contacts in more detail. Figure 2 shows a 1150 nm×1400 nm section of the local stray-field distribution at different external magnetic-field strengths, calculated for a distance of 90 nm below the ferromagnetic electrodes. The contour of the contacts is indicated in Fig. 2(a) which shows the saturated state at +200 mT. Figure 2(b) represents the remnant state. In Fig. 2(c), the external magnetic field of −5 mT has caused the magnetization pattern of the smaller electrode to reverse its direction resulting in a parallel alignment of the domains next to the channel. The strongest local stray fields occur at $B=\pm 5$ mT just after this irreversible magnetization change. They have an absolute value of 62.8 mT. Figures 2(d)–2(f) represent the situation at the corresponding points in the upsweep of the loop underlining the symmetry of the hysteresis curve. In the saturated states of Figs. 2(a) and 2(d) the average stray-field penetration into the semiconductor channel is strongest.

Experimentally, the average of the stray field is measured by means of Hall micromagnetometry. The Hall micromagnetometer consists of a modulation-doped GaAs/AlGaAs heterostructure with a 2DES 90 nm below the surface. The Hall crosses are patterned as mesas by electron-beam lithography and chemical etching with a geometrical width of $w=1150$ nm and an electronic width of $w_{el}=850$ nm. Experimental details are reported elsewhere.[11] To compare the simulation with the experimental results the average of the stray field is calculated 90 nm below the surface in a 850 nm×850 nm wide region which corresponds to the active sensor area. This procedure is performed for each value of the applied magnetic field. The resulting ''hysteresis'' curve is shown in Fig. 3(a) and can be compared to the measured one in Fig. 3(b). The overall shapes of the two curves are in good agreement. The stray field maxima occur at approximately the same values of the external field, namely, at −5 and +5 mT in the simulated curve, and at −5.8 and +6.2 mT in the measured one. Although the mea-

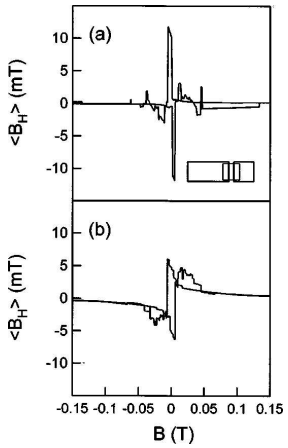

FIG. 3. (a) Calculated averaged stray fields of the 850 nm×850 nm sensor area under the iron electrodes as indicated in the inset vs the externally applied magnetic field in the range between −150 and 150 mT. (b) Hall-sensor signal measured at a temperature of $T=37$ K.

sured and simulated averaged stray-field strengths are both in the few-mT regime the theoretical values are a factor of 2 stronger than measured. This might be due to a different saturation magnetization of the real polycrystalline iron structures or due to the specific sensor area chosen. This area strongly depends on the effective electronic width which results from depletion and can only be determined rather indirectly from mesoscopic transport effects.[11]

IV. CONCLUSIONS

We have investigated stray fields of micrometer-sized iron structures that are suitable as injectors and detectors for spin-polarized transport. Simulations of the magnetization of the as-prepared state show good agreement with MFM images measured at room temperature. For the entire hysteresis curve of the electrode configuration the averaged stray fields in the 2DES channel between the ferromagnetic electrodes are calculated in the region of a Hall micromagnetometer and are compared to the measured sensor response. In summary, the combination of Hall micromagnetometry and micromagnetic simulation provides a powerful tool for the analysis of stray fields in ferromagnet/semiconductor hybrid systems.

ACKNOWLEDGMENTS

The authors would like to thank U. Merkt for encouragement and D. Grundler for valuable discussions about Hall micromagnetometry. We acknowledge financial support of the Deutsche Forschungsgemeinschaft via the Sonderforschungsbereich 508 ''Quantenmaterialien,'' the Graduiertenkolleg ''Physik Nanostrukturierter Festkörper,'' the NEDO International Joint Research Grant Program, and the BMBF (Grant No. 13N8283).

[1] G. A. Prinz, Phys. Today **48**, 58 (1995).
[2] S. A. Wolf, D. D. Awschalom, R. A. Buhrman, J. M. Daughton, S. von Molnár, M. L. Roukes, A. Y. Chtchelkanova, and D. M. Treger, Science **294**, 1488 (2001).
[3] H. J. Zhu, M. Ramsteiner, H. Kostial, M. Wassermeier, H.-P. Schönherr, and K. H. Ploog, Phys. Rev. Lett. **87**, 0166011 (2001).
[4] V. F. Motsnyi, J. De Boeck, J. Das, W. Van Roy, G. Borghs, E. Goovaerts, and V. I. Safarov, Appl. Phys. Lett. **81**, 265 (2002).
[5] A. T. Hanbicki, B. T. Jonker, G. Itskos, G. Kioseoglou, and A. Petrou, Appl. Phys. Lett. **80**, 1240 (2002).
[6] C.-M. Hu, J. Nitta, A. Jensen, J. B. Hansen, and H. Takayanagi, Phys. Rev. B **63**, 125 333 (2001).
[7] G. Meier, T. Matsuyama, and U. Merkt, Phys. Rev. B **65**, 125327 (2002).
[8] F. M. Peeters and X. Q. Li, Appl. Phys. Lett. **72**, 572 (1998).
[9] A. Geim, S. V. Dubonos, J. G. S. Lok, I. V. Grigorieva, J. C. Maan, L. Theil Hansen, and P. E. Lindelof, Appl. Phys. Lett. **71**, 2379 (1997).
[10] T. M. Hengstmann, D. Grundler, N. Klockmann, H. Rolff, Ch. Heyn, and D. Heitmann, IEEE Trans. Magn. **38**, 2535 (2002).
[11] G. Meier, R. Eiselt, and M. Halverscheid, J. Appl. Phys. **92**, 7296 (2002).
[12] *Oommf*, object oriented micromagnetic framework, http://math.nist.gov/oommf
[13] U. Hartmann, Phys. Lett. A **137**, 475 (1989).
[14] S. McVitie, G. S. White, J. Scott, P. Warin, and J. N. Chapman, J. Appl. Phys. **90**, 5220 (2001).
[15] G. Meier and T. Matsuyama, Appl. Phys. Lett. **76**, 1315 (2000).

5.4 Permalloy sample at zero magnetic field

By combining magnetic-force microscopy and simulated images, not only domain formation can be studied, but also the principle of magnetic-force microscopy can be investigated. The next publication [P4] deals with measurements and simulations on permalloy elements of various geometries and thicknesses. The sample is introduced in detail in chapter 3. Here, the method of calculating a MFM signal is improved by taking into account the exact position of the magnetic dipole inside the cantilever, which serves as an approximation of the real magnetic tip [70].

Another aim of the investigations is the study of domain walls in structured material in dependence of the film thickness. As described in chapter 3, nine different film thicknesses have been prepared, partly from vertically assembled permalloy films. For a comparison, the film thickness of 100 nm is prepared with both methods, in a single preparation cycle as well as by sputtering three times on top of each other, using the 10, 20, and 70 nm thick permalloy films. However, the particles prepared from assembled films either do not show a magnetic signal or it is much smaller in strength as shown in Fig. 5.6. From a comparison of the 100 nm thick elements prepared in both methods, it can be concluded, that either the magnetic signal does not result from the entire layer system or the micromagnetic structure is strongly influenced by the layer structure. For this reason, the further investigations presented are performed on the elements prepared in a single sputtering process.

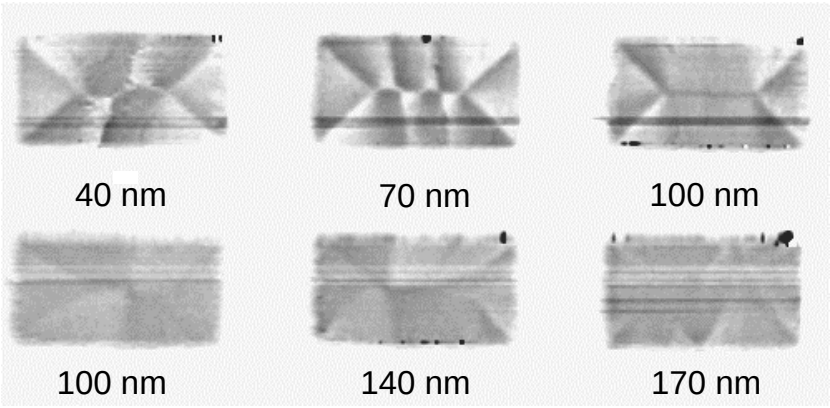

Figure 5.6: Magnetization pattern of the 1 μm×2 μm large permalloy elements as measured by magnetic-force microscopy. The top row consists of particles prepared in one preparation cycle, whereas the elements in the bottom row are prepared from vertically assembled permalloy layers. The black and white spots at the boundaries are artifacts resulting from tear-off edges.

JOURNAL OF APPLIED PHYSICS VOLUME 95, NUMBER 10 15 MAY 2004

Stray fields of domains in permalloy microstructures—Measurements and simulations

M. Barthelmess, C. Pels, A. Thieme, and G. Meier[a)]
Institut für Angewandte Physik und Zentrum für Mikrostrukturforschung, Universität Hamburg Jungiusstraße 11, D-20355 Hamburg, Germany

(Received 16 October 2003; accepted 15 February 2004)

We have measured the stray fields of thin permalloy ($Ni_{83}Fe_{17}$) microstructures with different geometries and several thicknesses by magnetic-force microscopy (MFM). The MFM images are compared to corresponding images calculated from micromagnetic simulations. In particular, the type of 180° domain walls is discussed. We observe a transition from cross-tie to asymmetric Bloch walls between 70 and 100 nm film thickness. Good agreement between measurement and simulation is obtained. © *2004 American Institute of Physics.* [DOI: 10.1063/1.1697642]

I. INTRODUCTION

Interest in the magnetization of micro- and nanostructured ferromagnetic thin films has been boosted by the development of magnetoelectronic devices[1,2] and research on the interplay between transport properties and magnetic domain structure.[3,4] Local modulation of the spin orientation in domain walls causes an additional contribution to the magnetoresistance, which cannot be neglected in the micro- and nano-meter scale of ferromagnets. Therefore, a detailed knowledge of the domain structure is essential. Currently, in the very active field of spin electronics,[5] the micromagnetic properties of ferromagnetic contacts acting as source of spin-polarized electrons play a decisive role,[6,7] e.g., a homogeneous magnetization and small stray fields of the injector are desired for spin-polarized transport. In basic research on magnetic domain structure, there is a current interest in permalloy thin films, especially in the Bloch to Néel transition,[8] the internal structure of domain walls,[9] and the concomitant stray fields.[10] In this article, we present results of a systematic variation of the lateral geometry and thickness of microstructured permalloy thin films relevant for spintronic and magnetoelectronic applications prepared by electron-beam lithography and investigated by means of magnetic-force microscopy and micromagnetic simulations. A great deal of work, theoretical[11,12] as well as experimental,[13–15] has been done on rectangular permalloy elements. A good overview can be found in the book of Hubert and Schäfer.[16] In the present work the specific transition in domain wall structure as a function of sample thickness influenced by the lateral confinement on the micrometer scale is investigated.

II. PREPARATION AND EXPERIMENT

Figure 1(a) shows an overview of the sample prepared by electron-beam lithography and lift-off processing. Permalloy is deposited repeatedly on a GaAs (100) surface by a dc sputter process. Details of the deposition process are described elsewhere.[17,18] The composition of the thin-film alloy $Ni_{83}Fe_{17}$ is analyzed by energy-dispersive x-ray analysis. The completed sample includes microstructures with five different thicknesses deposited in a single process and the repeatedly sputtered microstructures consisting of two, respectively, three layers with another five different thicknesses. With this technique, ten different lateral geometries of homogeneous vertical growth are prepared: $1\times1\ \mu m^2$, $1\times1.5\ \mu m^2$, $1\times2\ \mu m^2$, $1\times4\ \mu m^2$, $1.5\times1.5\ \mu m^2$, $1.5\times2\ \mu m^2$, $1.5\times4\ \mu m^2$, $2\times2\ \mu m^2$, $2\times4\ \mu m^2$, and $4\times4\ \mu m^2$. Figure 1(b) shows a cut out of one row of the geometry $1.5\times4\ \mu m^2$ with different thicknesses of the structures, namely, 10, 20, 40, 70, and 100 nm as determined by atomic-force microscopy [see Fig. 1(c)]. For each geometry, two rows of the same film thicknesses exist, i.e., row one and three, and row two and four are nominally identical. The latter, consisting of the additively sputtered films, comprise additional thicknesses. These structures reveal very complex magnetization patterns presumably caused by the inhomogeneous vertical growth in several deposition steps and are not further discussed in this article. Consequently, for each geometry there exist two microstructures with exactly the same size and thickness. This provides the possibility to compare their micromagnetic behavior and yields a better experimental basis for the comparison with micromagnetic simulations.

The sample is investigated by magnetic-force microscopy (MFM) applying the LiftMode™ (Ref. 19) at a lift-scan height of 40 nm without external magnetic field. Standard thin-film MFM tips sold by Veeco/Digital Instruments, Santa Barbara, CA (type Magnetic Etched Silicon Probe) coated with a ferromagnetic CoCr alloy are applied. The fact that structures of the same lateral geometry but different thicknesses are prepared on a single wafer allows MFM measurements under exactly the same conditions, i.e., temperature, magnetic field, and, most important, the same MFM tip. Scan rates of 0.1 Hz/line and slower are used to obtain high quality MFM images.

III. SIMULATION OF MAGNETIC-FORCE-MICROSCOPY IMAGES

The domain configurations of the permalloy microstructures described above are simulated using a computer code

a)Electronic mail: meier@physnet.uni-hamburg.de

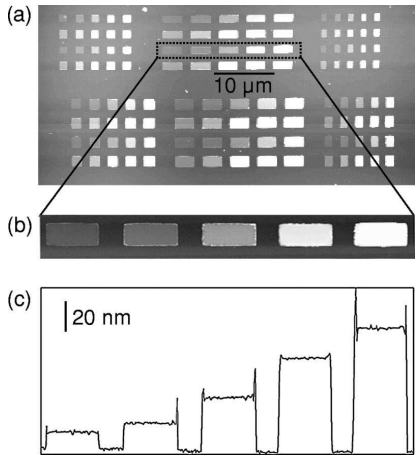

FIG. 1. (a) Topography of a section of the $Ni_{83}Fe_{17}$ sample prepared on GaAs, measured with atomic-force microscopy. The sample comprises geometries in the range of 1×1 μm^2 to 4×4 μm^2 each with five different film thicknesses. (b) Cutout of one row of identical lateral geometry. (c) Line scan of the elements shown in (b), illustrating the increasing film thickness, i.e., 10, 20, 40, 70, and 100 nm.

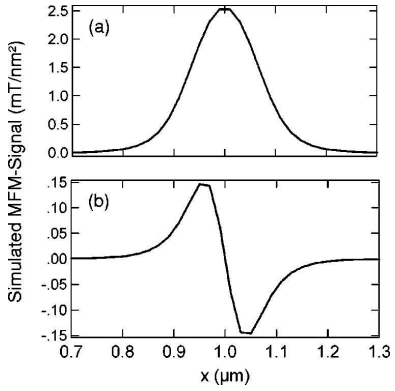

FIG. 2. Calculated MFM signal of (a) an undisturbed Bloch wall in a 100 nm thick film with a wall width of 90 nm and (b) an undisturbed Néel wall in a 35 nm thick film with a wall width of 30 nm.

supplied by Donahue and Porter.[20] For permalloy the following material parameters are chosen: saturation magnetization $M_S=860\times10^3$ A/m, anisotropy constant $K_1=100$ J/m^3, exchange constant $A=13\times10^{-12}$ J/m, and a cell size of 10 nm in each direction using the fully three-dimensional code. The directions of the uniaxial crystal-anisotropy axes are chosen to be distributed randomly to account for the polycrystalline permalloy film with virtually no texture as produced with the present sputter process. For a direct comparison between measurement and simulation, images corresponding to the measured MFM image are calculated from the simulated magnetizations. For this, the data is interpreted as an array of magnetic dipoles whose strengths result from the product of the lattice-cell volume times the saturation magnetization. From these magnetic dipoles the overall stray field is evaluated. The measured MFM signal in the present mode of operation corresponds to the phase shift of the oscillating cantilever, resulting from the interaction between magnetic tip and stray field of the magnetic sample.[21] The phase shift is proportional to the force gradient, which corresponds to the second derivative of the measured stray field.[22–24] This second derivative is calculated from the simulated data and translated into a gray-scale image, which can be compared directly to the measured MFM image. It is now commonly accepted that either the dipole or the monopole contribution can be used to model the MFM tip.[25–27] For the present calculations, the MFM tip is considered a magnetic point dipole.[28] As long as the tip-sample distance, i.e., the lift-scan height, is significantly larger than the cell size of the dipole array, this is a valid approximation. To be able to describe the real thin-film tip within the framework of the point-dipole approximation, the dipole moment must be located at an elevated position within the tip volume. Consequently, for the simulated MFM images, the sum of the experimentally controllable lift-scan height plus an additional distance, accounting for the location of the point dipole representing the physical MFM tip, has to be used.[25] Our MFM image-calculation code is at present a command-line tool, which is compatible to the OOMMF output-file format.[20] One parameter is the distance between point dipole and sample surface mentioned above. The components of the magnetic stray-field vector and the corresponding derivatives can be obtained. While the latter are relevant for simulated MFM images, the field components themselves can be used to evaluate, e.g., the signal of Hall micromagnetometers,[29,30] not discussed here. As an example, the simulated MFM signals of parameterized, i.e., perfect 180° Bloch and Néel walls are calculated. Following the calculations of Ref. 10, we assume a 100 nm thick film with a wall width of 90 nm and a 35 nm thick film with a wall width of 30 nm for the parameterized Bloch and Néel wall, respectively. The wall width is defined as in Ref. 8. The corresponding simulated MFM signals are shown in Fig. 2. The Bloch wall causes a symmetric and the Néel wall an asymmetric MFM signal. In real microstructures, the wall type will generally consist of a mixture of Bloch and Néel contributions.

IV. RESULTS AND DISCUSSION

Free parameters for the calculation of the MFM signal in the point dipole approximation are quality factor and spring constant of the cantilever and strength and position of the point dipole representing the physical MFM tip. However, the first three parameters enter as a common factor simply scaling the strength of the calculated MFM signal. Typical values for these parameters for the present type of MFM tip can be found in Ref. 25. The crucial parameter for the calculation of MFM images is the position δ of the point dipole inside the MFM tip, which enters in a more sophisticated way into the calculation. The parameter δ also depends on the size of the measured micromagnetic structure, i.e., in principal δ has to be determined for each microstructure individually. To determine this quantity, we compare measured

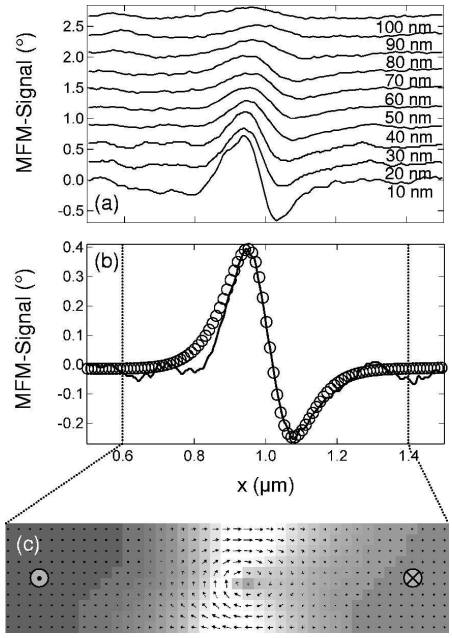

FIG. 3. (a) Measured line scans across a 180° domain wall in a 100 nm thick $2\times4\ \mu m^2$ sized rectangle for various lift-scan heights as indicated. Each linescan is an average over 50 line traces at the same position to improve the signal to noise ratio. The traces are successively shifted upwards for clarity. (b) Line scan measured in a lift-scan height of 40 nm (solid line) compared to the simulated line scan calculated at 90 nm distance (circles). (c) Cut through the simulated magnetization pattern in the range indicated in (b), revealing the structure of the underlying asymmetric Bloch wall.

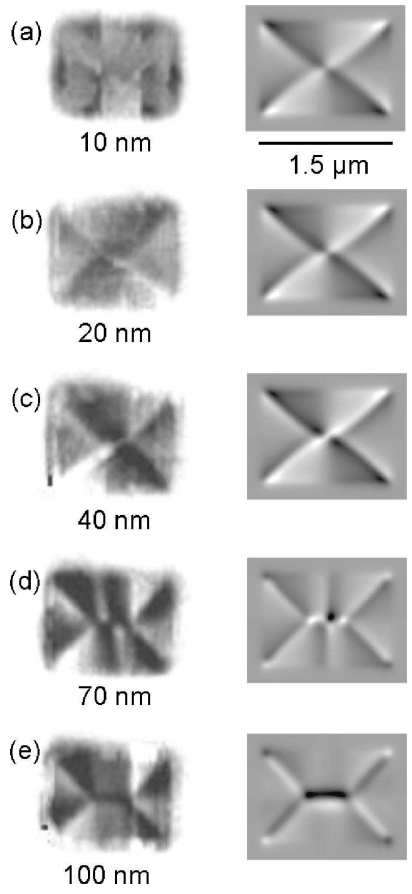

FIG. 4. Magnetization patterns of $1\times1.5\ \mu m^2$ sized permalloy rectangles with five different film thicknesses measured with magnetic-force microscopy with a lift-scan height of 40 nm (left) and micromagnetic simulations calculated at a distance of 90 nm (right).

and simulated line scans across a 180° wall. Figure 3(a) shows line scans across a 180° wall in a 100 nm thick $2\times4\ \mu m^2$ microstructure measured in various lift-scan heights in the range of 10 to 100 nm. Simulated MFM line scans of the 100 nm thick element are calculated in a variety of distances between 10 and 200 nm. By comparing the measured and calculated decrease in amplitude from one line scan to the next, we can deduce the location of the virtual point dipole in the magnetic tip for the investigated microstructure. It results to be 50 nm from the apex of the tip. The calculated line scan with fitted amplitude in comparison to the measured one at a lift-scan height of 40 nm is depicted in Fig. 3(b). The good agreement between measured and simulated MFM signal prooves the applicability of the point dipole approximation and allows a detailed determination of the wall type. The line scans can be interpreted as a superposition of a Bloch and a Néel contribution (compare Fig. 2), the center of the Bloch wall being slightly shifted with respect to the one of the Néel wall. In the micromagnetic simulation, the underlying wall type can be viewed directly (see Fig. 3(c)). It shows a cut through the sample revealing an asymmetric Bloch wall.[31,32] Because of the good agreement between measurement and simulation, it can be concluded that in fact in the 100 nm thick particle an asymmetric Bloch wall is formed.

In Fig. 4, MFM measurements (on the left) are compared to the calculated signal (on the right) of $1\times1.5\ \mu m^2$ sized permalloy rectangles varying in film thickness. In the simulations, different starting patterns for the magnetization were tested. For the 70 nm thick element, an envelope configuration results in the smallest total energy. For the other four structures crosses yield the minimum energy configuration. It is obvious that the measured MFM signal of the 10 nm thin element [see Fig. 4(a)] cannot be analyzed, because the MFM tip manipulates the domain pattern irreversibly during measurement by dragging the domain walls along with it while scanning across the walls. The problem could not be circumvented by using a larger lift-scan height within a reasonable range. This is presumably due to the fact that the dragging of domain walls occurs already in the topography

5644 J. Appl. Phys., Vol. 95, No. 10, 15 May 2004 Barthelmess *et al.*

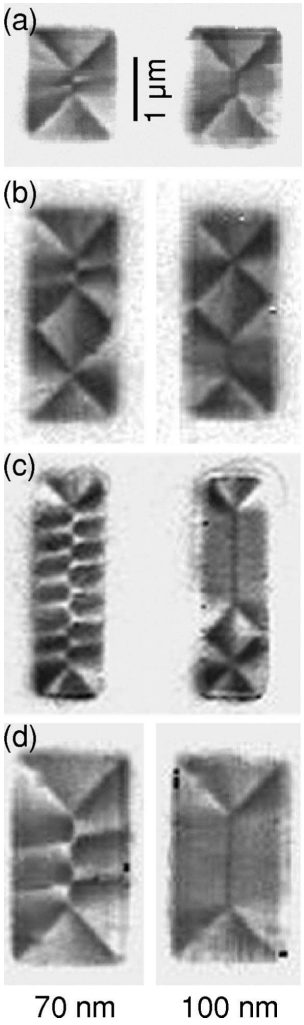

FIG. 5. Magnetic-force micrographs showing the transition from cross-tie walls to noncross-tie walls between 70 nm (on the left) and 100 nm (on the right) thick film elements for different geometries, i.e., (a) $1.5\times2\ \mu m^2$, (b) $1.5\times4\ \mu m^2$, (c) $1\times4\ \mu m^2$, and (d) $2\times4\ \mu m^2$.

scan preceding the MFM scan in close proximity to the structures. For film thicknesses larger than 10 nm, an irreversible manipulation by the MFM tip is not observed.

The simulated domain patterns of the three thinnest microstructures reproduced in Figs. 4(a)–4(c) are very similar and show a crosslike pattern. The sense of rotation of the flux-closure patterns of the 20 and 40 nm thick elements is inverted in direction and energetically degenerated due to the anticipated random distribution of the uniaxial anisotropy. The 70 nm thick element [see Fig. 4(d)] shows a cross-tie wall in the measured as well as in the calculated signal. In contrast, the 100 nm thick rectangle [see Fig. 4(e)] consists of four domains of approximately the same size as in the 70 nm element, but does not comprise a cross-tie wall, again in the simulated as well as the measured signal. The wall in the center of the structure is an asymmetric Bloch wall as discussed in detail above (see Fig. 3). For all thicknesses, measurements and simulations are in good correspondence.

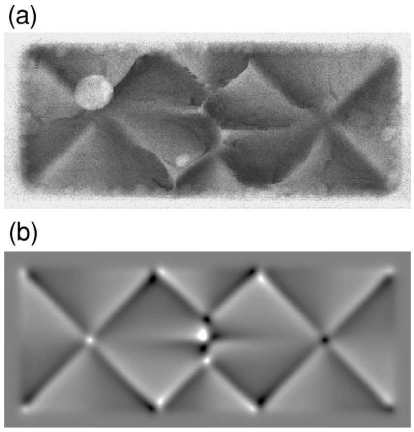

FIG. 6. Comparison of measured and calculated MFM signal of a 70 nm thick element with a size of $1.5\times4\ \mu m^2$.

The transition from cross-tie walls to noncross-tie walls between 70 and 100 nm film thickness is observed in all elements containing 180° walls. This is illustrated in Fig. 5. Here the measured signals of four additional geometries are shown, comparing 70 nm thick microstructures on the left to 100 nm thick ones on the right. The first geometry, $1.5\times2\ \mu m^2$ in Fig. 5(a), exhibits similar magnetization patterns as the ones discussed above [see Figs. 4(d) and 4(e)]. Again, the 70 nm thick element shows four domains with a cross-tie wall as 180° wall, whereas the 100 nm thick structure shows an envelope kind of shape. Although the larger structures in Fig. 5 reveal more complicated domain patterns, the transition between cross-tie and Bloch wall is observed throughout. At the size of $1.5\times4\ \mu m^2$ in Fig. 5(b), both magnetization patterns consist of a cross next to a second pattern, a cross-tie wall in the 70 nm element, and an envelope structure with a Bloch wall in the 100 nm thick rectangle. Regarding the 100 nm thick shape, this domain pattern is again observed in the $1\times4\ \mu m^2$ sized element [Fig. 5(c)]. However, the corresponding 70 nm thick structure consists of several cross-tie walls. The $2\times4\ \mu m^2$ geometry depicted in Fig. 5(d) shows two cross-tie walls in the 70 nm thick element and again an envelope pattern in the thicker structure. For the $1.5\times4\ \mu m^2$ geometry, an alternative magnetization pattern comprising a cross-tie wall is found for 70 nm film thickness in MFM measurements as well as in simulation, as presented in Fig. 6. Here the cross-tie wall lies between two crosses and is rotated by an angle of 90° compared to the MFM image shown in Fig. 5(b).

The transition of wall type observed in Figs. 4 and 5 is qualitatively expected since the magnetostatic energy density of a Bloch wall increases with decreasing film thickness as a result of the closer proximity of the free poles at the top and

the bottom of the wall. One possibility to reduce this energy contribution is that the spins inside the wall execute their 180° rotation in the plane of the surface. In the arising Néel wall, a smaller magnetostatic energy density at the internal interface of the wall is accepted as the price for removing the larger magnetostatic energy density at the top of the surface. However, in films of intermediate thickness, it is known that cross-tie walls occur. Then the magnetostatic energy density is reduced by an alternating sense of magnetic charge polarization.[33] The wall type observed in the present microstructures is in concordance with the analytical calculations of Middelhoek,[34] which propose the transition from cross-tie to Bloch walls around 90 nm film thickness in infinitely extended permalloy films. Within the experimental accuracy, patterning of the films on the micrometer scale obviously has no influence on the transition thickness between asymmetric Bloch and cross-tie walls.

V. CONCLUSIONS

We have measured the stray fields of permalloy microstructures with different geometries and various thicknesses using magnetic-force microscopy (MFM). We find good agreement between measurement and simulation concerning the line scan across an asymmetric Bloch wall. Within the point dipole approximation, this comparison allows the determination of the position of the point dipole within the MFM tip. Images were calculated from simulated magnetization patterns and compared to the experimental results yielding good agreement. Cross-tie walls are only measured in 40 and 70 nm thick elements, but never occur in thinner or thicker microstructures. In particular, we observe the cross-tie to noncross-tie transition between 70 and 100 nm film thickness for 180° walls. This is underlined by micromagnetic simulations since no cross-tie walls occur in 100 nm thick elements. As a result of the measurements, it can be concluded that in permalloy microstructures cross-tie walls only occur for film thicknesses above 20 nm and well below 100 nm.

ACKNOWLEDGMENTS

The authors would like to thank U. Merkt for persistent support and valuable discussions. The authors acknowledge financial support of the Deutsche Forschungsgemeinschaft via the Sonderforschungsbereich 508 ''Quantenmaterialien'' and the Graduiertenkolleg ''Physik nanostrukturierter Festkörper.''

[1] G. A. Prinz, Phys. Today **48(4)**, 58 (1995).
[2] S. S. P. Parkin, K. P. Roche, M. G. Samant, P. M. Rice, R. B. Beyers, R. E. Scheuerlein, E. J. O'Sullivan, S. L. Brown, J. Bucchigano, D. W. Abraham, Y. Lu, M. Rooks, P. L. Trouilloud, R. A. Wanner, and W. J. Gallagher, J. Appl. Phys. **85**, 5828 (1999).
[3] C. Yu, S. F. Lee, J. L. Tsai, E. W. Huang, T. Y. Chen, Y. D. Yao, Y. Liou, and C. R. Chang, J. Appl. Phys. **93**, 8761 (2003).
[4] H. Koo, C. Krafft, and R. D. Gomez, Appl. Phys. Lett. **81**, 862 (2002).
[5] S. A. Wolf, D. D. Awschalom, R. A. Buhrman, J. M. Daughton, S. von Molnár, M. L. Roukes, A. Y. Chtchelkanova, and D. M. Treger, Science **294**, 1488 (2001).
[6] G. Meier and T. Matsuyama, Appl. Phys. Lett. **76**, 1315 (2000).
[7] G. Meier, T. Matsuyama, and U. Merkt, Phys. Rev. B **65**, 125 327 (2002).
[8] T. Trunk, M. Redjdal, A. Kákay, M. F. Ruane, and F. B. Humphrey, J. Appl. Phys. **89**, 7606 (2001).
[9] R. Hertal and H. Kronmüller, Phys. Rev. B **60**, 7366 (1999).
[10] M. Redjdal, J. Giusti, M. F. Ruane, and F. B. Humphrey, IEEE Trans. Magn. **39**, 2684 (2003).
[11] H. A. M. van den Berg and A. H. J. van den Brandt, J. Appl. Phys. **62**, 1952 (1987).
[12] D. Goll, G. Schütz, and H. Kronmüller, Phys. Rev. B **67**, 094 414 (2003).
[13] A. Hubert and M. Rührig, J. Appl. Phys. **69**, 6072 (1991).
[14] J. McCord, A. Hubert, and A. Chizhik, IEEE Trans. Magn. **33**, 3981 (1997).
[15] Jing Shi, S. Tehrani, and M. R. Scheinfein, Appl. Phys. Lett. **76**, 2588 (2000).
[16] A. Hubert and R. Schäfer, *Magnetic Domains—The Analysis of Magnetic Microstructures* (Springer, Berlin, 1998).
[17] G. Meier, C. Pels, C. Schierholz, M. Steiner, and T. Matsuyama, Phase Transitions **76**, 459 (2003).
[18] C. Pels, Ph.D. Thesis, Universität Hamburg, 2003.
[19] V. Elings and J. Gurley, U.S. Patent No. 5,308,974 (1994), Digital Instruments, Santa Barbara, CA, May 3, 1994.
[20] M. Donahue and D. Porter, OOMMF, *Object Oriented Micromagnetic Framework*, http://math.nist.gov/oommf
[21] S. McVitie, G. S. White, J. Scott, P. Warin, and J. N. Chapman, J. Appl. Phys. **90**, 5220 (2001).
[22] D. Rugar, H. J. Mamin, G. Guethner, S. E. Lambert, J. E. Stern, I. McFadyen, and T. Yogi, J. Appl. Phys. **68**, 1169 (1990).
[23] U. Hartmann, T. Göddenhenrich, and C. Heiden, J. Magn. Magn. Mater. **101**, 263 (1991).
[24] H. J. Hug, B. Stiefel, P. J. A. van Schendel, A. Moser, R. Hofer, S. Martin, H. J. Güntherodt, S. Porthun, L. Abelmann, J. C. Lodder, G. Bochi, and R. C. O'Handley, J. Appl. Phys. **83**, 5609 (1998).
[25] J. Lohau, S. Kirsch, A. Carl, G. Dumpich, and E. F. Wassermann, J. Appl. Phys. **86**, 3410 (1999).
[26] L. Kong and S. Y. Chou, Appl. Phys. Lett. **70**, 2043 (1997).
[27] L. Kong and S. Y. Chou, J. Appl. Phys. **81**, 5026 (1997).
[28] U. Hartmann, Phys. Lett. A **137(9)**, 475 (1989).
[29] G. Meier, R. Eiselt, and M. Halverscheid, J. Appl. Phys. **92**, 7296 (2002).
[30] M. Barthelmess, A. Thieme, R. Eiselt, and G. Meier, J. Appl. Phys. **93**, 8400 (2003).
[31] A. E. LaBonte, J. Appl. Phys. **40**, 2450 (1969).
[32] M. R. Scheinfein, J. Unguris, J. L. Blue, K. J. Coakley, D. T. Pierce, R. J. Celotta, and P. J. Ryan, Phys. Rev. B **43**, 3395 (1991).
[33] R. O'Handley, *Modern Magnetic Materials: Principles and Applications* (Wiley, New York, 1999).
[34] S. Middelhoek, J. Appl. Phys. **34**, 1054 (1963).

A. Y. Chtchelkanova, and D. M. Treger, Science **294**, 1488 (2001).
[6] G. Meier and T. Matsuyama, Appl. Phys. Lett. **76**, 1315 (2000).
[7] G. Meier, T. Matsuyama, and U. Merkt, Phys. Rev. B **65**, 125327 (2002).
[8] T. Trunk, M. Redjdal, A. Kákay, M. F. Ruane, and F. B. Humphrey, J. Appl. Phys. **89**, 7606 (2001).
[9] R. Hertel and H. Kronmüller, Phys. Rev. B **60**, 7366 (1999).
[10] M. Redjdal, J. Giusti, M. F. Ruane, and F. B. Humphrey, IEEE Trans. Magn. **39**, 2684 (2003).
[11] G. Meier, C. Pels, C. Schierholz, M. Steiner, and T. Matsuyama, Phase Transitions **76**, 459 (2003).
[12] C. Pels, PhD Thesis, Universität Hamburg (2003).
[13] V. Elings, and J. Gurley, US Patent No. 5,308,974 (1994), Digital Instruments, Santa Barbara, CA, May 3, 1994.
[14] Oommf, object oriented micromagnetic framework, http://math.nist.gov/oommf
[15] S. McVitie, G. S. White, J. Scott, P. Warin, and J. N. Chapman, J. Appl. Phys. **90**, 5220 (2001).
[16] D. Rugar, H. J. Mamin, G. Guethner, S. E. Lambert, J. E. Stern, I. McFadyen, and T. Yogi, J. Appl. Phys. **68**, 1169 (1990).
[17] U. Hartmann, T. Göddenhenrich, and C. Heiden, J. Magn. Magn. Mater. **101**, 263 (1991).
[18] H. J. Hug, B. Stiefel, P. J. A. van Schendel, A. Moser, R. Hofer, S. Martin, H. J. Güntherodt, S. Porthun, L. Abelmann, J. C. Lodder, G. Bochi, and R. C. O'Handley, J. Appl. Phys. **83**, 5609 (1998).
[19] J. Lohau, S. Kirsch, A. Carl, G. Dumpich, and E. F. Wassermann, J. Appl. Phys. **86**, 3410 (1999).
[20] L. Kong and S. Y. Chou, Appl. Phys. Lett. **70**, 2043 (1997).
[21] L. Kong and S. Y. Chou, J. Appl. Phys. **81**, 5026 (1997).
[22] U. Hartmann, Phys. Lett. A **137** (9), 475 (1989).
[23] G. Meier, R. Eiselt, and M. Halverscheid, J. Appl. Phys. **92**, 7296 (2002).
[24] M. Barthelmess, A. Thieme, R. Eiselt, and G. Meier, J. Appl. Phys. **93**, 8400 (2003).
[25] A. E. LaBonte, J. Appl. Phys. **40**, 2450 (1969).
[26] M. R. Scheinfein, J. Unguris, J. L. Blue, K. J. Coakley, D. T. Pierce, R. J. Celotta, and P. J. Ryan, Phys. Rev. B **43**, 3395 (1991).
[27] R. O'Handley, *Modern Magnetic Materials: Principles and Applications* (John Wiley & Sons, Inc., New York, 1999).
[28] S. Middelhoek, J. Appl.Phys. **34**, 1054 (1963).

5.5 Permalloy sample in external magnetic fields

The permalloy sample described in chapter 3 and publication [P4] is further investigated by applying external magnetic fields in the plane of the sample in two directions, namely parallel and perpendicular to the easy magnetization axes. MFM measurements [P5] as well as simulations are performed in detail on the 1 μm×1 μm and 1 μm×2 μm sized geometries with 10, 20, 40, 70, and 100 nm film thickness. For this purpose, an external field of up to 50 mT is applied in both directions, and all thicknesses of one geometry are measured simultaneously, whereas in the simulations external magnetic fields of up to 100 mT are applied depending on the saturation field of the single particles. The magnetization is simulated separately for each element in dependence of the external magnetic field, resulting in a hysteresis curve. Here, the same parameters as described in publication [P4] and in table (4.1) are used. The external magnetic field is increased in steps of 1 mT. The simulations cannot be performed on the 1 μm×2 μm sized geometry in a thickness of 100 nm, because of the enormous computing time. For the same reason, only one part of the hysteresis is calculated starting towards positive field direction with the initial magnetization curve, not shown in the figures for clarity reasons. Figure 5.7 shows the magnetization of the symmetric 1 μm×1 μm elements with all five film thicknesses. Note that for the 70 and 100 nm thick particles the magnetic field is increased up to 100 mT to guarantee saturation. For a comparison, also the magnetization of the 20 nm thick element is simulated in fields up to 100 mT, whereas for the 10 and 40 nm

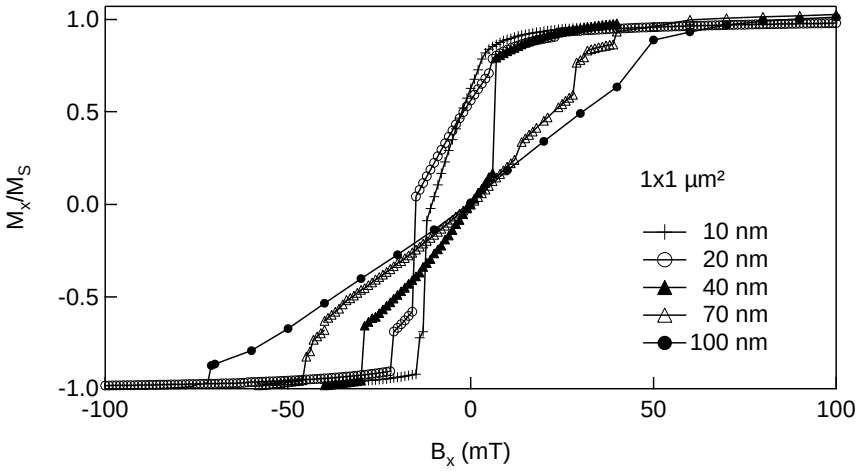

Figure 5.7: Simulated hysteresis curves for the 1 μm×1 μm elements in the thicknesses of 10, 20, 40, 70, and 100 nm. The magnetization M_x in the direction of the external field is normalized with respect to the saturation magnetization M_s and is plotted versus the external magnetic field B_x.

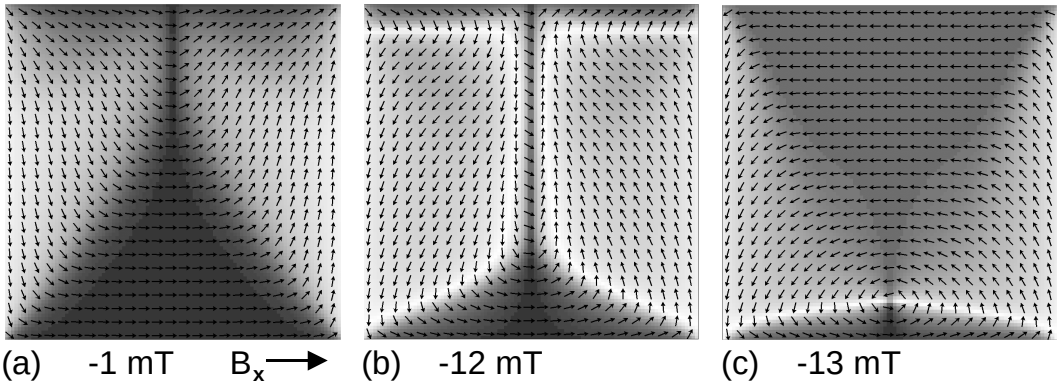

Figure 5.8: Magnetization patterns revealing the process of magnetization change from positive to negative saturation in the 1 μm×1 μm geometry with 10 nm film thickness (compare hysteresis in Fig. 5.7): (a) C-state at -1 mT after positive saturation, (b) at -12 mT before first irreversible jump, and (c) at -13 mT between first and second irreversible change in magnetization.

thick elements a field of 40 mT is sufficient. The remanences of the 10 and 20 nm thick particles are comparable, whereas for 40 nm film thickness the first irreversible change in magnetization going from positive to negative fields occurs at 6 mT already. The magnetization behavior of the two thickest particles differs in so far as the changes in magnetization occur even earlier. The 70 nm thick geometry shows two small irreversible jumps at 29 and 14 mT already. Then the magnetization changes in a reversible manner except of a small irreversible step when saturation is achieved in negative direction. The three thickest particles have zero remanence, i.e., the coercive field is also zero. It has to be mentioned that in the calculation for the thickest particle, the magnetic field was decreased in large steps of 10 mT for computing time reasons. Only at the irreversible step close to negative saturation, the step size was reduced to 1 mT for a better resolution. For this reason, irreversible changes in magnetization, comparable to the first ones for the 70 nm thick element, cannot be resolved. In the sequence of the magnetization patterns, a difference in the magnetization behavior of the 10 and 70 nm thick elements is found. After saturation, the thin particle is in a C-state as shown in Fig. 5.8(a) and domains with negative magnetization direction enter the particle from the sides (Fig. 5.8(b)). They grow reversibly until the last small domains with positive magnetization direction disappear in two irreversible steps and negative saturation is achieved. Figure 5.8(c) shows the magnetization pattern at -13 mT before the final irreversible step occurs. In contrast, the 70 nm thick element is in an S-state after saturation as shown in Fig. 5.9(a) and two reversed oriented domains enter from the top and bottom as shown in Fig. 5.9(b). After an irreversible step at 14 mT, one cross-like pattern with two small crosses

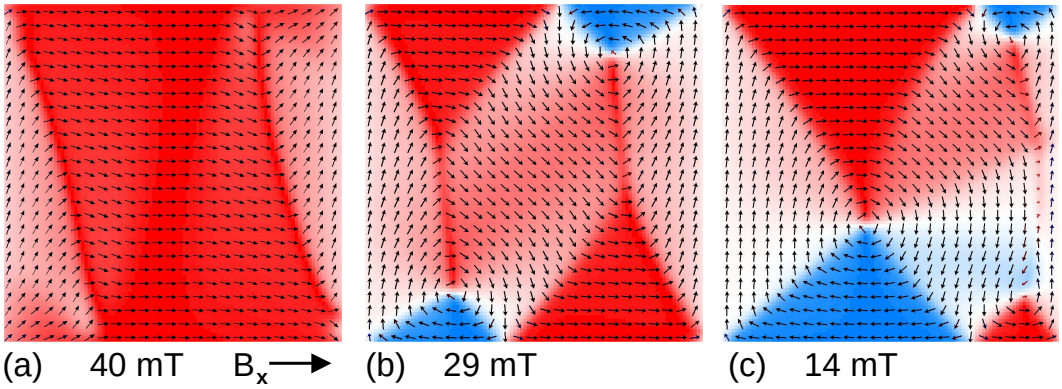

Figure 5.9: Magnetization patterns revealing the process of magnetization change from positive to negative saturation in the 1 μm×1 μm geometry with 70 nm film thickness (compare hysteresis in Fig. 5.7): (a) S-state after positive saturation, (b) at 29 mT after first irreversible jump, and (c) at 14 mT after second irreversible change in magnetization.

in the corners is formed (see Fig. 5.9(c)). The center of the large cross gradually moves through the particle until the reversed oriented domain displaces the domain with positive magnetization direction in an irreversible step, and saturation is reached. In Fig. 5.10 the magnetization behavior of the 1 μm×2 μm sized elements with the thicknesses 10, 20, 40, and 70 nm is shown, while the external field is applied along the easy axes. The process of magnetization change is comparable to the one in Fig. 5.7 for the 1 μm×1 μm elements. The three thinner

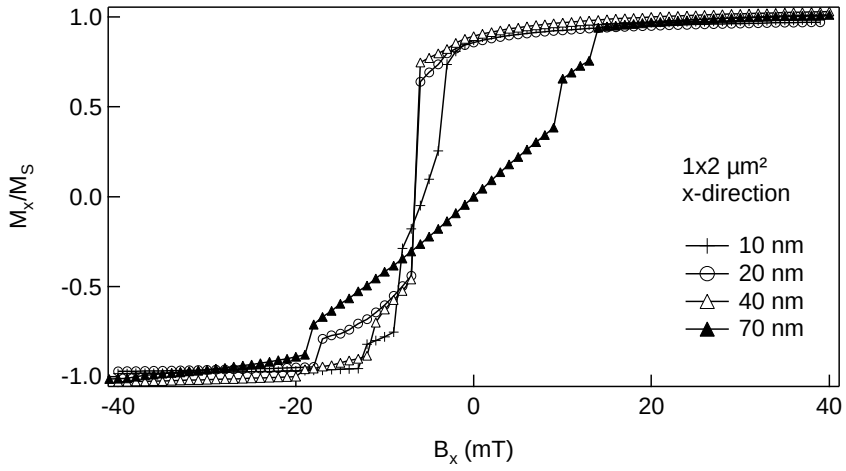

Figure 5.10: Simulated hysteresis curves for the 1 μm×2 μm sized particles in the thicknesses of 10, 20, 40, and 70 nm. The external field is applied in x-direction parallel to the easy axis of the rectangle.

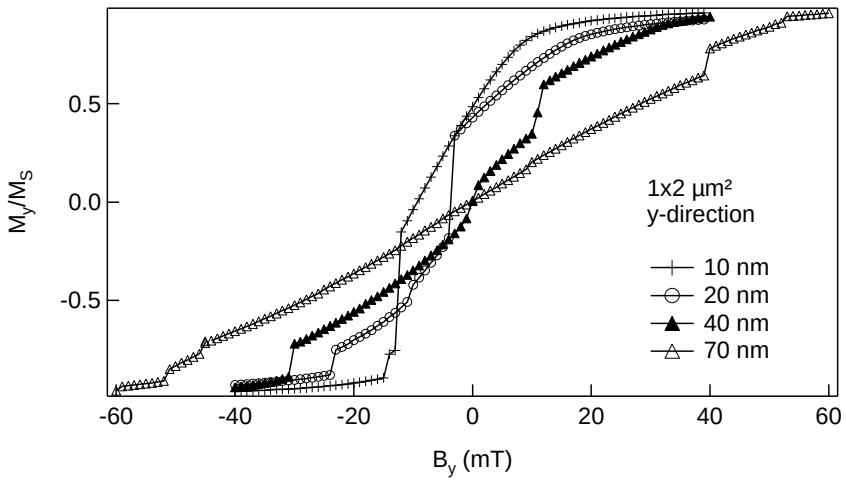

Figure 5.11: Simulated hysteresis curves for the 1 μm×2 μm sized particles in the thicknesses of 10, 20, 40, and 70 nm. The external field is applied along the hard axis of the rectangle.

particles have almost the same remanence and, as before, the 10 nm thick element shows a smaller coercive field than the 20 nm thick one. The 40 nm thick rectangle has a different behavior compared to the quadratic shape. Its behavior resembles the one of the 20 nm thick particle. However, saturation is obtained in two irreversible steps, whereas the 20 nm thick element passes only one irreversible change. Again, the 70 nm thick rectangle has no remanence in this fild direction. Its magnetization behavior corresponds to the one of the 70 nm

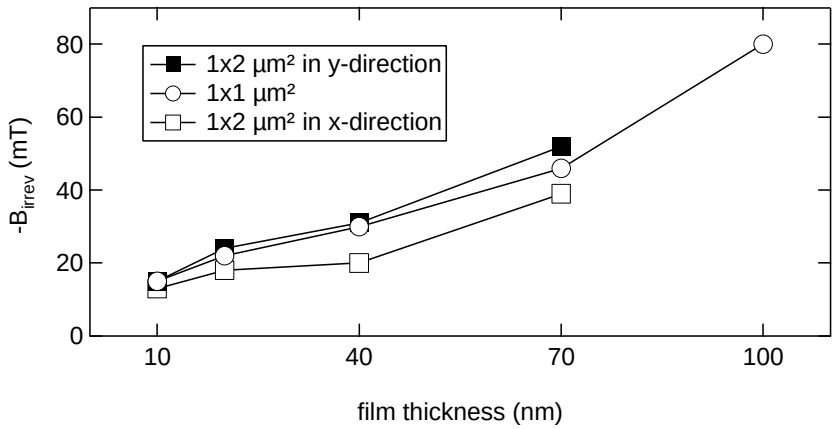

Figure 5.12: Field needed for saturation of the 1 μm×1 μm and the 1 μm×2 μm sized elements. The simulated data is taken from Figs. 5.7, 5.10, and 5.11. B_{irrev} refers to the field after the last irreversible change in magnetization before saturation is achieved.

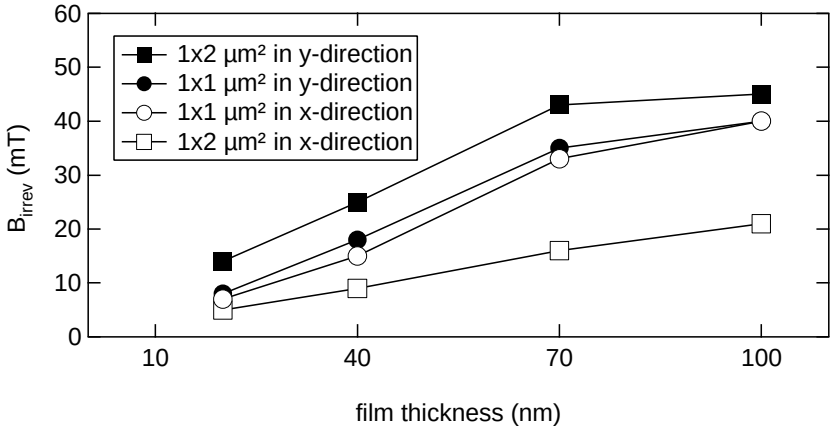

Figure 5.13: Field needed for saturation of the 1 μm×1 μm and the 1 μm×2 μm sized elements as measured by magnetic-force microscopy for film thicknesses of 20, 40, 70, and 100 nm.

thick 1 μm×1 μm element. After saturation the particle is in an S-state. In an irreversible step at 13 mT two negative oriented domains enter from the top and bottom, which form a double cross after another irreversible step at 9 mT. The negative oriented domains widen until saturation is reached. If the external magnetic field is applied along the hard axis (see Fig. 5.11), the remanence of the two thinnest particles is dramatically reduced. The 40 and 70 nm thick elements have no remanence again. Also the field needed for saturation has increased. This is shown in Fig. 5.12. Here, the effect of shape anisotropy is also obvious in so far as the saturating magnetic fields for the 1 μm×2 μm sized particles are lower in the direction of the easy axis than the ones for the symmetric 1 μm×1 μm elements. The same effect is observed in the experiment as depicted in Fig. 5.13. As described in the previous publication [P4], the MFM measurements cannot be analyzed for 10 nm film thickness because of interactions between cantilever and sample. Unlike in the simulations, the external field was applied in both directions for the symmetric 1 μm×1 μm particles. As expected, the saturating fields are very similar. The small discrepancies are due to impurities or slight asymmetries in the shape of the particles.

Chapter 6

Summary

Microstructured ferromagnets have been analyzed with respect to their domain configuration by comparing simulations to experimental results. In this context, the computer code has been extended. It now allows to calculate data that can be directly compared to measurements.

In a first step, the micromagnetic behavior of a pair of permalloy contacts, which are to be used in spintronic devices, was investigated by micromagnetic simulations of the magnetization. The calculated domain pattern at zero magnetic field was compared to magnetic-force microscopy measurements in the as-prepared state. It could be shown that the two different domain patterns observed in the measurements correspond to the two energetically most favorable magnetization configurations resulting from simulations. Further, the interaction of the two neighboring electrodes was investigated by simulations of the hysteresis curves for various distances between the contacts. For a distance in the order of the particle size, namely 500 nm, the simulated hysteresis curve of the interacting electrode pair corresponds to the sum of the single electrode signals. Calculated hysteresis curves of the magnetization were further compared to the signals of Hall μ-magnetometry on iron contacts.

A computer code was developed to calculate the signal of Hall μ-magnetometry from the magnetization data. For these calculations, the magnetization data is interpreted as an array of magnetic dipoles, namely one dipole per lattice cell. The stray fields of these dipoles are calculated and the resulting stray field can be computed in arbitrary distances above the sample. The Hall signal results from averaging the field values above the Hall cross. With help of this tool, the stray field strengths generated by the electrodes could be compared directly and a good overall agreement was found. Additionally, the stray field could be visualized for an analysis of the local stray field in the semiconductor channel.

A further aim of this thesis was to achieve a direct comparison between magnetic-force microscopy and calculated magnetization patterns. For this, the calculation of the stray field serves as a basis, since the experimental signal corresponds ap-

proximately to the second derivative of the out-of-plane component of the stray field in out-of-plane direction. Employing these calculations, not only the magnetization patterns of the above mentioned electrodes could be easily compared to simulations, but also further investigations of the magnetization behavior in the as-prepared state as well as in external magnetic fields could be performed. Special interest was drawn to the investigation of domain walls in dependence of particle thickness. Magnetic-force microscopy measurements were performed on a permalloy sample comprising neighboring geometries of identical lateral shape in various thicknesses. Simulated and measured signals were compared directly and led to very good agreement. With both techniques, in the study of domain walls a transition between cross-tie and Bloch wall was observed between 70 and 100 nm in the structured material, corresponding to literature values for extended films.

As a conclusion, the calculation of experimental signals from simulation data is a powerful tool for the analysis of domain configurations, as well as for a better understanding of experimental methods. With this tool at hand, the optimization of domain structures for applications in spintronic devices and electron transport in ferromagnetic micro- and nanostructures is more easily feasible and represents an important basis for further work in this field.

Appendix A

Derivatives of the stray field

For the calculation of the MFM signal from simulated data, the second derivative of the stray field has to be determined, as mentioned in chapter 4. The z-component of the stray field at a certain point P with coordinates x, y, and z results from the sum of the stray fields of all magnetic dipoles (see equation (4.2)) in the lattice:

$$H_z = \frac{1}{4\pi} \sum_i^N \frac{3(m_{ix}x + m_{iy}y + m_{iz}z)z - m_{iz}(x^2+y^2+z^2)}{(x^2+y^2+z^2)^{5/2}} .$$

Here, m_{ix}, m_{iy}, and m_{iz} are the components of the magnetic dipole in cell i with N being the total number of lattice cells. x, y, and z are the coordinates of point P. The first derivatives are:

$$\frac{\partial H_z}{\partial x} = \frac{1}{4\pi} \sum_i^N \left(\frac{3m_{iz}x^3 - 12m_{ix}zx^2 - (15z(m_{iy}y + m_{iz}z) - 3m_{iz}(y^2+z^2))x}{(x^2+y^2+z^2)^{7/2}} + \frac{3m_{ix}z(y^2+z^2)}{(x^2+y^2+z^2)^{7/2}} \right) ,$$

$$\frac{\partial H_z}{\partial y} = \frac{1}{4\pi} \sum_i^N \left(\frac{3m_{iz}y^3 - 12m_{iy}zy^2 - (15z(m_{ix}x + m_{iz}z) - 3m_{iz}(x^2+z^2))y}{(x^2+y^2+z^2)^{7/2}} + \frac{3m_{iy}z(x^2+z^2)}{(x^2+y^2+z^2)^{7/2}} \right) ,$$

and

$$\frac{\partial H_z}{\partial z} = \frac{1}{4\pi}\sum_i^N \left(\frac{-6m_{iz}z^3 - 12(xm_{ix}+ym_{iy})z^2 + 3m_{iz}(x^2+y^2)z}{(x^2+y^2+z^2)^{7/2}} + \frac{3(x^2+y^2)(xm_{ix}+ym_{iy}+2m_{iz})}{(x^2+y^2+z^2)^{7/2}} \right).$$

The second derivatives are:

$$\frac{\partial^2 H_z}{\partial x^2} = \frac{1}{4\pi}\sum_i^N \left(\frac{-12m_{iz}x^4 + 60m_{ix}zx^3 + (9m_{iz}(y^2+z^2)+6A)x^2}{(x^2+y^2+z^2)^{9/2}} - \frac{(24m_{ix}z(y^2+z^2)+7B)x + A(y^2+z^2)}{(x^2+y^2+z^2)^{9/2}} \right)$$

with

$$\begin{aligned} A &= 15z(m_{iy}y + m_{iz}z) - 3m_{iz}(y^2+z^2) \text{ and} \\ B &= 3m_{ix}z(y^2+z^2)\,, \end{aligned}$$

$$\frac{\partial^2 H_z}{\partial y^2} = \frac{1}{4\pi}\sum_i^N \left(\frac{-12m_{iz}y^4 + 60m_{iy}zy^3 + (9m_{iz}(x^2+z^2)+6A')y^2}{(x^2+y^2+z^2)^{9/2}} - \frac{(24m_{iy}z(x^2+z^2)+7B')y + A'(x^2+z^2)}{(x^2+y^2+z^2)^{9/2}} \right)$$

with

$$\begin{aligned} A' &= 15z(m_{ix}x + m_{iz}z) - 3m_{iz}(x^2+z^2) \text{ and} \\ B' &= 3m_{iy}z(x^2+z^2)\,, \end{aligned}$$

and

$$\frac{\partial^2 H_z}{\partial z^2} = \frac{3}{4\pi}\sum_i^N \left(\frac{3m_{iz}(x^2+y^2+z^2)^2 - 15(xm_{ix}+ym_{iy}+zm_{iz})(x^2+y^2+z^2)z}{(x^2+y^2+z^2)^{9/2}} - \frac{15m_{iz}(x^2+y^2+z^2)z^2 + 35(xm_{ix}+ym_{iy}+zm_{iz})z^3}{(x^2+y^2+z^2)^{9/2}} \right).$$

Appendix B

Measurements and simulations of the permalloy sample

This appendix gives an overview of MFM measurements on the permalloy sample described in chapter 3 and publication [P4]. When calculated, the corresponding simulated images are included for comparison. They are calculated in a distance of 40 nm above the sample unless otherwise noted. The measured images either show a group of 20 particles with film thicknesses as illustrated in Fig. 3.2(b) or one row of the group with film thicknesses of 10, 20, 40, 70, and 100 nm. The latter are as well shown in the simulated images unless otherwise indicated.

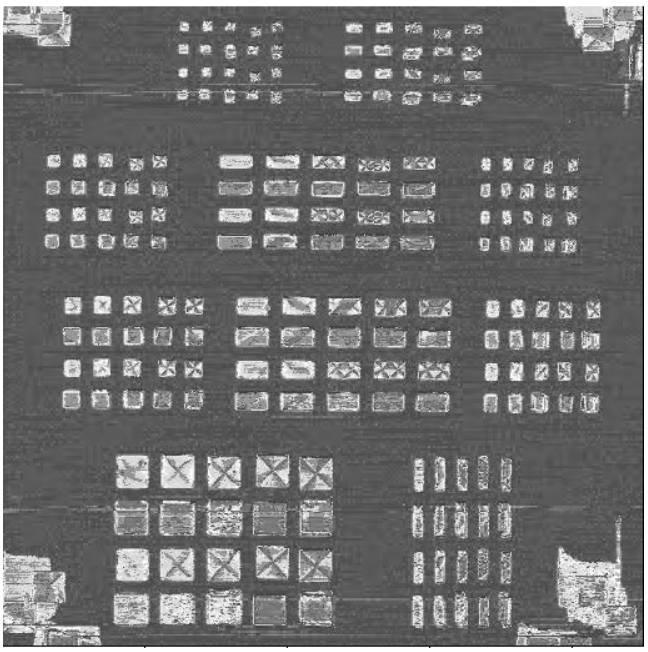

Figure B.1: Magnetic signal of the permalloy sample with a scan range of 100 μm $\times$ 100 μm.

1 μm×1 μm

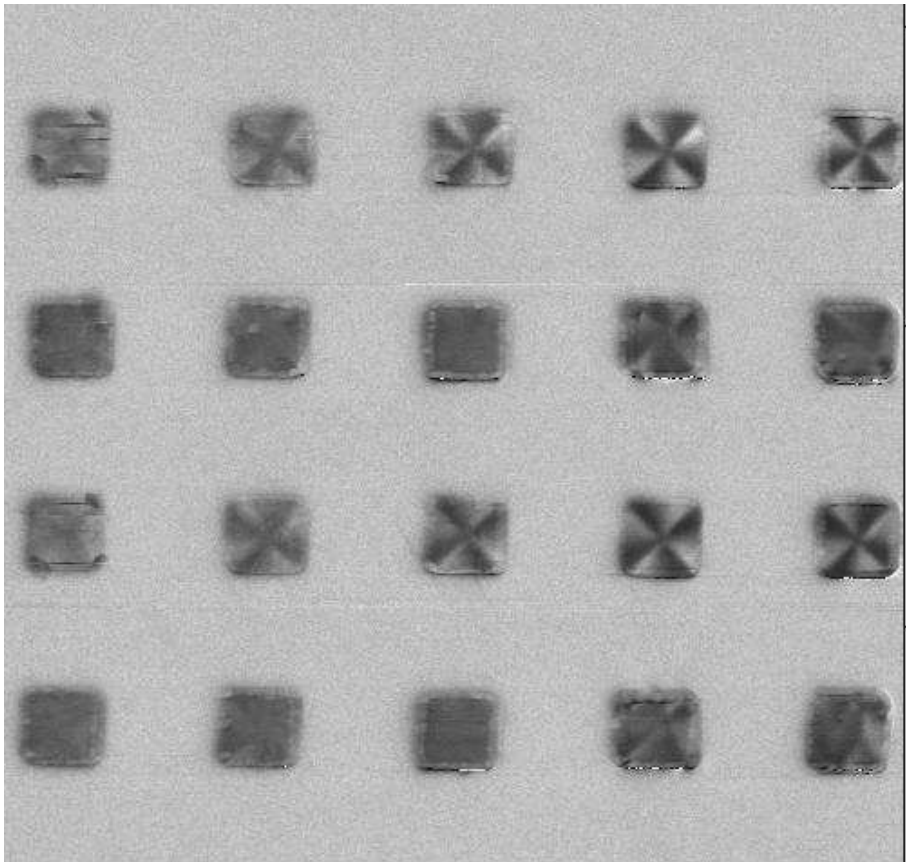

Figure B.2: MFM image of the 1 μm×1 μm sized structures.

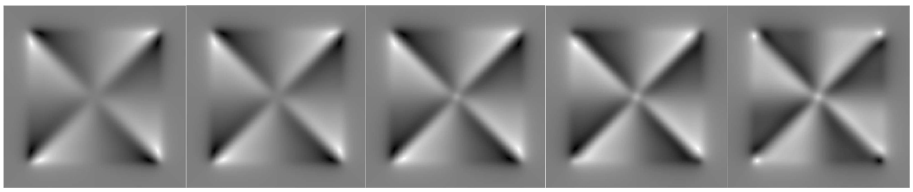

Figure B.3: Corresponding simulated images.

1 μm×1.5 μm

Figure B.4: MFM image of the 1 μm×1.5 μm sized structures.

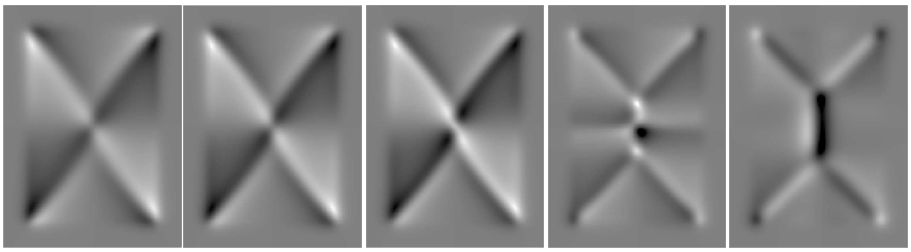

Figure B.5: Corresponding simulated images. The simulations were performed with various initial magnetization patterns. The energetically most favorable simulations are shown here, resulting from an envelope pattern for the 70 nm thick structure, whereas for all others a cross was chosen as starting configuration. The images are calculated for a distance of 90 nm above the sample.

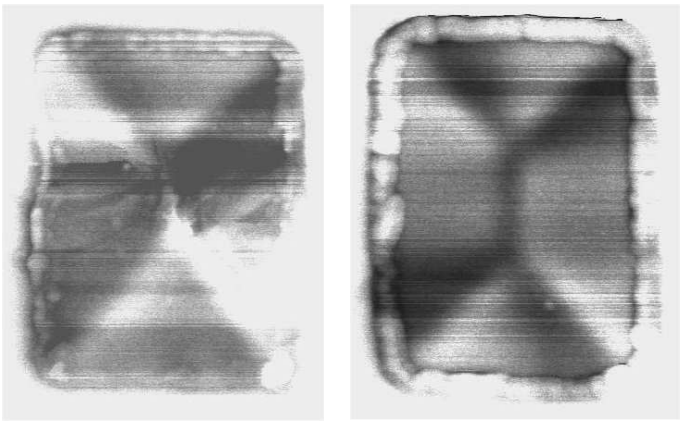

Figure B.6: High resolution MFM images of the 40 and 100 nm thick elements. Tear-off edges can be seen in both geometries.

1 μm×4 μm

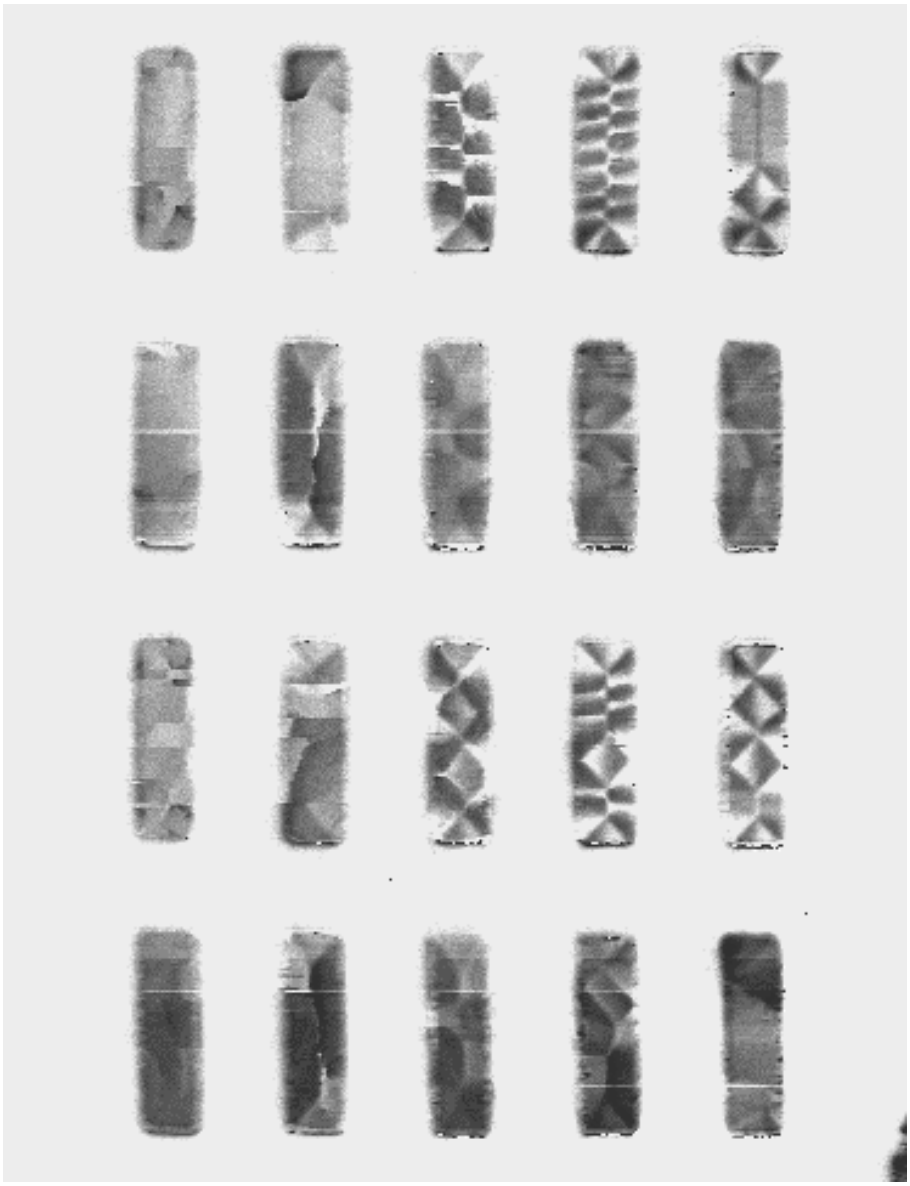

Figure B.7: MFM image of the 1 μm×4 μm sized structures.

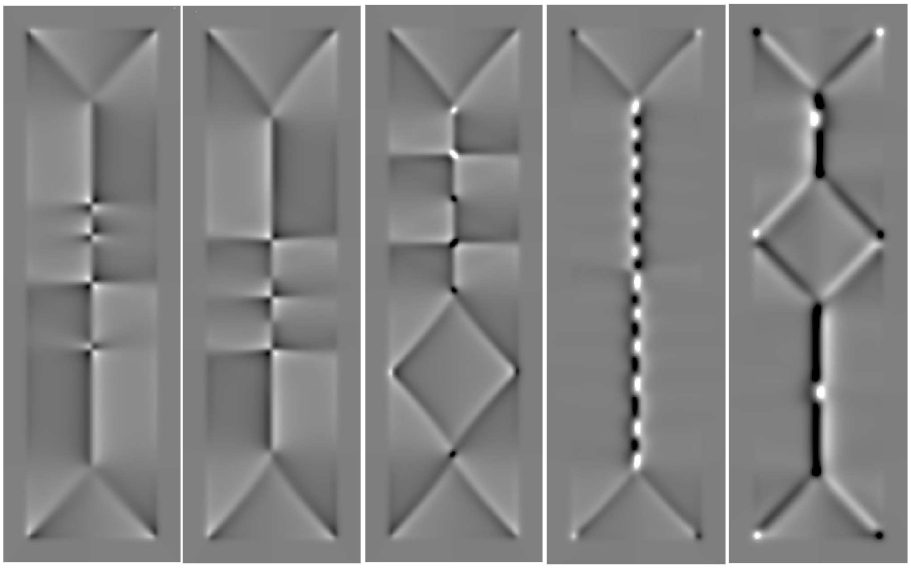

Figure B.8: Corresponding simulated images using an envelope pattern as initial configuration.

1.5 μm×1.5 μm

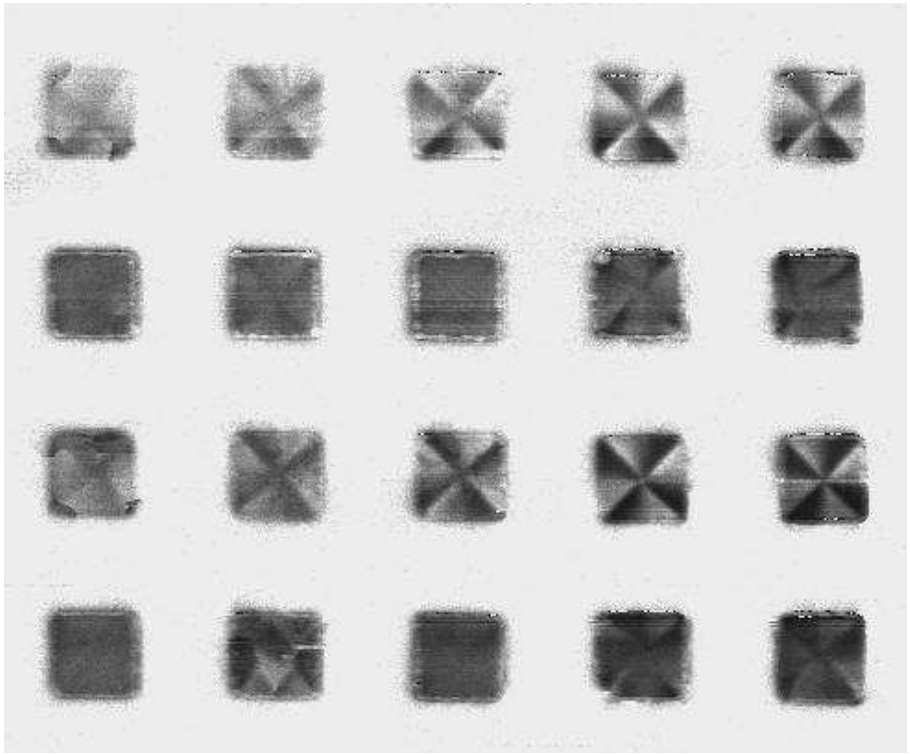

Figure B.9: MFM image of the 1.5 μm×1.5 μm sized structures.

1 μm×2 μm

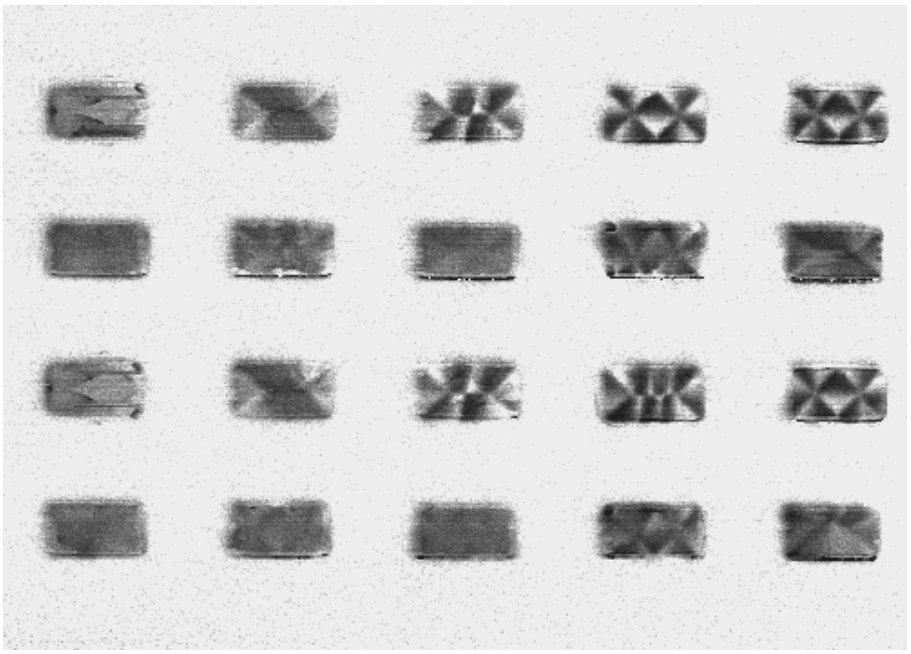

Figure B.10: MFM image of the 1 μm×2 μm sized structures.

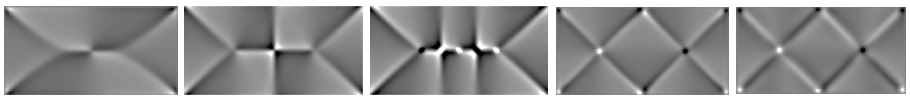

Figure B.11: Corresponding simulated images using the following patterns as initial magnetization for the energetically most favorable simulations: a cross for 10 nm, an envelope pattern for 20 and 40 nm, and a double cross for 70 and 100 nm film thickness.

1.5 μm×2 μm

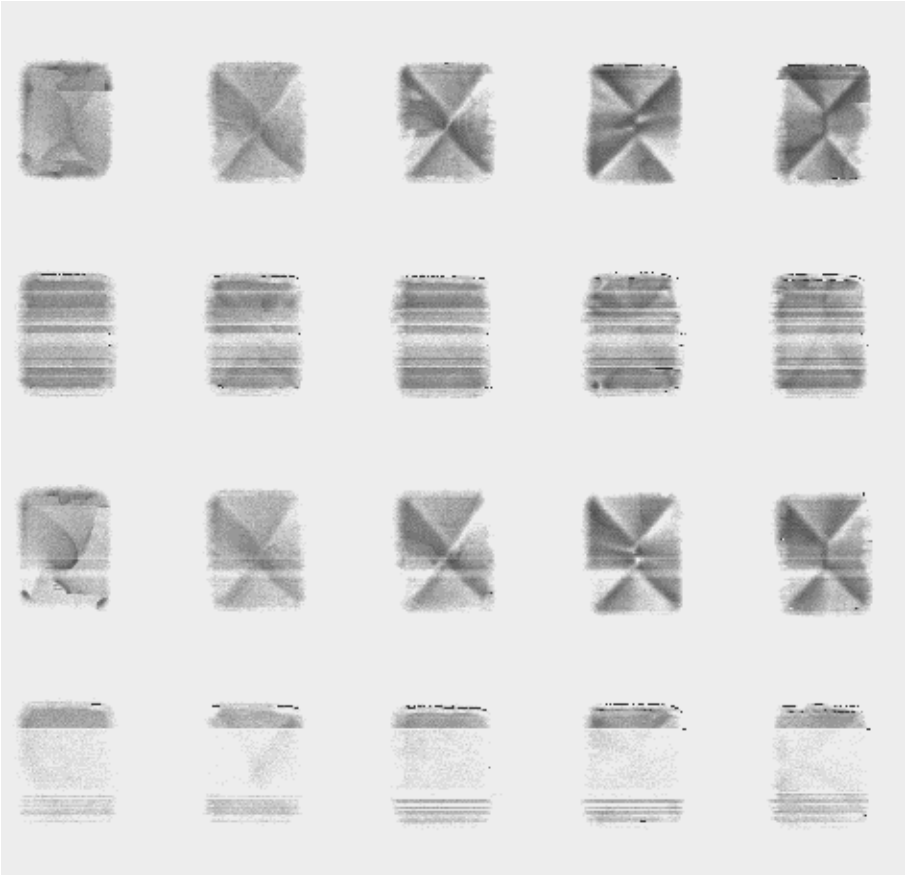

Figure B.12: MFM image of the 1.5 μm×2 μm sized structures.

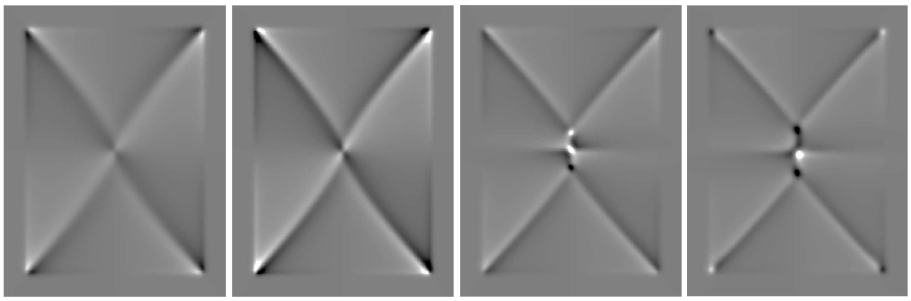

Figure B.13: Corresponding simulated images for 10 to 70 nm film thickness.

2 μm×2 μm

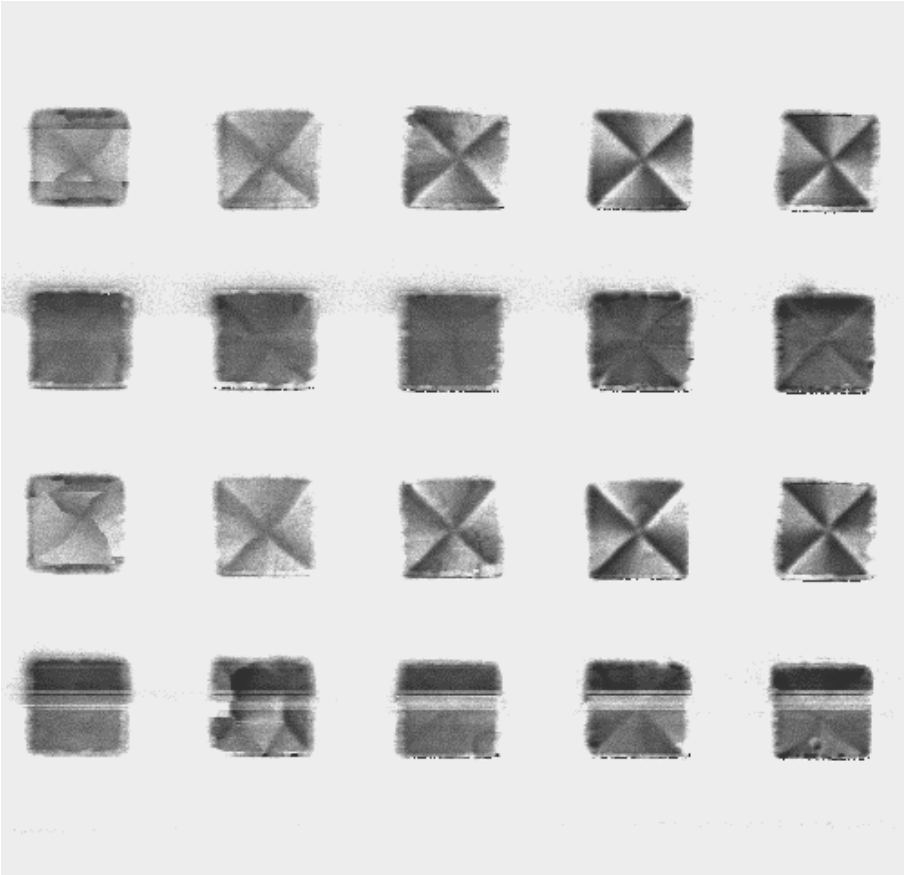

Figure B.14: MFM image of the 2 μm×2 μm sized structures.

1.5 μm×4 μm

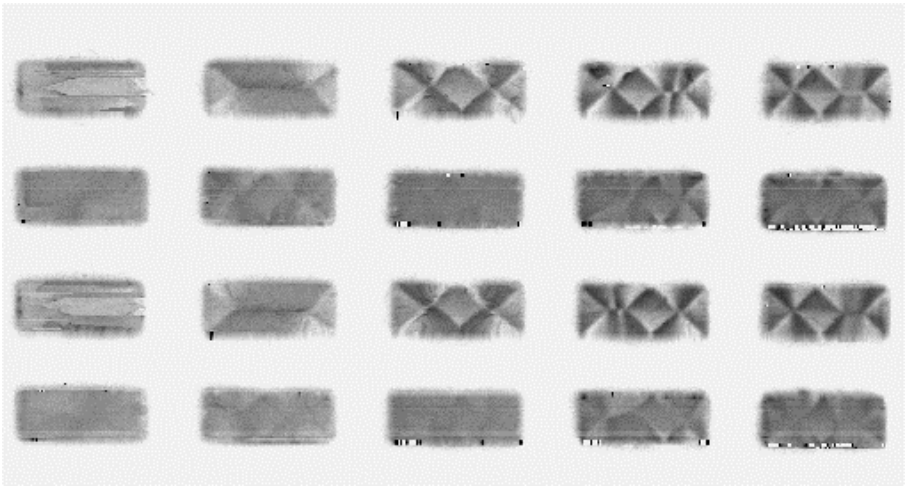

Figure B.15: MFM image of the 1.5 μm×4 μm sized structures.

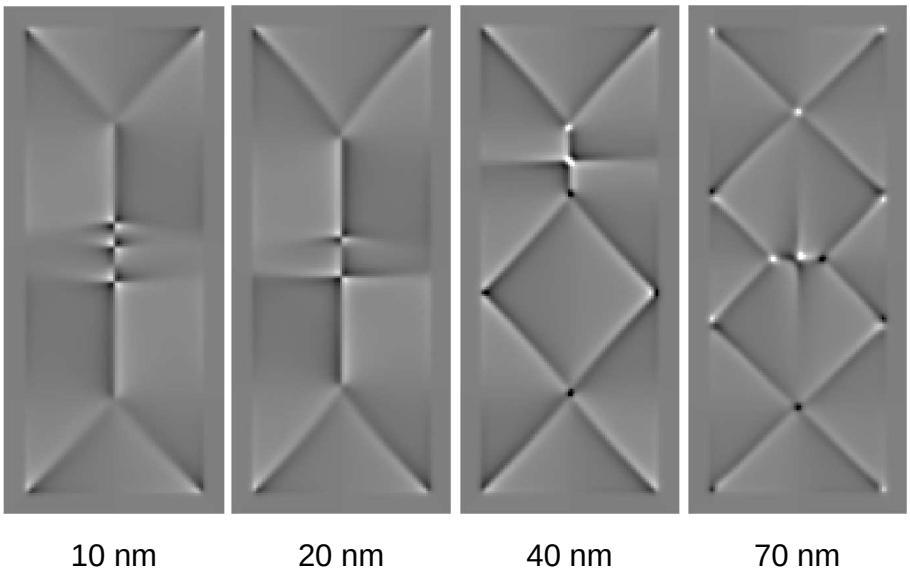

Figure B.16: Corresponding simulated images for 10 to 70 nm film thickness.

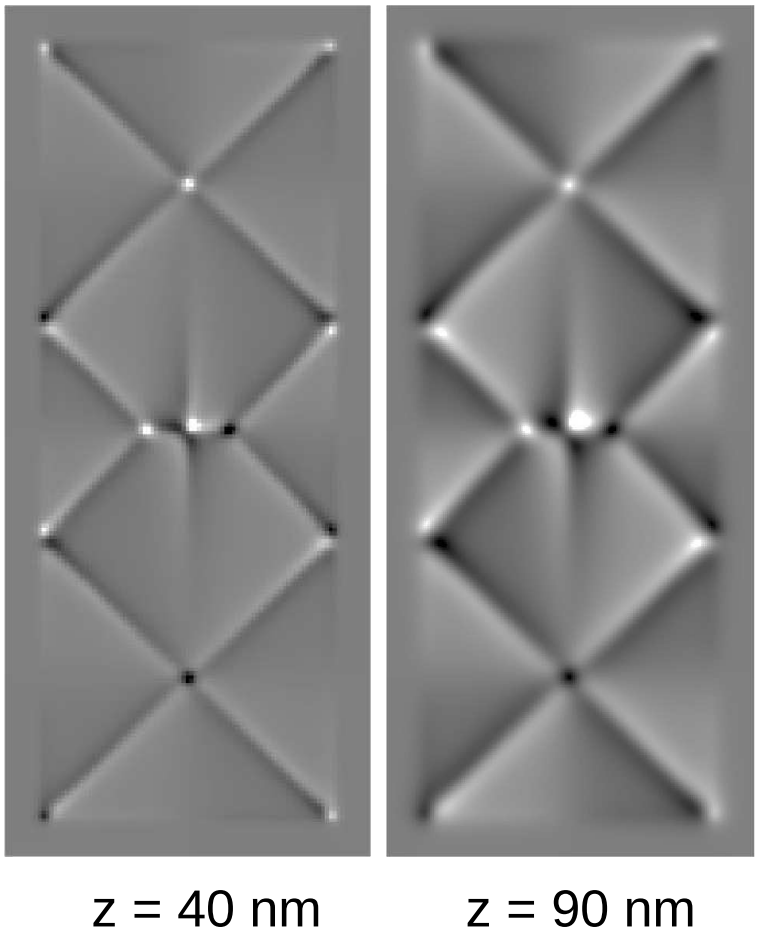

Figure B.17: Images for the 70 nm thick element simulated in a distance of 40 and 90 nm above the sample (see publication [P4]).

2 μm×4 μm

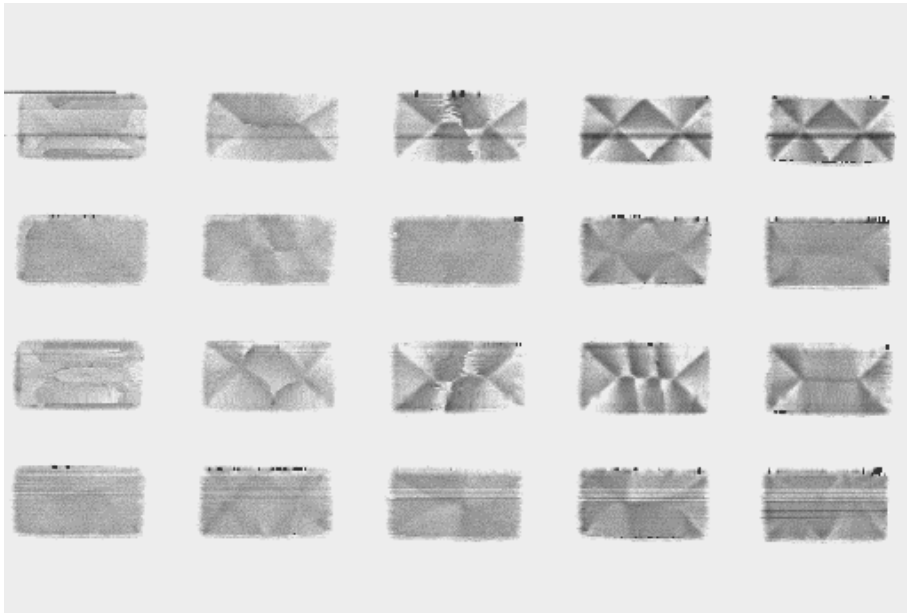

Figure B.18: MFM image of the 2 μm×4 μm sized structures.

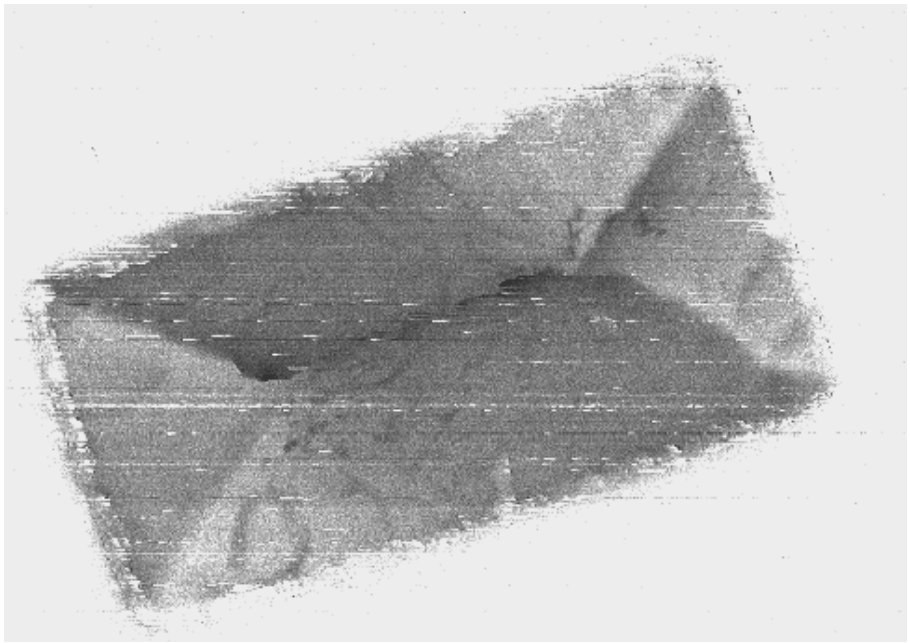

Figure B.19: High resolution MFM image of the 20 nm thick element.

4 μm×4 μm

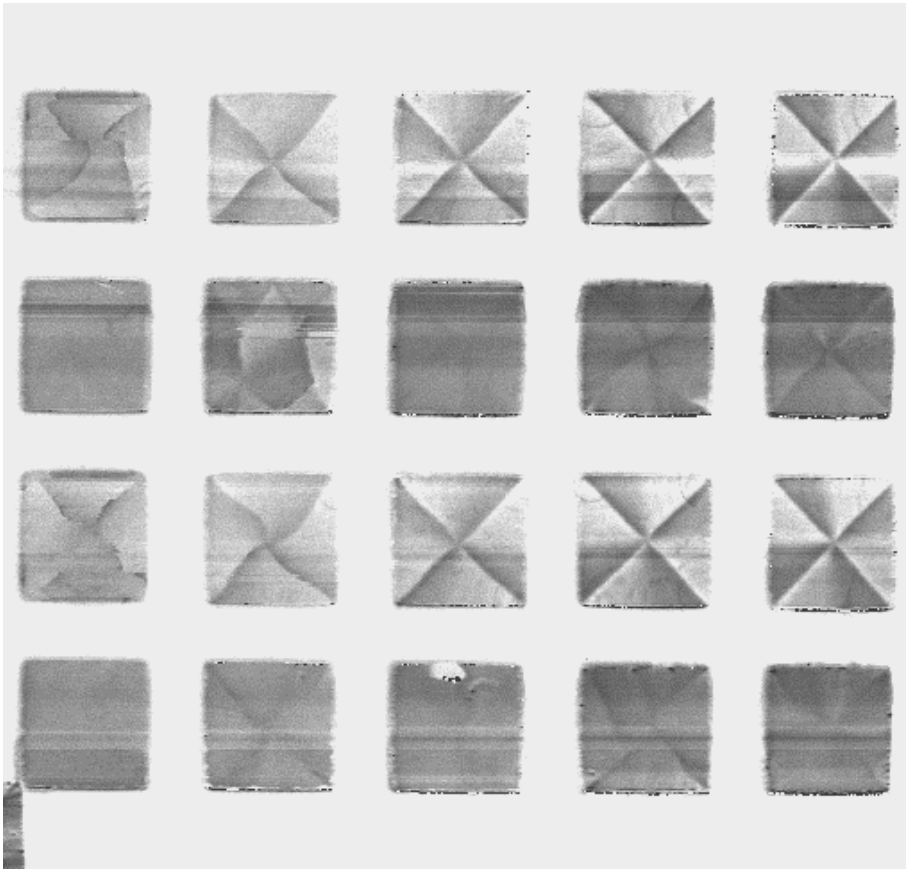

Figure B.20: MFM image of the 4 μm×4 μm sized structures.

Bibliography

[1] J. L. Simonds, *Magnetoelectronics Today and Tomorrow*, Physics Today **48**, 26 (1995).

[2] S. S. P. Parkin, K. P. Roche, M. G. Samant, P. M. Rice, R. B. Beyers, R. E. Scheuerlein, E. J. O'Sullivan, S. L. Brown, J. Bucchigano, D. W. Abraham, Yu Lu, M. Rooks, P. L. Trouilloud, R. A. Wanner, and W. J. Gallagher, *Exchange-biased magnetic tunnel junctions and application to nonvolatile magnetic random access memory*, J. Appl. Phys, **85**, 5828 (1999).

[3] E. D. Dahlberg and J.-G. Zhu, *Micromagnetic Microscopy and Modeling*, Physics Today **48**, 34 (1995).

[4] D. D. Awschalom and D. P. DiVincenzo, *Complex Dynamics of Mesoscopic Magnets*, Physics Today **48**, 43 (1995).

[5] T. Trunk, M. Redjdal, A. Kákay, M. F. Ruane, and F. B. Humphrey, *Domain wall structure in Permalloy films with decreasing thickness at the Bloch to Néel transition*, J. Appl. Phys. **89**, 7606 (2001).

[6] Gary A. Prinz, *Spin-Polarized Transport*, Physics Today **48**, 58 (1995).

[7] S. A. Wolf, D. D. Awschalom, R. A. Buhrman, J. m. Daughton, M. L. Roukes S. von Molnár, A. Y. Chtchelkovna, and D. M. Treger, *Spintronics: A Spin-Based Electronics Vision for the Future*, Science **294**, 1488 (2001).

[8] D. Grundler, *Ballistic spin-filter transistor*, Phys. Rev. B **63**, R161307 (2001).

[9] G. Meier and T. Matsuyama, *Magnetic electrodes for spin-polarized injection into InAs*, Appl. Phys. Lett. **76**, 1315 (2000).

[10] C. Kittel, *Einführung in die Festkörperphysik*, Oldenbourg, München, 1993.

[11] A. H. Morrish, *The Physical Principles of Magnetism*, Wiley, New York, 1965.

[12] A. Hubert and R. Schäfer, *Magnetic Domains: The Analysis of Magnetic Microstructures*, Springer, 1998.

[13] C. Zener, *Interaction Between the d Shells in the Transition Metals*, Phys. Rev. **81**, 440 (1951).

[14] C. Zener, *Interaction Between the d Shells in the Transition Metals. Calculations of the Weiss Factors in Fe, Co and Ni.*, Phys. Rev. **83**, 299 (1951).

[15] L. Berger, *Motion of a magnetic domain wall traversed by fast-rising current pulses*, J. Appl. Phys. **71**, 2721 (1992).

[16] I. I. Mazin, *How to Define and Calculate the Degree of Spin Polarization in Ferromagnets*, Phys. Rev. Lett. **83**, 1427 (1999).

[17] R. C. O'Handley, *Modern magnetic materials: Principles and applications*, Wiley, New York, 2000.

[18] K. Kopitzki, *Einführung in die Festkörperphysik*, Teubner, Stuttgart, 1993.

[19] W. Heisenberg, *Mehrkörperproblem und Resonanz in der Quantenmechanik*, Z. Phys. **38**, 441 (1926).

[20] P. A. M. Dirac, *On the theory of quantum mechanics*, Proc. Roy. Soc. **112A**, 661 (1926).

[21] K. Honda and S. Kaya, *On the Magnetization of Single Crystals of Iron*, Sci. Rep. Tohoky Imp. Univ. **15**, 721 (1926).

[22] F. Schmidt and A. Hubert, *Domain observations on CoCr-layers with a digitally enhanced Kerr-microscope*, J. Magn. Magn. Mat. **61**, 307 (1986).

[23] R. P. Cowburn, D. K. Koltsov, A. O. Adeyeye, and M. E. Welland, *Probing submicron nanomagnets by magneto-optics*, Appl. Phys. Lett. **73**, 3947 (1998).

[24] E. C. Stoner and E. P. Wohlfarth, *A Mechanism of Magnetic Hysteresis in Heterogeneous Alloys*, Phil. Trans. Royal Soc. London **A240**, 599 (1948).

[25] L. Néel, Compt. rend., Paris **241**, 533 (1955).

[26] A. E. LaBonte, *Two-Dimensional Bloch-Type Domain Walls in Ferromagnetic Films*, J. Appl. Phys. **40**, 2450 (1969).

[27] A. Hubert, *Stray-Field-Free Magnetization Configurations*, Phys. Stat. Sol. **32**, 519 (1969).

[28] A. Hubert, *Stray-Field-Free and Related Domain Wall Configurations in Thin Magnetic Films (II)*, Phys. Stat. Sol. **38**, 699 (1970).

[29] A. Aharoni, *Asymmetry in Domain Walls*, Phys. Stat. Sol. **18**, 661 (1973).

[30] M. R. Scheinfein, J. Unguris, J. L. Blue, K. J. Coakley, D. T. Pierce, and R. J. Celotta, *Micromagnetics of domain walls at surfaces*, Phys. Rev. B **43**, 3395 (1991).

[31] M. Redjdal, Kákay, M. F. Ruane, and F. B. Humphrey, *Cross-tie Walls in Thin Permalloy Films*, IEEE Trans. Magn. **38**, 2471 (2002).

[32] E. E. Huber, D. O. Smith, and J. B. Goodenough, *Domain-Wall Structure in Permalloy Films*, J. Appl. Phys. **29**, 294 (1958).

[33] M. S. Cohen, *Handbook of Thin Film Technology*, McGraw, New York, 1970.

[34] S. Middelhoek, *Domain Walls in Thin Ni-Fe Films*, J. Appl. Phys. **34**, 1054 (1963).

[35] W. F. Brown and A. E. LaBonte, *Structure and Energy of One-Dimensional Domain Walls in Ferromagnetic Thin Films*, J. Appl. Phys. **36**, 1380 (1965).

[36] N. G. Einspruch, *VLSI Electronics: Microstructure Science*, volume 16, Academic, New York, 1987.

[37] C. Pels, *Ferromagnetic Electrodes for Spin Polarized Transport - Technology and Experiments*, Ph.D. Thesis, Universität Hamburg, 2003.

[38] R. Wiesendanger, *Scanning Probe Microscopy and Spectroscopy: Methods and applications*, Cambridge University Press, 1994.

[39] P. Grütter, *Applications of Magnetic Force Microscopy*, Kluwer, Dordrecht, 1995.

[40] U. Y. Martin and H. K. Wickramasinghe, *Magnetic imaging by „force microscopy"with 1000 Å resolution*, Appl. Phys. Lett. **50**, 1455 (1987).

[41] S. McVitie, G. S. White, J. Scott, P. Warin, and J. N. Chapman, *Quantitative imaging of magnetic domain walls in thin films using Lorentz and magnetic force microscopies*, J. Appl. Phys. **90**, 5220 (2001).

[42] D. Rugar, H. J. Mamin, G. Guenther, S. E. Lambert, J. E. Stren, I. McFadyen, and T. Yogi, *Magnetic force microscopy: General principles and application to longitudinal recording media*, J. Appl. Phys. **68**, 1169 (1990).

[43] U. Hartmann, T. Göddenhenrich, and C. Heiden, *Magnetic force microscopy: Current status and future trends*, J. Magn. Magn. Mat. **101**, 263 (1991).

[44] H. J. Hug, P. J. A. van Schendel, A. Moser, R. Hofer, S. Martin, H. J. Güntherodt, S. Parthun, L. Abelmann, J. C. Lodder, G. Bochi, and R. C. O'Handley, *Quantitative magnetic force microscopy on perpendicularly magnetized samples*, J. Appl. Phys. **83**, 5609 (1998).

[45] A. Wadas and H. J. Güntherodt, *Lateral Resolution in Magnetic Force Microscopy. Application to Periodic Structures*, Phys. Lett. A **146**, 277 (1990).

[46] K. Babcock, *Magnetic Force Microscopy: High-Resolution Imaging for Data Storage*, Application Notes, Digital Instruments (1994).

[47] C. B. Prater, P. G. Maivald, K. J. Kjoller, and M. G. Heaton, *Tapping mode^{TM} Imaging: Applications and Technology*, Application Notes, Digital Instruments (1995).

[48] V. Elings and J. Gurley, editors, US Patent No. 5,308,974 (1994), Digital Instruments, Santa Barbara, CA, May 3, 1994.

[49] Object Oriented MicroMagnetic Framework, http:\\math.nist.gov\oommf.

[50] A. Aharoni, *Introduction to the Theory of Ferromagnetism*, Clarendon Press, Oxford, 1996.

[51] D. V. Berkov, K. Ramstöck, and A. Hubert, *Solving Micromagnetic Problems Towards an Optimal Numerical Method*, Phys. Stat. Sol. (a) **137**, 207 (1993).

[52] L. Landau and E. Lifshitz, *On the Theory of the Dispersion of Magnetic Permeability in Ferromagnetic Bodies*, Physik. Z. Sowjetunion **8**, 153 (1935).

[53] T. L. Gilbert, *A Lagrangian Formulation of the Gyromagnetic Equation of Magnetization Field*, Phys. Rev. **100**, 1243 (1955).

[54] W. F. Brown, Jr., *Magnetostatic Principles in Ferromagnetism*, In: E. P. Wohlfarth, editor, *Selected Topics in Solid State Physics*, volume 1, Amsterdam, 1962. North-Holland.

[55] M. J. Donahue and D. G. Porter, *OOMMF User's guide*, Version 1.2a3, Interagency Report NISTIR 6376, NIST, Gaithersburg, MD, 2002.

[56] A. Aharoni, *Demagnetization Factors for Rectangular Ferromagnetic Prisms*, J. Appl. Phys. **83**, 3432 (1999).

[57] A. J. Newell, W. Williams, and D. J. Dunlop, *A Generalization of the Demagnetizing Tensor for Nonuniform Magnetization*, J. Geophysical Research - Solid Earth **98**, 9551 (1993).

[58] M. J. Donahue and R. D. McMichael, *Exchange Energy Representation in Computational Micromagnetics*, Physica B **233**, 272 (1997).

[59] M. J. Donahue, *A variational approach to exchange energy calculations in micromagnetics*, J. Appl.Phys. **83**, 6491 (1998).

[60] M. R. Scheinfein, J. Unguris, R. J. Celotta, and D. T. Pierce, *Influence of the Surface on Magnetic Domain-wall Microstructure*, Phys. Rev. Lett. **63**, 668 (1989).

[61] R. D. McMichael and M. J. Donahue, *Head to Head Domain Wall Structures in Thin Magnetic Strips*, IEEE Trans. Mag. **33**, 4167 (1997).

[62] A. Hubert and M. Rührig, *Micromagnetic analysis of thin-film elements*, J. Appl. Phys. **69**, 6072 (1991).

[63] R. H. Koch, J. G. Deak, D. W. Abraham, P. L. Trouilloud, R. A. Altman, Y. Lu, W. J. Gallagher, R. E. Scheuerlein, K. P. Roche, and S. S. P. Parkin, *Magnetization Reversal in Micron-Sized Magnetic Thin Films*, Phys. Rev. Lett. **81**, 4512 (1998).

[64] R. Eiselt, *Charakterisierung ferromagnetischer Elektrodenstrukturen mittels Hall-Sondenmagnetometrie*, Diploma Thesis, Universität Hamburg, 2001.

[65] A. K. Geim, S. V. Dubonos, J. G. S. Lok, I. V. Grigorieva, J. C. Maan, L. Theil Hansen, and P. E. Lindelof, *Ballistic Hall micromagnetometry*, Appl. Phys. Lett. **71**, 2379 (1997).

[66] E. H. Hall, *On a New Action of the Magnet on Electrical Currents*, Amer. J. Math. **2**, 287 (1879).

[67] G. Meier, *Herstellung und Charakterisierung magnetischer Nanostrukturen*, Ph.D. Thesis, Universität Hamburg, 1999.

[68] W. Nolting, *Elektrodynamik*, Springer, Berlin, 2002.

[69] U. Hartmann, *The Point Dipole Approximation in Magnetic Force Microscopy*, J. Magn. Magn. Mat. **137**, 475 (1989).

[70] J. Lohau, S. Kirsch, A. Carl, G. Dumpich, and E. F. Wassermann, *Quantitative determination of effective dipole and monopole moments of magnetic force microscopy tips*, J. Appl. Phys. **86**, 3410 (1999).

[71] H. Rolff, *Hall- und Bend-Widerstands-Magnetometrie an mikro- und nanostrukturierten Ferromagneten*, Ph.D. Thesis, Universität Hamburg, 2003.

[72] M. Steiner, G. Meier, U. Merkt, and J. Nitta, *Magnetic transitions of permalloy rings in hybrid devices*, submitted to Physica E.

Danksagung

Ich möchte mich an dieser Stelle bei allen bedanken, die mir diese Arbeit durch ihre Unterstützung ermöglicht haben. Dabei gilt mein besonderer Dank

Prof. Dr. Ulrich Merkt für die Auswahl und die Übertragung dieser Arbeit und für sein Vertrauen, dass man auch als (werdende) Mutter eine Promotion schaffen kann,

Dr. Guido Meier für die hervorragende Betreuung und Unterstützung, die Flexibilität in Bezug auf meine Arbeitszeiten sowie 1000 unphysikalische Gespräche,

Prof. Dr. Wolfgang Hansen für die Übernahme des Zweitgutachtens,

Alexander Thieme für die unkomplizierte Zusammenarbeit bei der Programmierung und die schnelle Hilfe in vielen Notfällen,

Dr. Christian Pels für die erfolgreiche Einführung in die Präparation,

Dr. Katrin Buth für die angenehme Schreibtischnachbarschaft und viele Tips zu Igor, LaTeXund Co.,

Dr. Hans Fangohr und Dr. Haiko Rolff für so einige Diskussionen über Magnetismus,

Markus Bolte für viele kritische Fragen,

Peter Baars für die Mitteilungen seiner Sicht der Dinge und die Unterstützung in harten Zeiten,

Dr. Michael Rübhausen für zahlreiche informative Verabredungen zu Mittagessen oder Glühwein,

der gesamten Gruppe N für die nette Arbeitsatmosphäre,

Prof. Dr. Stefan Halverscheid für die kritische Durchsicht dieser Arbeit,

und denjenigen, die mir - besonders in den letzten Wochen - den Rücken freigehalten haben: meinen Eltern und Schwiegereltern, sowie Ruth Müllerwiebus und Susanne Halverscheid.

Mein größter Dank gilt meiner Familie für ihre große Unterstützung in guten wie in schlechten Zeiten.

Danke Henry, Maja und Ben!!!